USGS-OFR-90-36

UNITED STATES
DEPARTMENT OF THE INTERIOR
GEOLOGICAL SURVEY

Oxygen depletion studies in the Electrical Power Research Institute, Compressed Air Energy Storage facility, Pittsfield, Illinois

by

Edgar F. Ethington, Gary R. Olhoeft, and Trude V.V. King

Open-File Report 90-36

Prepared by the U. S. Geological Survey, Denver, Colorado

for

Electrical Power Research Institute
Research Project RP8000-17

January, 1990

ABSTRACT

A series of measurements were made to determine the capability of some montmorillonites, illite, pyrite, and clayey sandstones to deplete dissolved oxygen from water. The parameters monitored were dissolved oxygen content, redox potential, and pH. Some clays, iron pyrites, and clayey sandstones did deplete oxygen from an oxygen enriched aqueous solution. Of the properties measured, pH seems to the controlling factor on a mineral's capability to deplete oxygen. Pyrite will deplete oxygen in a neutral or basic environment but not in an acidic environment. Some clays and illite bearing sandstones deplete oxygen when the aqueous environment is acidic but not when it is basic. The results of this study indicate that the iron-bearing sulfide (pyrite/marcasite) and clay (illite/smectite) mineralogy of the site were in a reduced state and readily available to deplete oxygen from injected air by aqueous oxidation. Further, the use of acids to complete the wells at the Pittsfield, Illinois, Compressed Air Energy Storage site worsened the problem of oxygen depletion from the injected air by mineral oxidation.

INTRODUCTION

The Electric Power Research Institute (EPRI) Compressed Air Energy Storage (CAES) Program stores pressurized air underground with off-peak power (EPRI, 1987). This air is later recovered and used to enhance combustion during peak power demands. At the Pittsfield, Illinois, CAES test site, an anomalous oxygen loss was noted (Istvan and Pereira, 1987). In the absence of evidence for biological activity (Risatti and Brower, 1987), earlier studies (Krapac et al., 1987) proposed the loss of oxygen through oxidation of pyrite, though it was recognized that oxidation of illite clay might also be important (De Vine and Davies, 1985).

EPRI conducted feasibility projects, RP-1795-15 and RP-2488-10, at a site near Pittsfield, Illinois, for the purpose of using a geologic reservoir for the storage and recovery of compressed air. Several wells were drilled into the St. Peter Formation, acidified, and completed. Acidification was done three times. The first two consisted of 15% hydrochloric acid (HCl) solutions, and the third was a solution of 12% hydrochloric acid (HCl) and 3% hydrofluoric acid (HF) (De Vine and Davies, 1985). The sandstone porosity becomes the air reservoir as water is displaced by the injected air. When the air was injected and withdrawn in a regular cycle of days or weeks, the composition of the air withdrawn from the reservoir did not differ significantly from atmospheric air, but air stored for several months became depleted in oxygen (Istvan and Pereira, 1987). A maximum of 3.164×10^6 m^3 (cubic meters) of air was injected into the reservoir by December, 1983. Assuming an oxygen fraction of 20.95%, 6.326×10^5 m^3 of oxygen was injected. This is equivalent to 2.96×10^7 moles of oxygen. The final percentage of oxygen in the recovered air as reported in July, 1985 was 2.83%. This implies a loss of 2.56×10^7 moles of oxygen in a year. There was a slight increase in the percentage of carbon dioxide in the recovered air (De Vine and Davies, 1985), but isotope studies ruled out significant biological activity (Risatti and Brower, 1987). Core samples examined after air injection revealed evidence of sulfur mineral oxidation in the form of gypsum and elemental sulfur (Core Lab, 1987; De Vine and Davies, 1985; and Harmon, 1987).

This report describes a series of measurements determining the capability of pyrite and several clay minerals to deplete oxygen from the Pittsfield CAES reservoir. The parameters, dissolved oxygen concentration (PO_2), redox potential (Eh), and hydrogen ion concentration (pH) were measured as a function of time for various initial starting conditions. For the O_2-H_2O couple

$$O_2 + 4H^+ + 4e^- \; . \; 2H_2O,$$

at room temperature, these measured parameters are related as:

$$Eh = 1.229 - 0.074 \log PO_2 - 0.059 \; pH \qquad \text{(in volts)},$$

where PO_2 is the partial pressure of O_2 in Pascals (Rowell, 1981) (1 ppm O_2 = 2200 Pascals at 20^0C). Similarly, for the

$$Fe(OH)_3{}^s + 3H^+ + e^- \; . \; Fe^{2+} + 3H_2O \text{ couple},$$

$$Eh = 1.06 - 0.059 \log [Fe^{2+}] - 0.177 \; pH \qquad \text{(in volts)},$$

which also holds for the Fe^{2+}-$Fe(OH)_3$ couple

$$Fe(OH)_3 \; . \; Fe^{3+} + 3OH^-$$

$$Fe^{3+} + e^- \; . \; Fe^{2+}$$

when the solubility product of $(Fe^{3+})(OH)_3$ is considered (Rowell, 1981).

The aqueous oxidation of pyrite is well known and understood (Bloomfield, 1972; Klein and Shuey, 1979; Wong, 1979; Rowell, 1981; Nordstrom, 1982; Lindsay, 1988; van Breeman, 1988). As other studies have concentrated on the oxidation of pyrite (De Vine

and Davies, 1985; Krapac et al., 1987; Plumlee and Ridley, 1989), this report concentrates on the possible oxygen depletion due to the presence of clays. A literature review (Ridley and Plumlee, 1988) has ruled out significant oxygen depletion by physical or chemical adsorption processes. Thus, oxygen depletion by clays probably results from the oxidation of structural Fe^{2+} (Rozenson and Heller-Kallai, 1978; Badaut et al., 1985; Stucki, 1988; Scott and Amonette, 1988). The rate of Fe^{2+} oxidation in montmorillonite increases with increasing surface acidity and surface area, and is faster for wet than dry clay (Rozenson and Heller-Kallai, 1978; Yariv and Cross, 1979). Graf et al. (1988) argue for reversible oxidation of ferrous iron through a coupled cation exchange redox process. A companion report (Plumlee and Ridley, 1989) discusses geochemical models of clay and pyrite, suggesting that iron-bearing clays will buffer pyrite. In the presence of pyrite, iron in clays should be in the Fe^{2+} oxidation state which is readily oxidized to Fe^{+3} (Nordstrom, 1982). Further, laboratory studies using natural clays indicate that it is difficult to prevent clays from oxidizing when exposed to the atmosphere, particularly when wet and at low pH (Scott and Amonette, 1988; Stucki, 1988). A representative bibliography of clay oxidation studies is included in the reference list.

APPROACH

The approach taken in this study was to observe and document the reaction between certain clays, pyrite, EPRI well L-1 samples, and an oxygen enriched aqueous solution, and to determine what measured factors control oxygen depletion. This was done by injecting oxygen-poor materials into oxygen-enriched water, and observing changes in dissolved oxygen content, pH, and Eh in a closed system.

Dissolved oxygen content in an aqueous solution was the primary quantity to be measured, and the reasons for its change as a function of time and exposed material was the primary interest. Eh (redox potential) and pH (acidity or alkalinity) measurements were necessary to describe the general chemical state of the system. Redox potential, or Eh, is the voltage measured in a reversible manner, for any reversible cell and measured against a standard hydrogen half-cell reaction (Garrels and Christ, 1965). The activity of the hydrogen ion, H^+, is characterized using pH; it is the negative log of H^+ concentration. The Eh probe used in these studies is equivalent to a calomel electrode (Orion Research, 1983) and results differ from a hydrogen cell potential by +0.2415 volts (Mortimer, 1971).

Illite and montmorillonite clays were studied. A synopsis of their structure, similarities, and differences are presented. Montmorillonites were chosen to begin this study because of their high surface area, high cation exchange capability, and their ready availability. Illite was found to be the dominant clay in the EPRI core samples, and thus, its study became necessary. A kaolinite sample and a fumed silica sample were used in one measurement each to observe the reactions caused by mineral structures different from the illite or montmorillonite and found in the EPRI core samples. Samples of powdered Georgetown, Colorado iron pyrite were observed, as pyrite is also known to exist in the EPRI samples.

Scanning electron microscope (SEM), energy dispersive x-ray spectra (EDX), and infrared reflectance spectroscopy analysis revealed little iron pyrite and abundant clay in the samples from well L-1. However the core is very heterogeneous, and a large volume average concentration of pyrite is probably 0.05 weight percent (G. Plumlee, written communication).

The core samples studied are quartz arenites (Folk, 1974) from the St. Peter Sandstone of upper Ordovician age. They contain quartz, potassium feldspar, calcium carbonate, clay and traces of rutile and pyrite (FeS_2). Quartz and calcium carbonate do not react with oxygen. The calcium carbonate will react with both acids, and the hydrofluoric acid will react with all of the minerals present, preferring the calcium cation. Potassium feldspar is stable in the temperature range of 25-100°C (Velde, 1985, p.263). This leaves the illite and iron pyrite as the minerals likely to react with oxygen.

CHEMICAL AND STRUCTURAL DESCRIPTION OF THE CLAYS

$((Na,Ca)(Al,Mg,Fe)_2Si_4)_{10}(OH)_2 \cdot nH_2O)$ is the general chemical formula for montmorillonites, members of the smectite group of minerals (Fleischer, 1983). However, the bulk chemical compositions of the smectites are dispersed over a wide field which includes the fully expandable smectites, mixed layer, and extreme illite compositions (Velde, 1985). Montmorillonites are composed of units made up of two silica tetrahedral sheets and a central alumina octahedral sheet. All the tips of the tetrahedra point to the center of the unit. The tetrahedral and octahedral sheets are combined so that the tips of the silica sheet and one of the hydroxyl layers of the octahedral sheet form at O instead of OH. In stacking, the O units of each layer are adjacent to the O units of the adjacent sheet and a very weak bond is formed between them which acts as a cleavage surface. The distinguishing feature of smectites is that water and other polar or polarizable molecules can enter between the units, resulting in expansion of the lattice.

Exchangeable cations occur between the silicate layers and are believed to control, at least in part, the expansion properties of the clay. The most common interlayer ions in smectites are Na, Ca, K, and Mg. The exchangeable cations are held on the outer surface of the clay packet and do not change the structure of the silica-alumina framework (Grim, 1968). Smectites have an unbalanced charge on their surfaces due to: broken bonds around the edges of the silica-alumina packets; substitutions within the lattice structure of trivalent alumina for quadrivalent silicon in the tetrahedral sheet and ions of lower valence for trivalent alumina in the octahedral sheet; and hydrogens of exposed hydroxyls may be replaced by a cation which is exchangeable (Grim, 1968). The net charge deficiencies are balanced by adsorbed cations at either the edges or basal surfaces.

In electron micrographs, montmorillonite is seen as finely divided, platy forms, commonly with poorly defined outlines and crumpled edges (Brindley, 1980). The areal dimensions of the individual forms are estimated to be ten to one hundred times the thickness.

The natural occurrences of smectites are varied and complex (Velde, 1985). Montmorillonites occur in nature as: weathering products of varied rock types under medium intensity conditions; authigenic sediments in marine and lagunal environments; common components of sedimentary rocks which have not seen temperatures in excess of 100^oC at depths of more that two kilometers; in the argillic-propylitic zones of hydrothermal systems; and in volcanic rocks from the late stages of cooling (Velde, 1985). Smectite oxidation is discussed in Anderson and Stucki (1978), Badaut et al. (1985), Bart et al. (1980), Bonnin et al. (1985), Brigatti (1983), Chen et al. (1979), Craciun (1984), Eslinger et al. (1979), Goodman et al. (1976), Grman et al. (1973), Harder (1978), Lear and Stucki (1985), McBride (1979), Ross and Kodama (1976), Ross (1975), Roth et al. (1969), Rozenson and Heller-Kallai (1976, 1978), Russell (1979), Sayin (1982), Smith et al. (1980), Stucki and Roth (1976, 1977), Stucki (1988), Stucki et al. (1984), and van Breeman (1980).

As smectites become less stable due to increases in temperature, depth of burial, or increases in surface charge, the chances of their coexistence in a mixed layer assemblage, such as illite-smectite become more likely (Velde, 1985). Many clays are reported to be gradational between smectite and illite, but are in fact mixtures of true illite and smectite (Grim, 1968). In such material, the balancing cations might vary from layer to layer as well as within the same layer (Grim, 1968). The classification of such a material would be difficult and frequently the separation between smectite and illite is arbitrary, expanding material being called smectite and non-expanding material being classified as illite.

$(K,H_3O)(Al,Mg,Fe)_2(Si,Al)_4O_{10}(OH_2,H_2)$ is the basic general chemical formula for illite (Fleischer, 1983). However, many illites are mixed-layer structures and the

mixed layering is not obvious when the proportion of admixed layers, commonly montmorillonite, is small (<10%) (Brindley, 1980). Thus, an average chemical formula may be misleading. Illites consist of two silica tetrahedral sheets around a central octahedral sheet. The tips of the tetrahedral sheets point toward the center and are combined with the octahedral sheet in a single layer. The unit is the same as montmorillonite with the exception that some of the silicon is always replaced by aluminum. The resultant charge deficiency is balanced by potassium, calcium, magnesium, or hydrogen ions which occur between the unit sheets (Grim, 1968). Iron and magnesium can substitute for aluminum in some dioctahedral illites.

The structure of illites differs from smectites in number of ways (Grim, 1968). Firstly, the charge deficiency on illites is approximately twice that for smectites. Secondly, the balancing cation in illite is nearly always potassium. Because of these differences, the illite structural units are relatively fixed in position, and polar molecules can not enter between the layers and cause expansion (Grim, 1968).

Illites are known to represent a compositionally wide range of solid solutions and to be present in most geologic environments (Velde, 1985). Illite can form in several ways including burial metamorphism and as a weathering product stable under intermediate conditions (Velde, 1985). In addition, illite is also reported to be stable to short durations of river transport but converts to chlorite or an expandable clay in a marine environment (Velde, 1985, and references therein). Illite can also be formed in sedimentary environments and is the most dominant species of clay in argillaceous sedimentary rocks (Grim, 1968). Velde (1985) reports that illite is the primary replacement mineral of acidic rocks in the inner-most zone, closest to the hydrothermal fluids, of hydrothermal systems. Illite is frequently derived from biotite. Oxidation studies of biotite and illite are reported in Addison and Sharp (1963), Amonette et al. (1985), Barshad and Kishk (1968), Besson et al. (1987), Beyme et al. (1977), Bouda and Isaac (1986), Eslinger et al. (1979), Farmer et al. (1971), Gilkes et al. (1972, 1973), Ismail (1969, 1970), Roth et al. (1968), Sayin (1982), Scott and Youssef (1979), and Veith and Jackson (1974).

CORE DESCRIPTIONS FOR THE EPRI L-1 SAMPLES

The first EPRI core samples from the Pittsfield, Illinois well L-1 were received from Core Labs in January, 1989. These samples had been exposed to air for at least two weeks. A second set of EPRI core samples from the Pittsfield well L-1 which had been stored in a nitrogen environment was received from Core Labs in April, 1989. This is the set of cores used in the majority of this study.

The following descriptions of the core sample are based on visual, optical microscopic, scanning electron microscope, energy dispersive x-ray (EDX), and infrared spectral analysis, and on measurements using a helium pycnometer and surface area analyzer.

depth: 624.25' to 624.60' (Green Sand)

A greenish-grey sandstone with black splotches perpendicular to sub-perpendicular to the direction of the core. The sample is moderately cemented. The grains are moderately well-sorted, well-rounded, frosted quartz with approximately 2% dark minerals and have no preferred orientation. The sample reacts with dilute hydrochloric acid. The surfaces of the quartz grains are coated with many fine particles. These particles are rhombs of potassium feldspar in and on a layer of illite clay. Iron is a minor component of the clay layer. The measured surface area is 4.29 m^2/gram. Figures 1 thru 4 show the coated quartz grains, rhombs, and clay. The lower half of each figure is the EDX spectra for the area in the photograph.

depth: 624.8' to 625.25' (Green Sand)

A greenish-grey sandstone with some linear and splotchy black features that are

parallel to 30^{o} from the axis of the core. Some bedding is observed. The grains are well-sorted, frosted, rounded to sub-rounded, and moderately cemented. Quartz is the primary mineral. There are also feldspars and illite. Illite clay coats most of the interior surfaces. The measured surface area is 2.69 m^2/gram. Energy dispersive spectral analysis reveals no appreciable iron in this sample. Figures 5, 6, and 7 illustrate the clay coating and its energy dispersive signature.

depth: 630.9 to 632.0' (White Sand)

A pale grey sandstone with a sugary texture and no obvious sedimentary structures. It is moderately well-cemented. The grains are 0.1 to 0.3 mm in diameter, moderately well-sorted, well-rounded to sub-rounded, frosted quartz. Crystal facets appear on about 5% of the grains. There is only a trace of dark minerals. Some of the cementing material reacts to hydrochloric acid. The surfaces of the quartz grains exhibit quartz overgrowths, authigenic potassium feldspar rhombs, and a layer of illite. The feldspar rhombs have dissolution cavities and a slight alteration surface. Figures 8 through 11 show the overall sample texture, details of the quartz overgrowths, and a feldspar rhomb. The EDX spectra reveal no iron in this sample, but rather quartz and potassium aluminium silicates.

depth: 635' to 641' (White Sand grading to Grey Sand)

A light grey, fine grained sandstone with no obvious sedimentary structures. The sample is well cemented and competent. The grains are 0.2 to 0.3 mm in diameter, well rounded to sub-angular, moderately well sorted, spherical to sub-spherical, frosted quartz. There is some development of quartz crystal overgrowths. The cement is partly carbonate. The quartz grains have a slight coating of chlorite and illite. Figure 12 and 13 show the microscopic sample texture. The measured surface area is 0.47 m^2/gram. Figures 14 thru 16 are detailed examinations of clay, a quartz overgrowth, and rutile found in this sample. The EDX spectra reveals the presence of minor amounts of iron in this sample.

DISCUSSION OF SCANNING ELECTRON MICROSCOPE DATA

Figures 1 through 17 contain SEM photographs and EDX spectra. This data pair can be used to determine the identity of minerals, examine texture, and determine bulk composition in a rock sample. The photograph, in detail, yields the habit and form of a mineral and its setting. Set to a wider field of view, the photograph records the textural characteristics of a sample. The EDX spectra gives the relative abundance of elements within the field of view of the photograph. So by changing the field of view of the scanning electron microscope, the EDX can yield compositional information ranging from individual crystals to the rock sample as a whole. By knowing the host rock lithology, the crystal habit of a mineral, and its elemental components, an unknown mineral can usually be identified.

In the lower left portion of each SEM photograph is a short white horizontal line. This line denotes the scale of the photograph as indicated by the length printed below the line. The other printed information on the photograph deals with electron energy, sample number, and photograph number. The EDX spectra below the photograph has number of counts as the ordinate and energy as the abscissa. The common energy peaks of different elements are shown in the spectral graph. The gold (Au) and copper (Cu) peaks prominent in all the spectra are from the coating used on the samples.

The abundance of iron (Fe) in these samples is of particular interest because it could deplete oxygen through oxidization given the proper conditions. Whether the iron is combined in silicate minerals or in pyrites is not indicated by the EDX. But if there is no iron, then there is no pyrite. If iron is indicated in a bulk EDX spectra, then one must look for the source of the iron. In all cases but one, the source of the iron peak in the EDX spectra was clay. In only one case was a crystal of iron pyrite coated with

illite found, and it was found only after a lengthy search of the sample. This example is shown in Figure 17 and comes from L-1 626' (from the first set of L-1 samples received).

DISCUSSION OF INFRARED SPECTRA

Pittsfield core samples were characterized by near-infrared and mid-infrared spectroscopy to determine the presence and types of minerals in the core samples. Core samples were measured using reflected light from 0.2 to 25 μm. Reflectance spectroscopy analysis is sensitive to the presence of clays, on the order of a few weight percent and greater, in a mineral mixture.

Figure 18 shows the reflectance spectra of the EPRI L-1 625' sample (that has not be exposed to air) as a function of drying-time in the spectrometer under humid, oxygenated gas flow. The bottom most spectrum is representative of the sample as it was removed from the nitrogen environment and placed in the spectrometer. The broad absorption between approximately 2.7 and 3.3 microns in the spectra with the least drying times is attributed to the presence of water in the sample. The absorption feature near 4.0 microns in all the spectra can be attributed to fundamental vibrations of a carbonate mineral or a smectite bearing mineral. With increased drying time, the samples lose the free water that was adsorbed onto the sample. As the water is removed, the sample increases in reflectance and additional absorption features, which have been masked by the presence of water, become more visible. By 2400 seconds, the spectrum of the sample is beginning to show absorption features near 3.5 microns which are attributed to calcite as well as an absorption feature near 2.7 microns indicative of an illite/smectite clay mineral phase. It is commonly impossible to spectrally or chemically differentiate between illites and smectites, because of their tendency to form intergrown complexes. Thus, we will refer to illite/smectite intergrowths, even though spectrally, the presence of illite dominates in most instances.

Figure 19 shows the reflectance spectra of a standard laboratory dolomite, (Hunt and Salisbury Collection, U.S.G.S. Denver, HS102.2B) calcite(HS194.2B), the EPRI I-1 641' sample, and the EPRI L-1 631' sample. The absorption features in the EPRI samples, near 3.4 microns, are due to the presence of the CO_3 fundamental vibration in carbonates. The broad absorption feature centered near 3 microns is caused by the presence of water and hydroxyl-bearing mineral phases, most likely illite/smectite. Dolomite is spectrally distinguished from calcite by a shift in the position of the CO_3 fundamental vibration by approximately 0.03 microns. The fundamental vibration for dolomite has a shorter wavelength than calcite.

Figure 20 shows the reflectance spectra of Pittsfield L-1 625' and 624.5' samples, the I-1 651' sample, and standard laboratory spectra for illite (IMt-1), kaolinite (KGa-1), and smectite (SWy-1) (Van Olphan and Fripiat, 1979). The three bottom spectra represent the L-1 625' sample as measured without exposure to an oxidizing environment (no suffix), one that has been exposed to air (air suffix), and the third that has been exposed to air, then dried and wetted with distilled water, exposed to air, and dried again (ox suffix). The wet L-1 625' sample is spectrally dominated by the presence of water. The dried L-1 625' samples show absorption features attributed to smectite and illite as well as carbonates (as discussed above). The presence of illite/smectite is substantiated by the absorption features near 2.7 and 4 microns (as seen in the laboratory standards). There is no spectral indication that the L-1 625', 624.5', or I-1 651' samples contain any kaolinite.

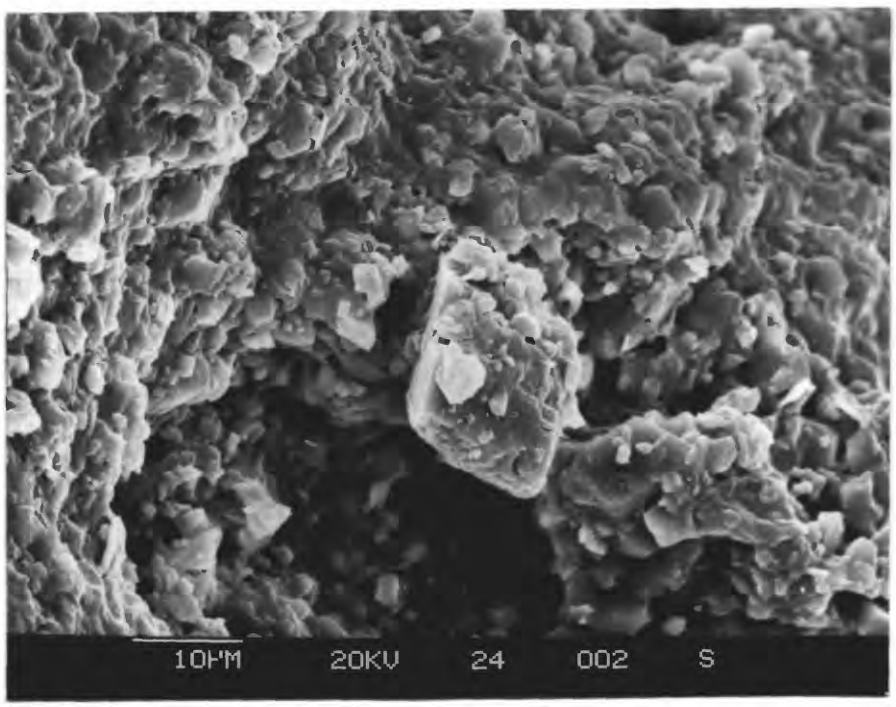

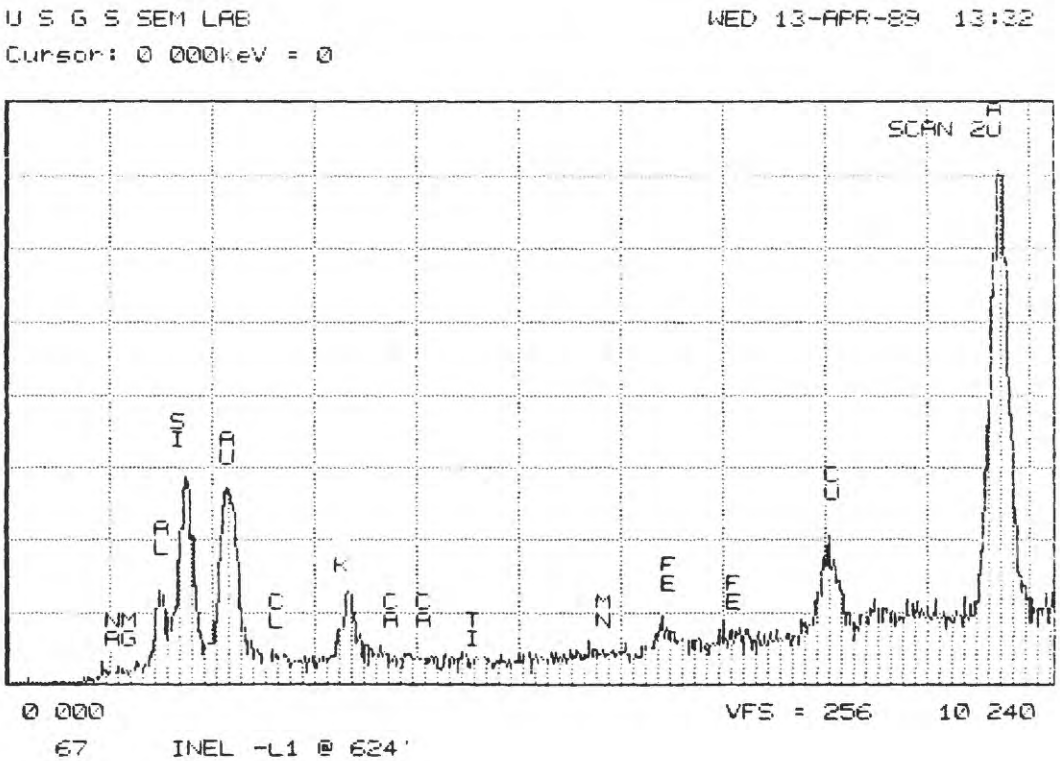

Figure 1. SEM photograph and EDS spectra of the illite and feldspar rhombs coating a quartz grain.

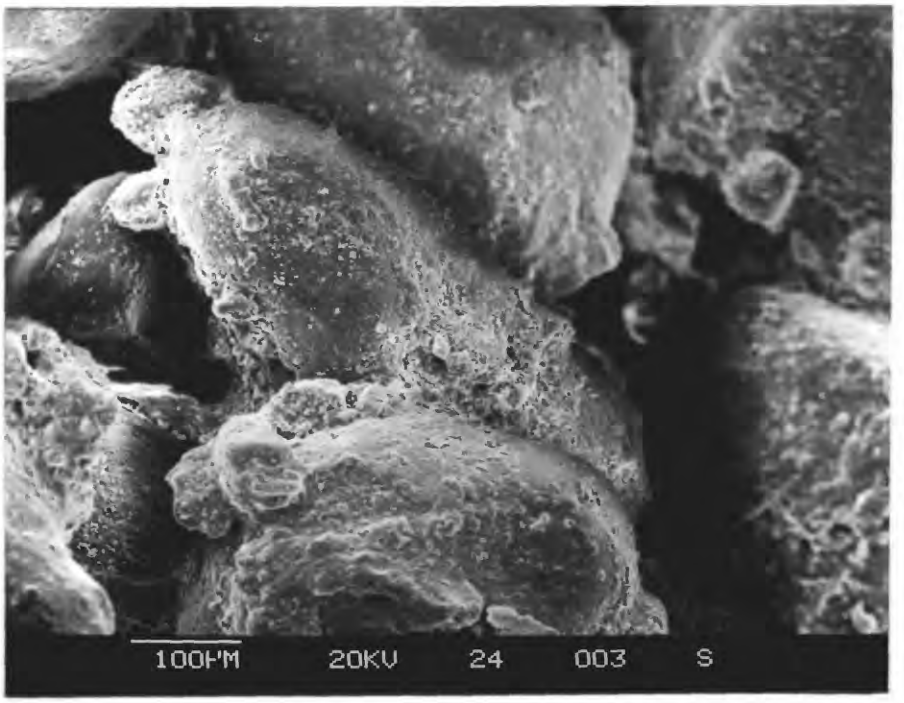

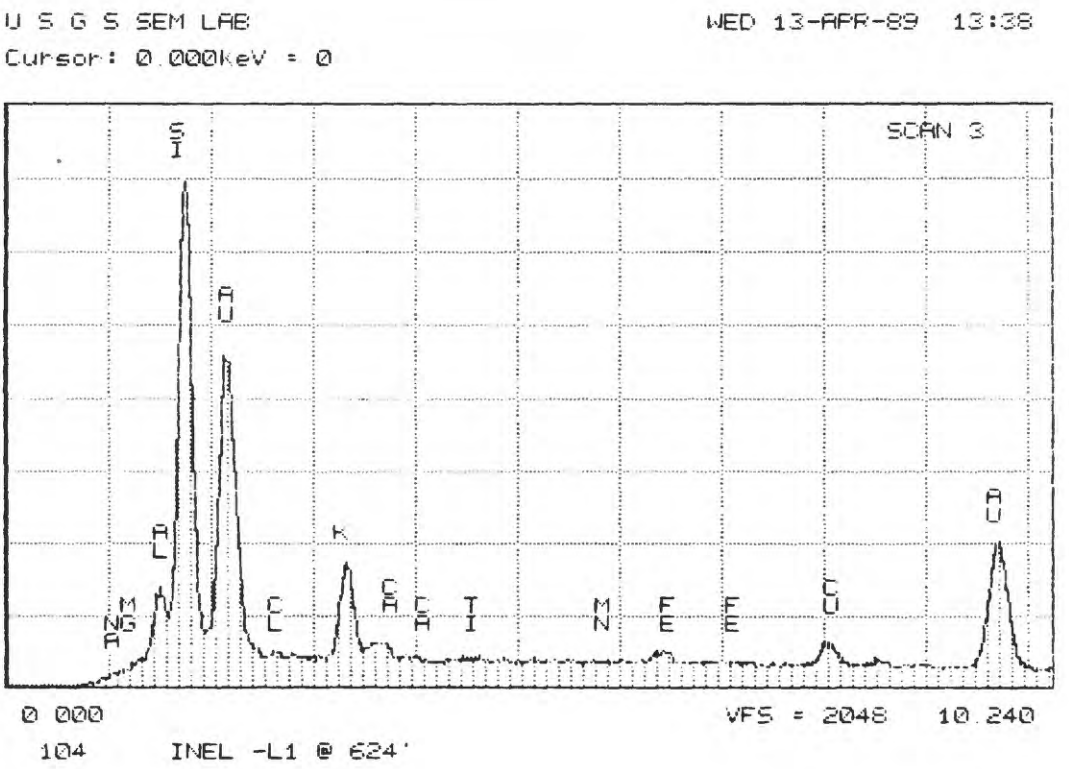

Figure 2. SEM photograph and EDS spectra of coated quartz grains.

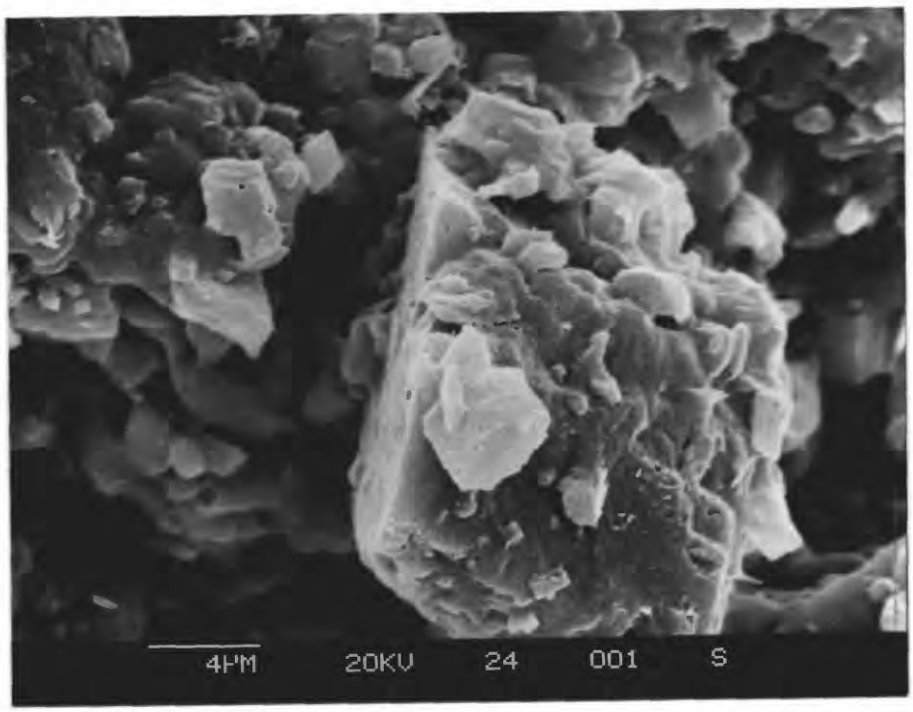

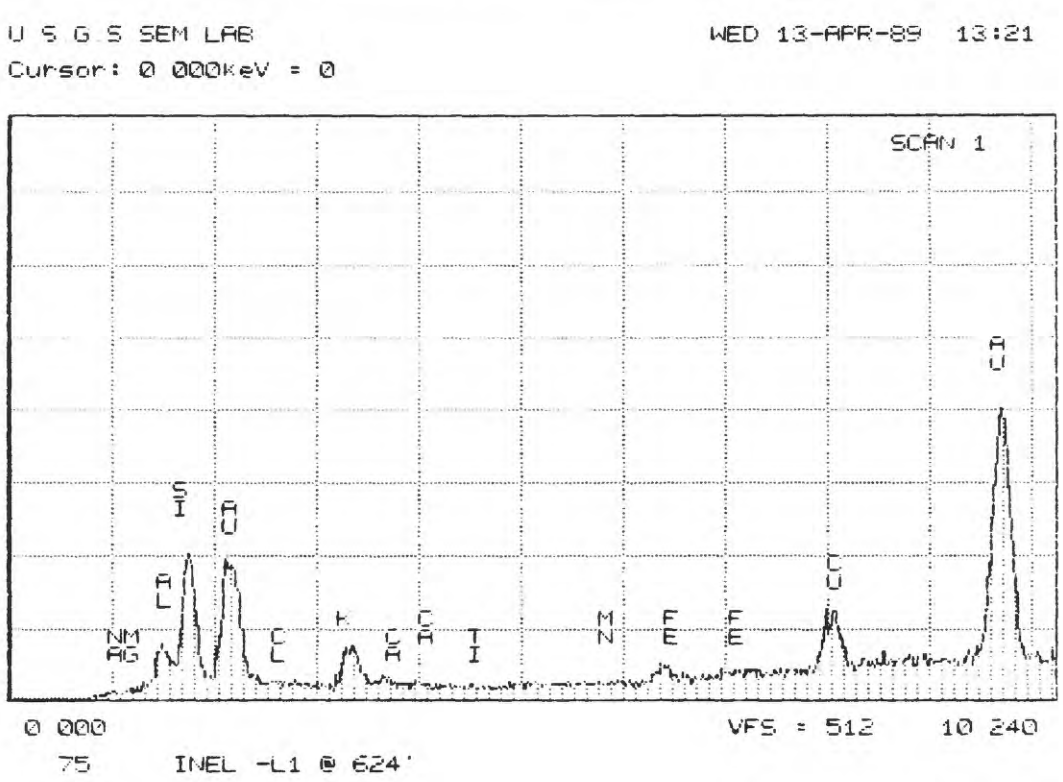

Figure 3. SEM photograph and EDS spectra of a feldspar rhomb on a clay coating.

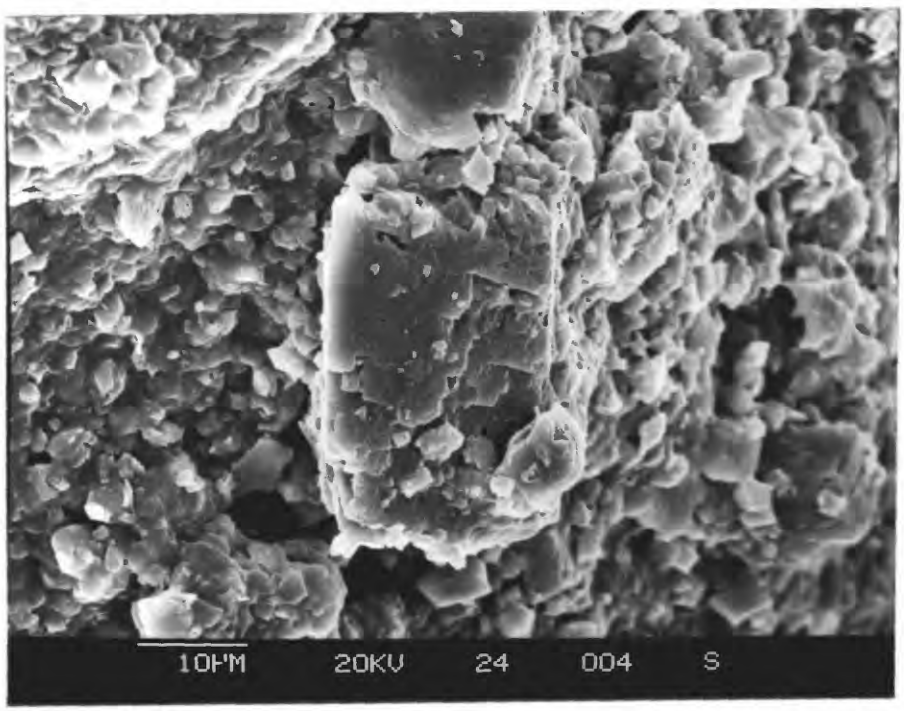

U S.G S SEM LAB WED 13-APR-89 13:43
Cursor: 0 000keV = 0

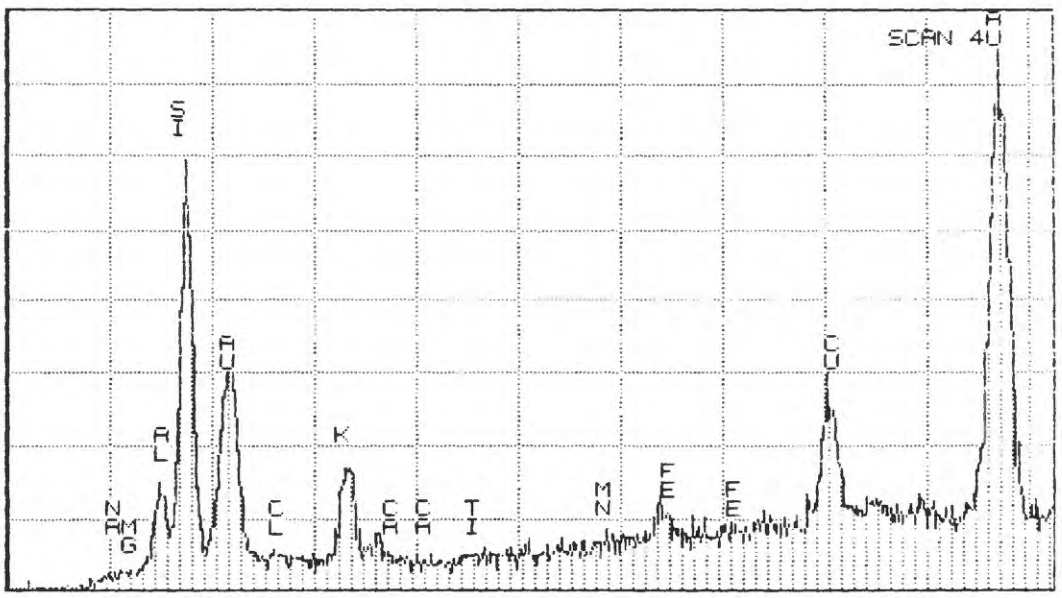

Figure 4. SEM photograph and EDS spectra of a feldspar rhomb on a clay coating.

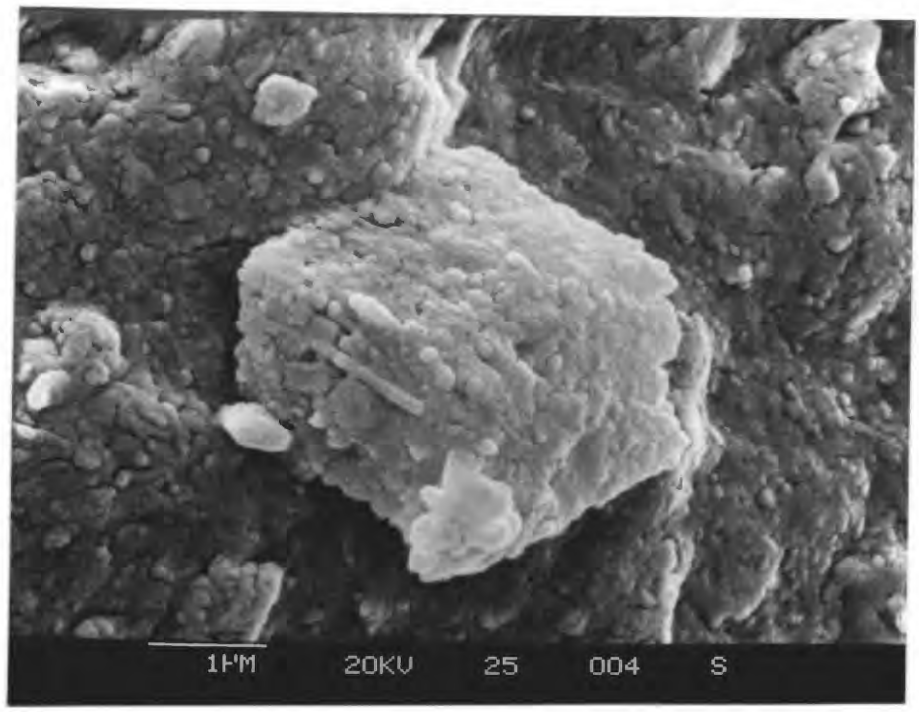

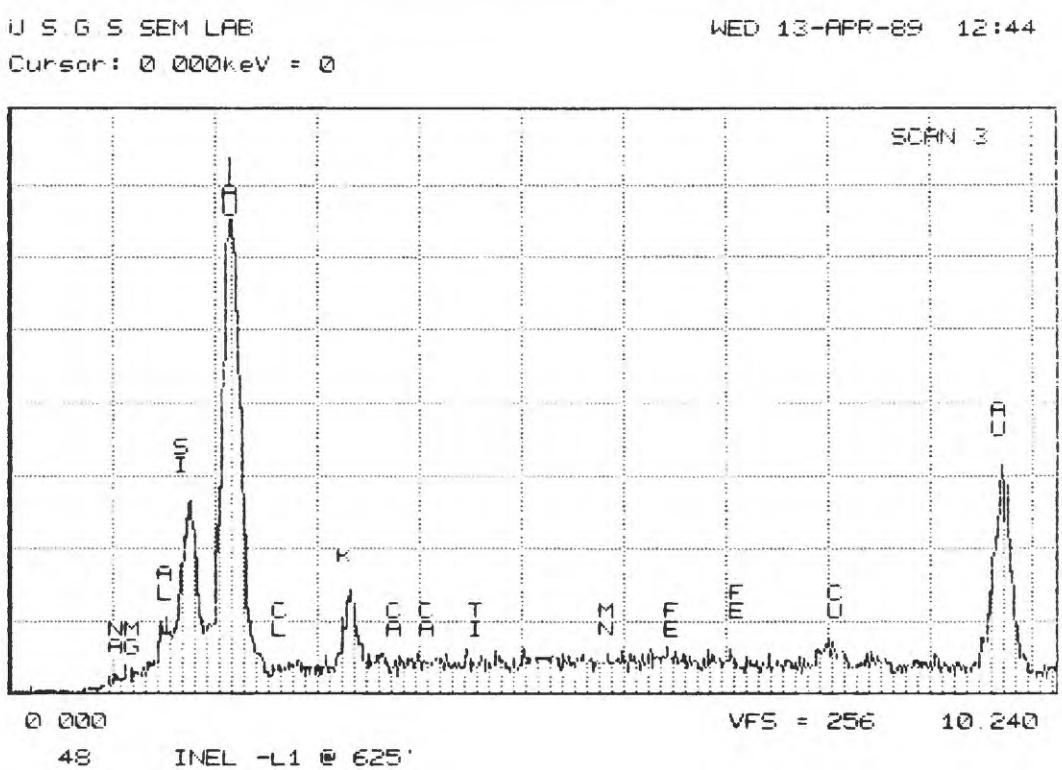

Figure 5. SEM photograph and EDS spectra of the illite coating of all grains.

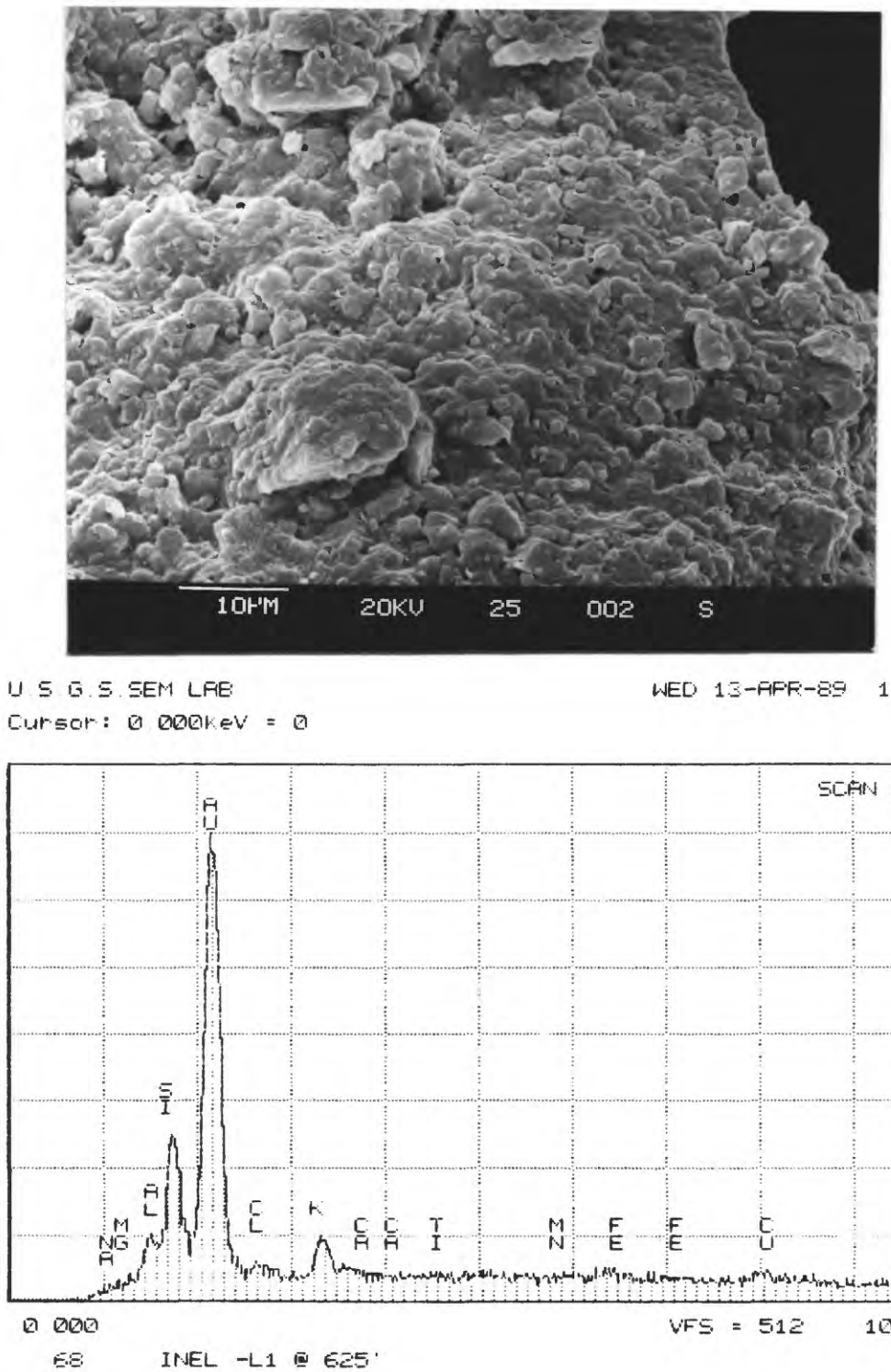

Figure 6. SEM photograph and EDS spectra of the illite coating.

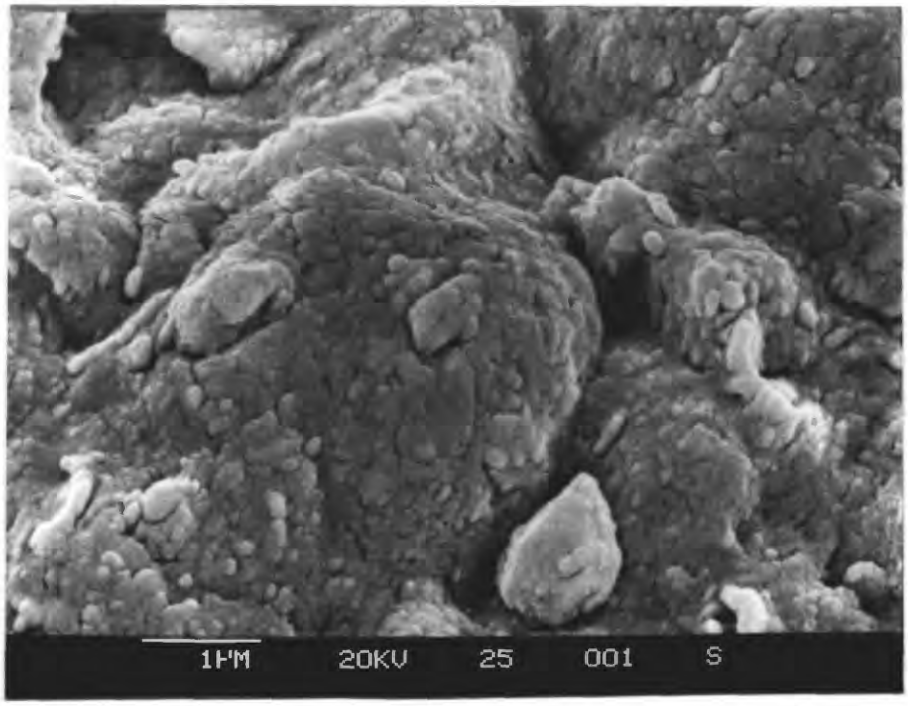

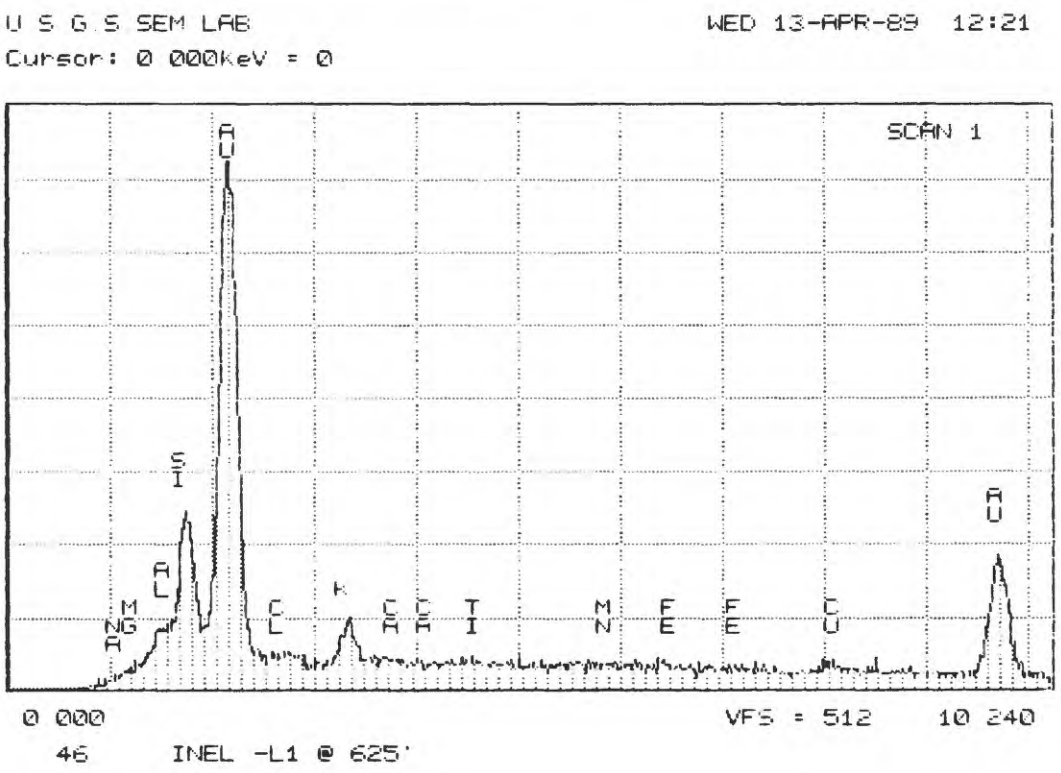

Figure 7. Detail SEM photograph and EDS spectra of illite surface.

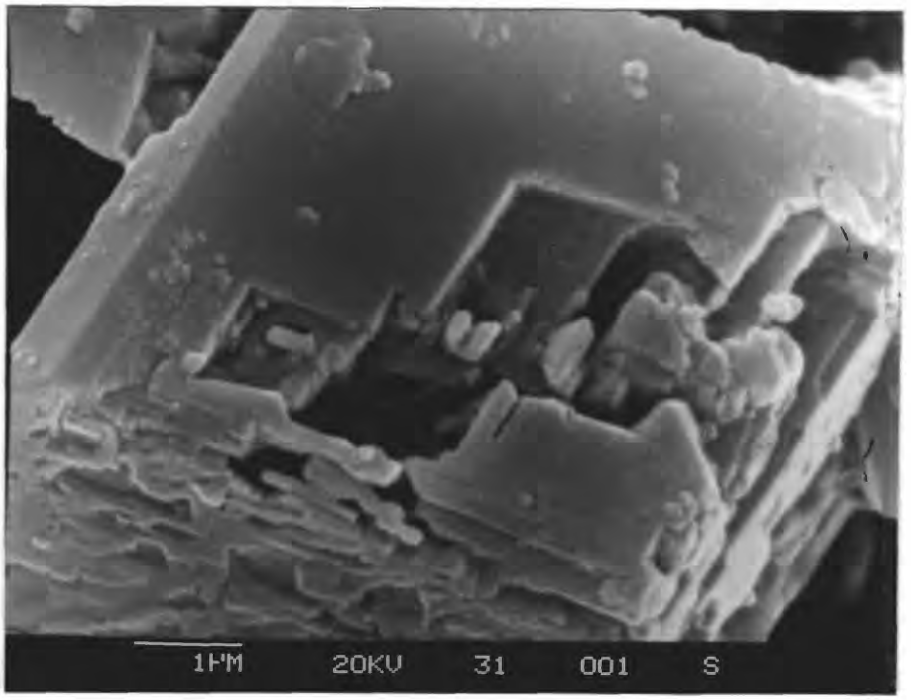

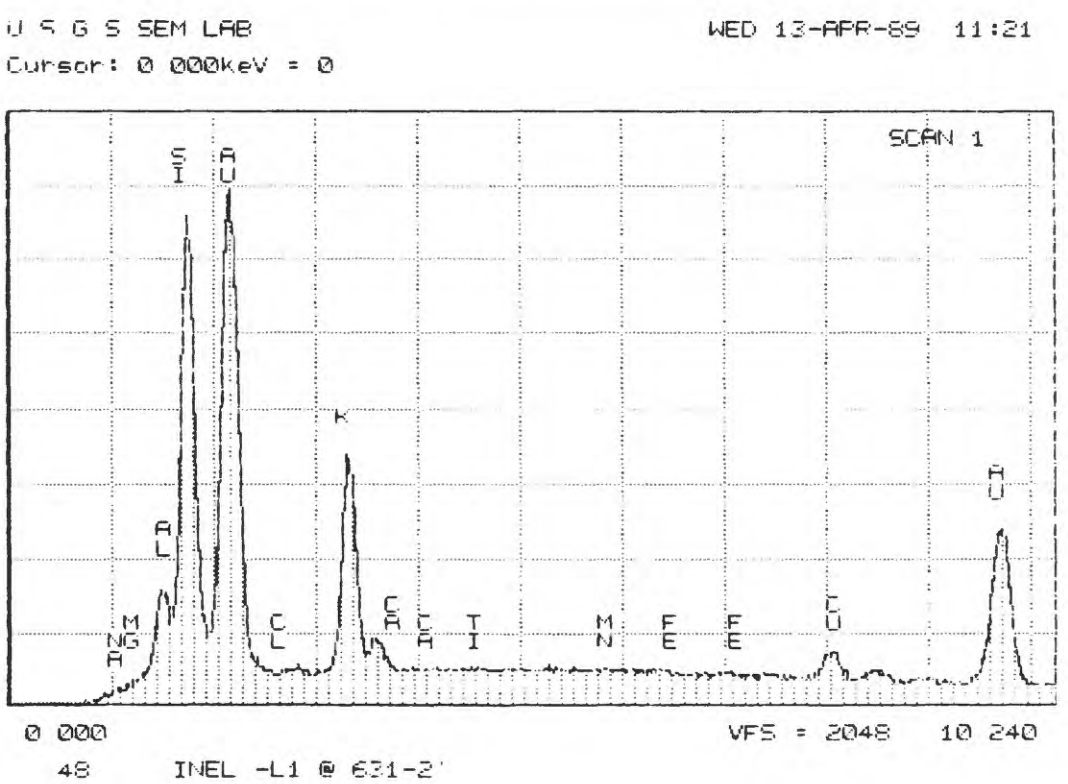

Figure 8. Detail SEM photograph and EDS spectra of the surface of a feldspar rhomb.

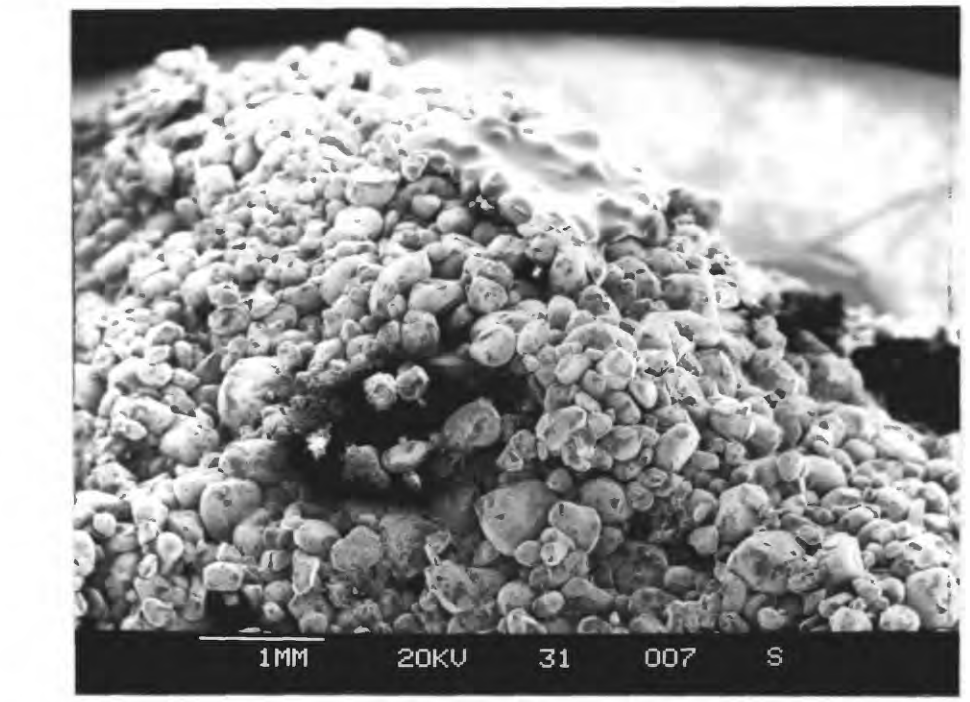

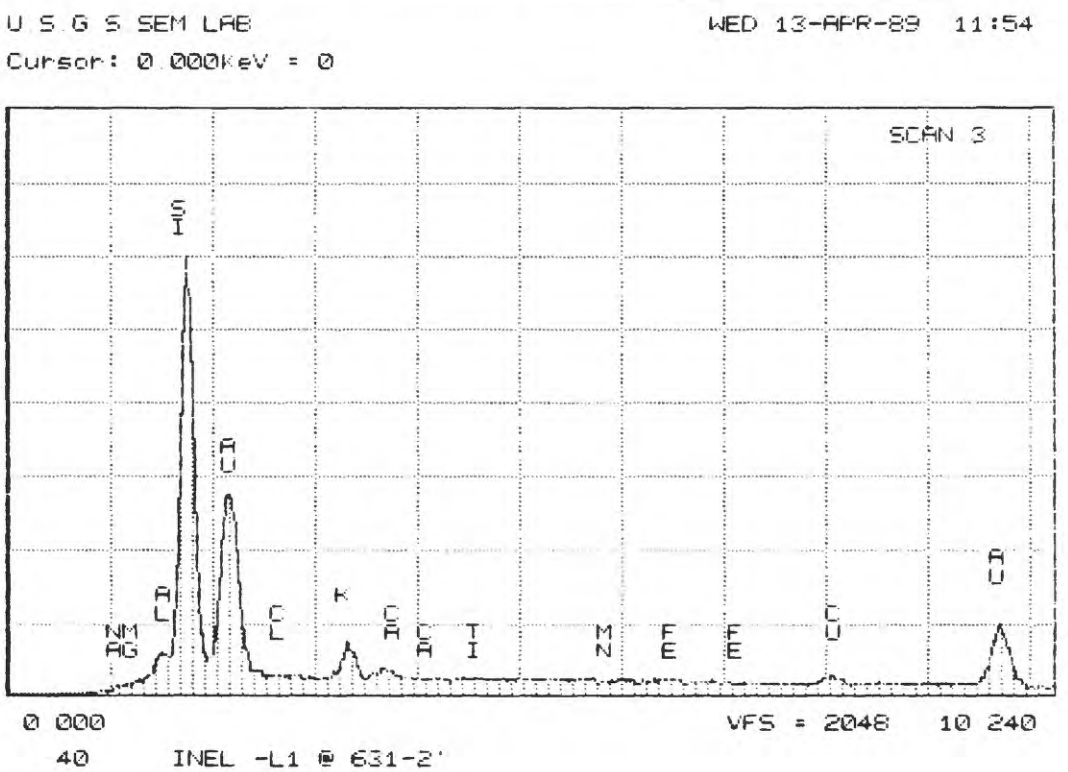

Figure 9. Overview SEM photograph and EDS spectra of a sandstone surface.

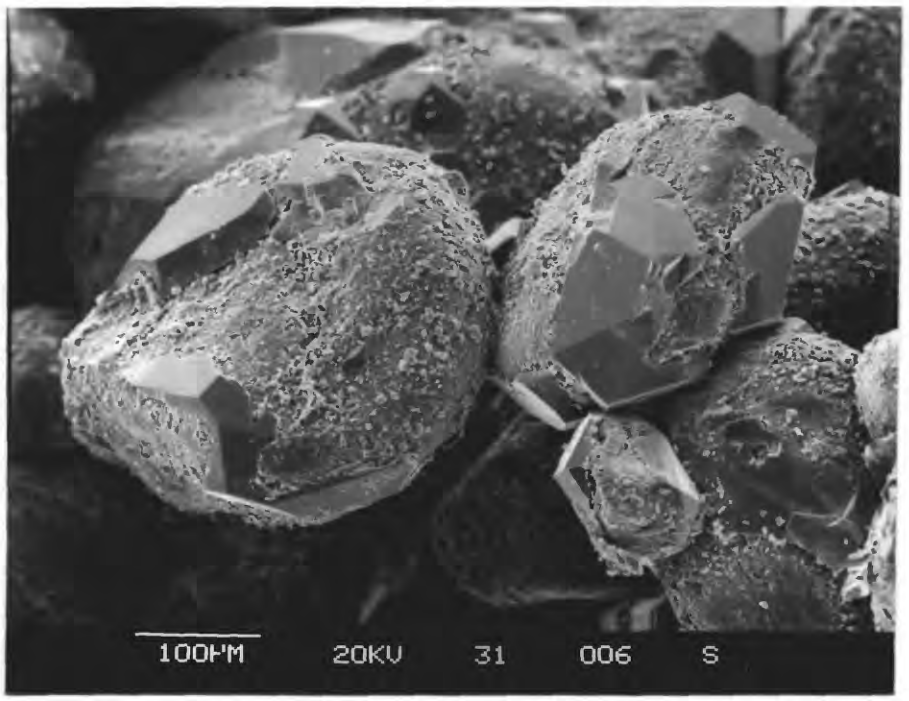

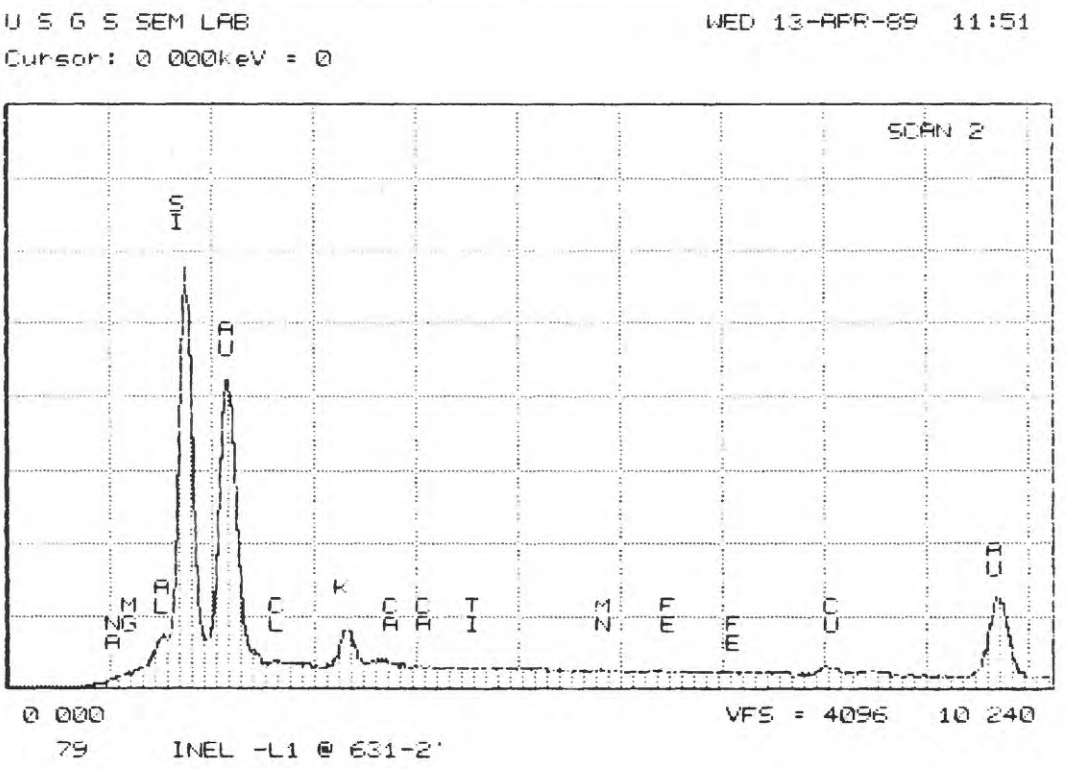

Figure 10. SEM photograph and EDS spectra of sandstone grains and quartz overgrowths.

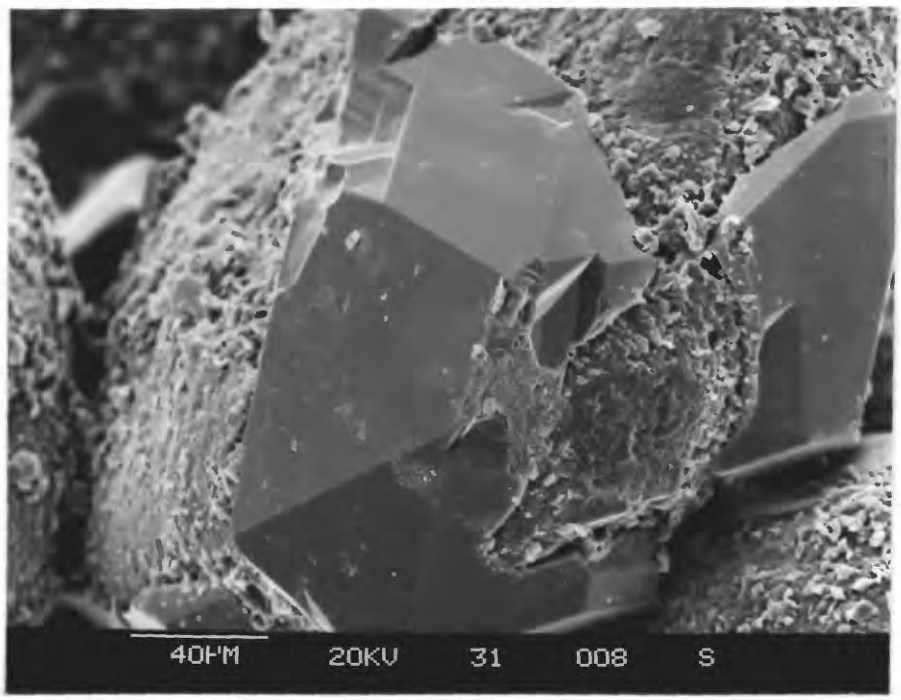

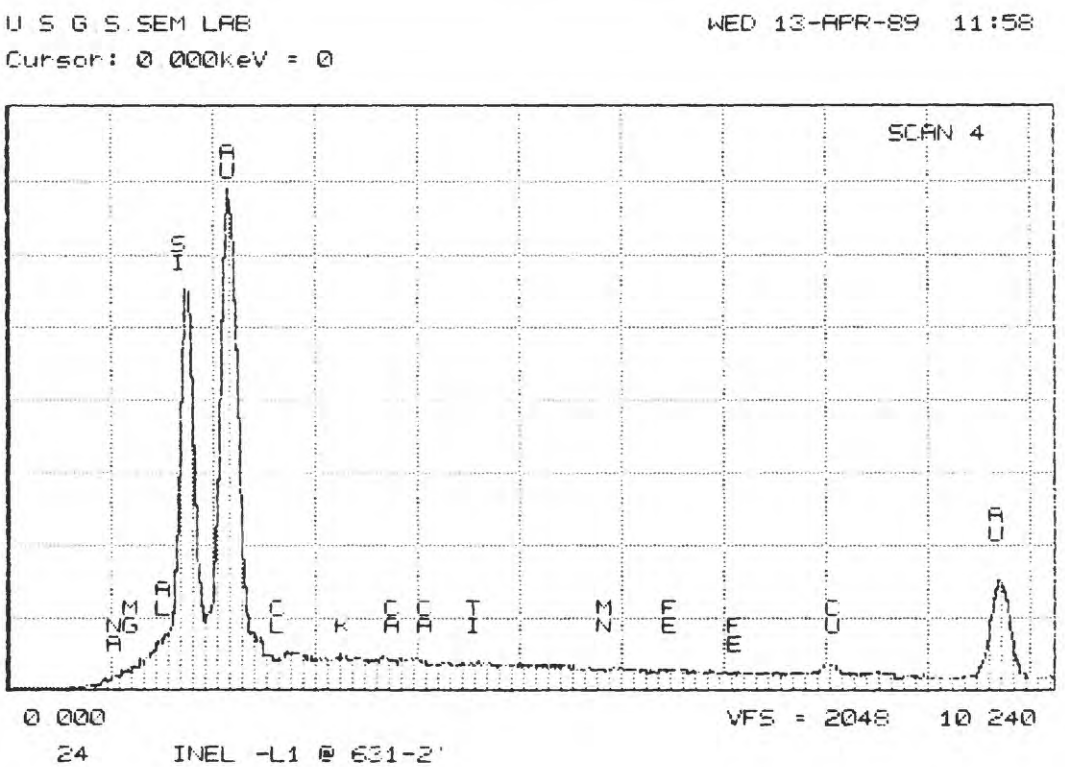

Figure 11. Detail SEM photograph and EDS spectra of a quartz overgrowth.

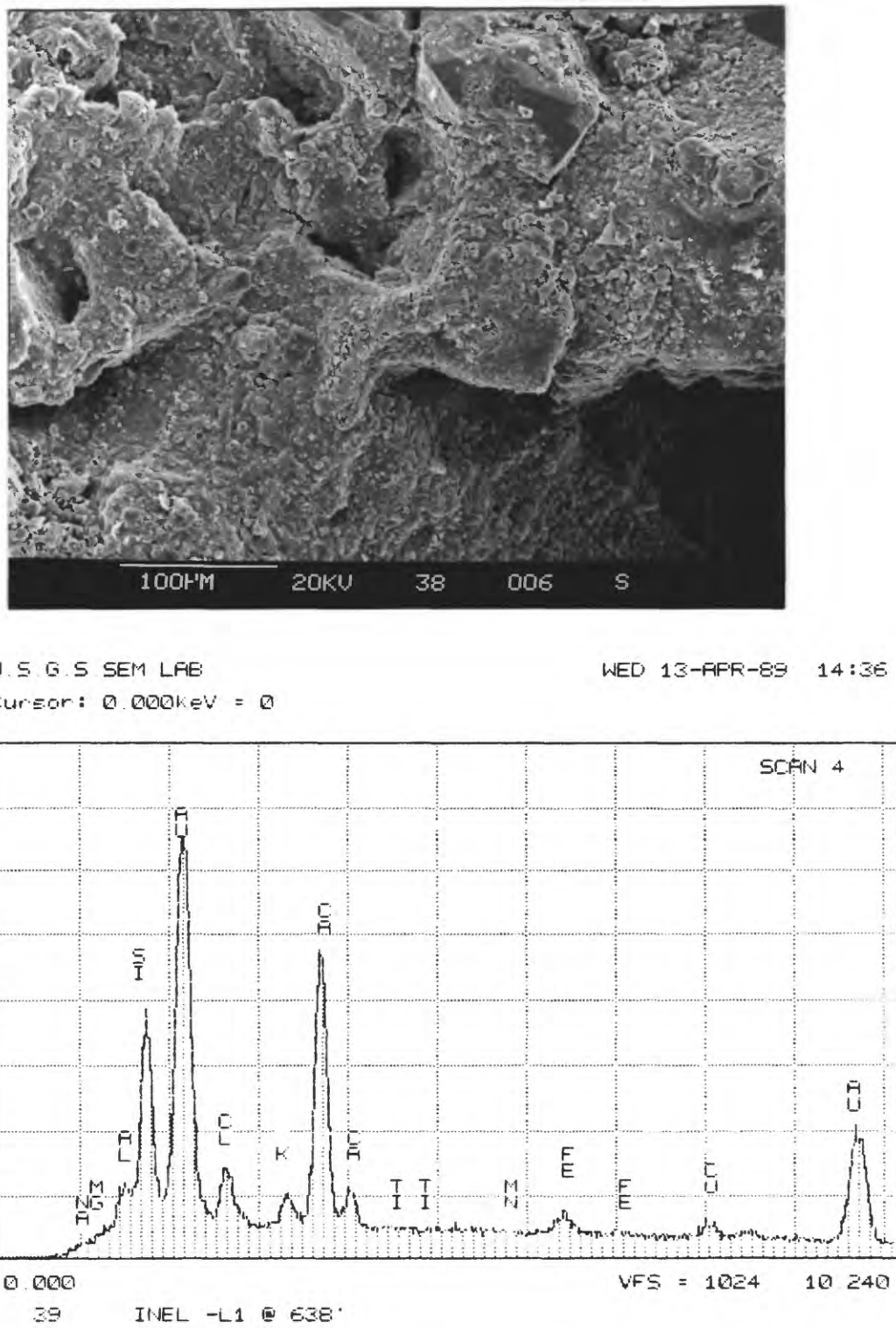

Figure 12. SEM photograph and EDS spectra of a sandstone surface showing clay coating and pore openings.

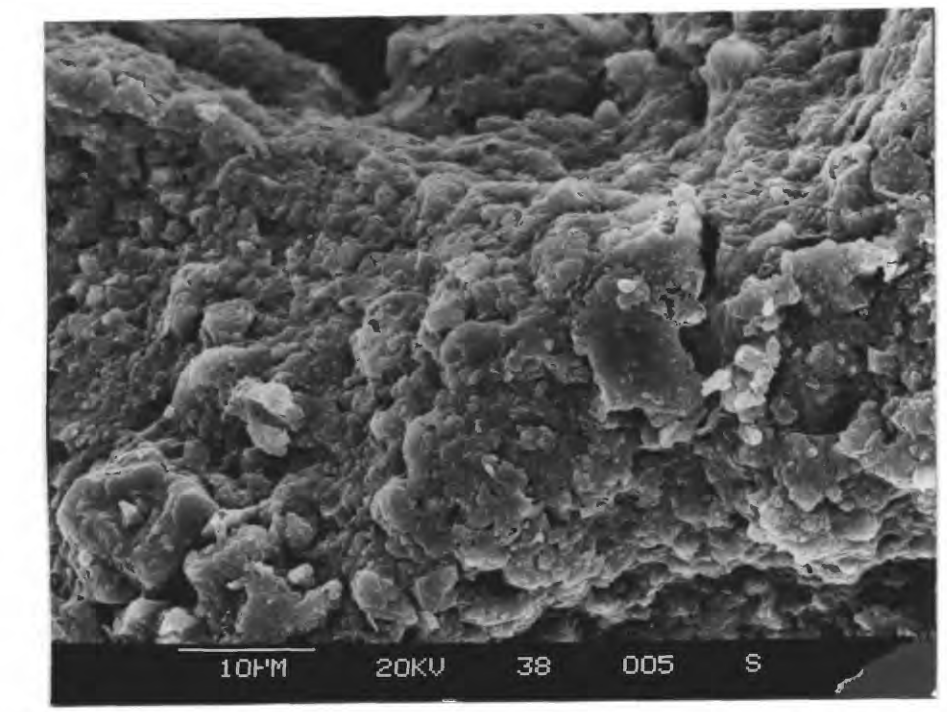

U.S G.S.SEM LAB WED 13-APR-89 14:40
Cursor: 0.000keV = 0

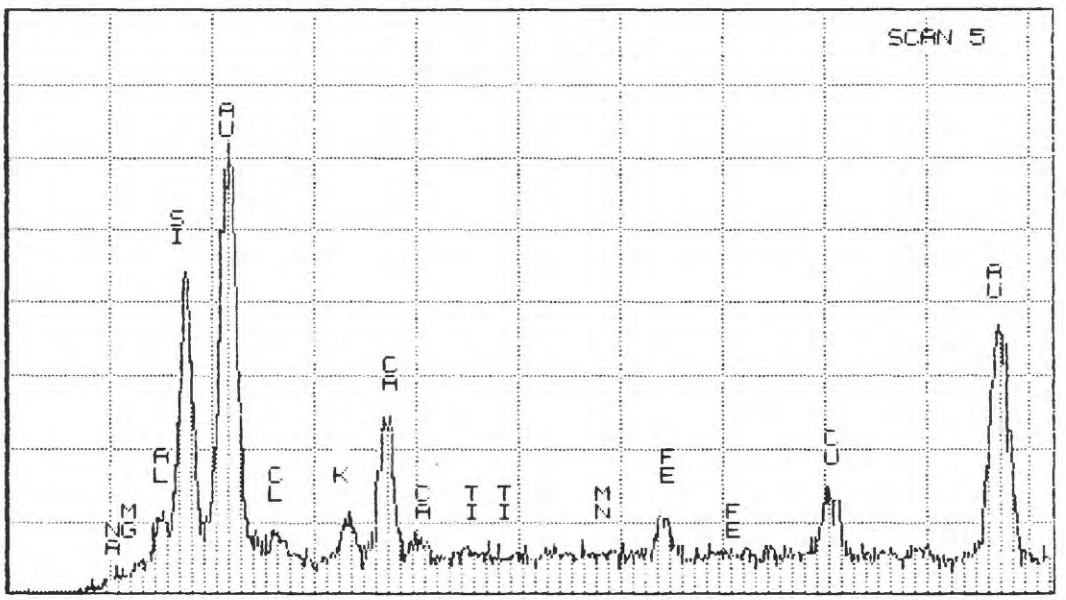

0.000 VFS = 256 10.240
31 INEL -L1 @ 638'

Figure 13. SEM photograph and EDS spectra of the clay coating on the edge of a pore opening.

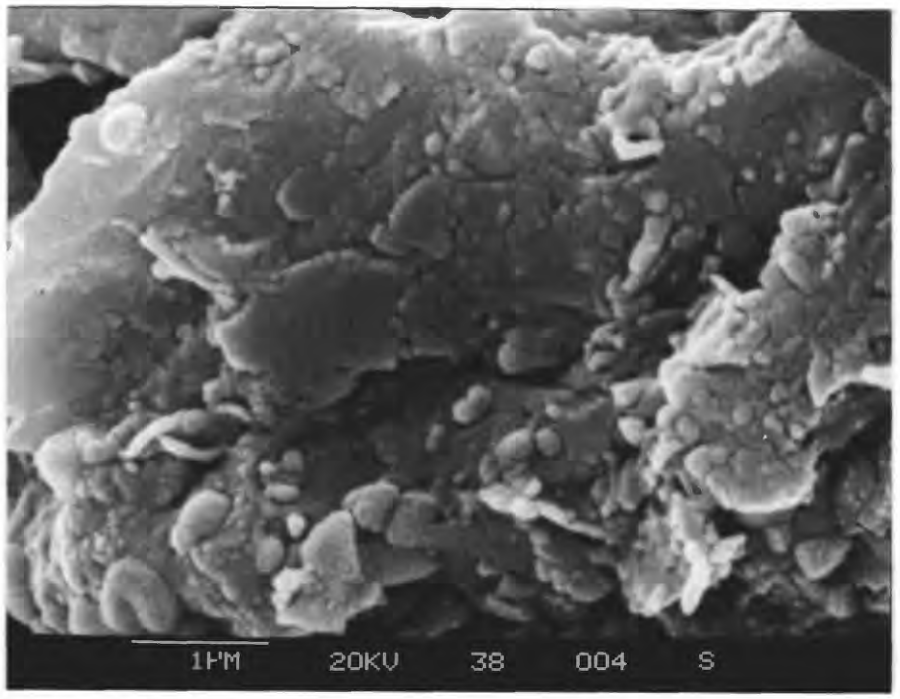

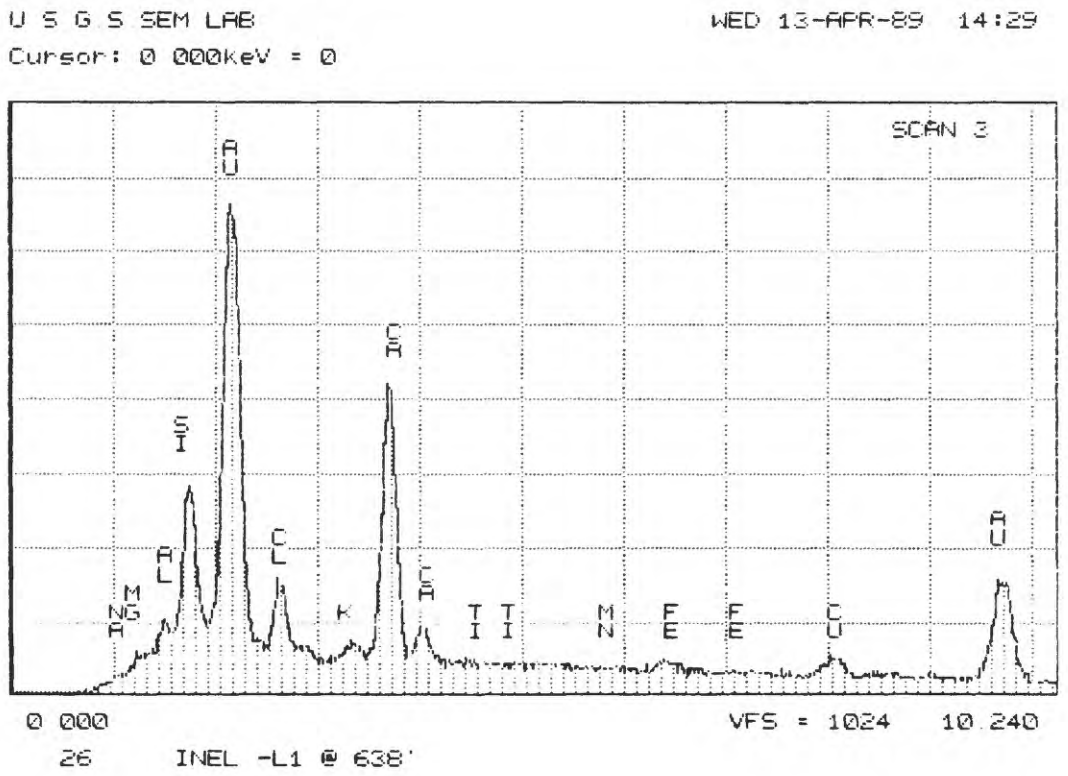

Figure 14. Detail SEM photograph and EDS spectra of clay coating.

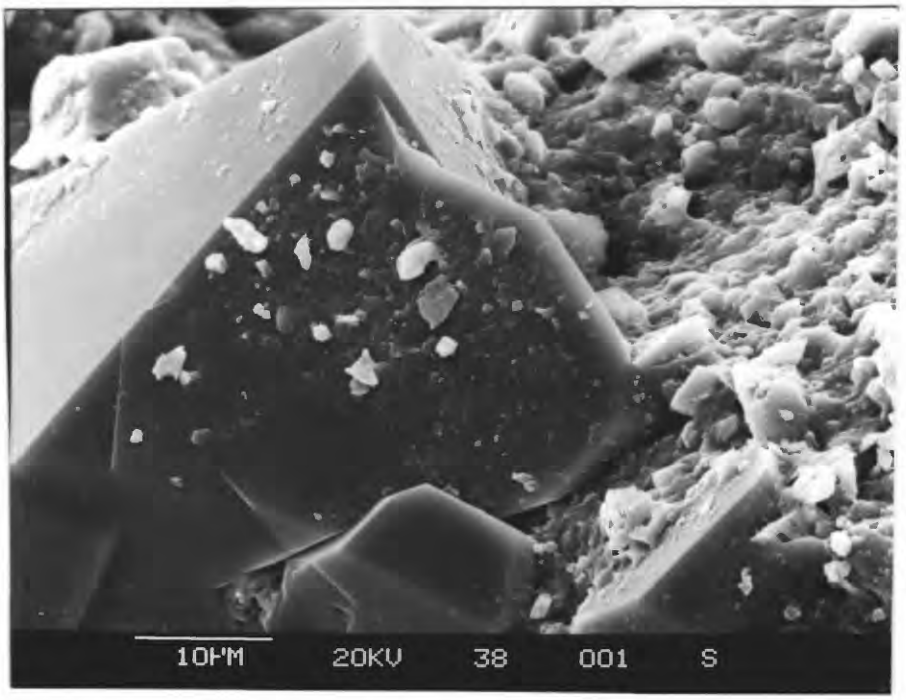

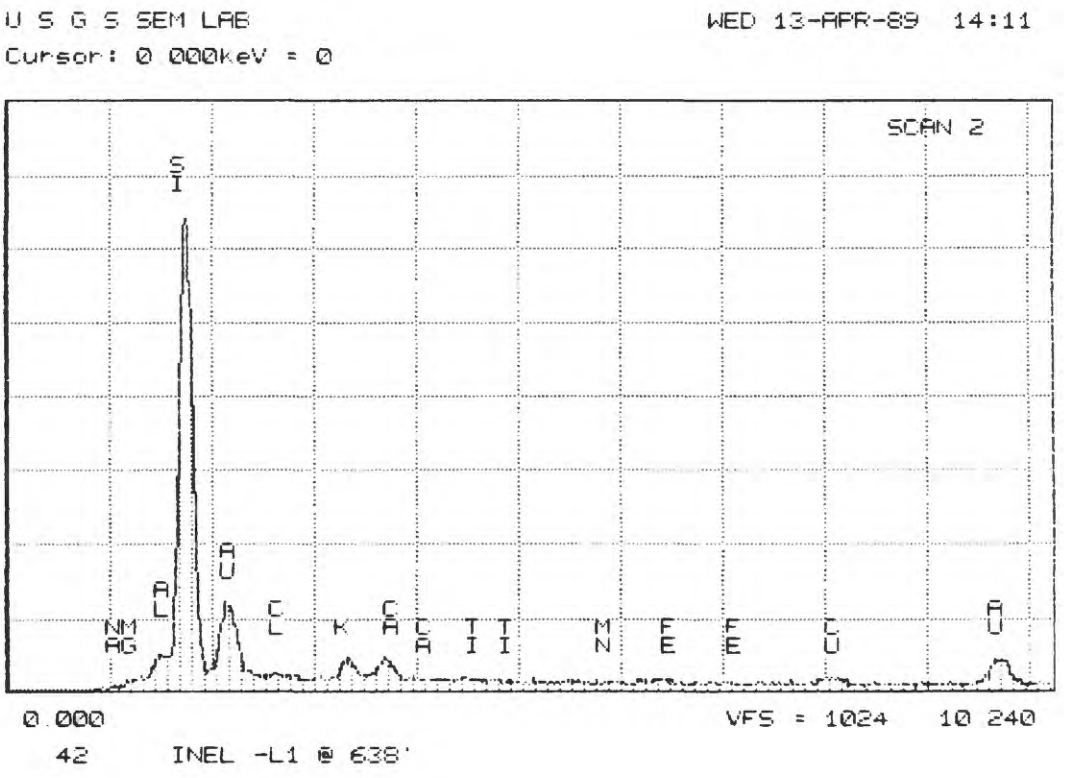

Figure 15. SEM photograph and EDS spectra of a quartz overgrowth with some clay particles on the surface.

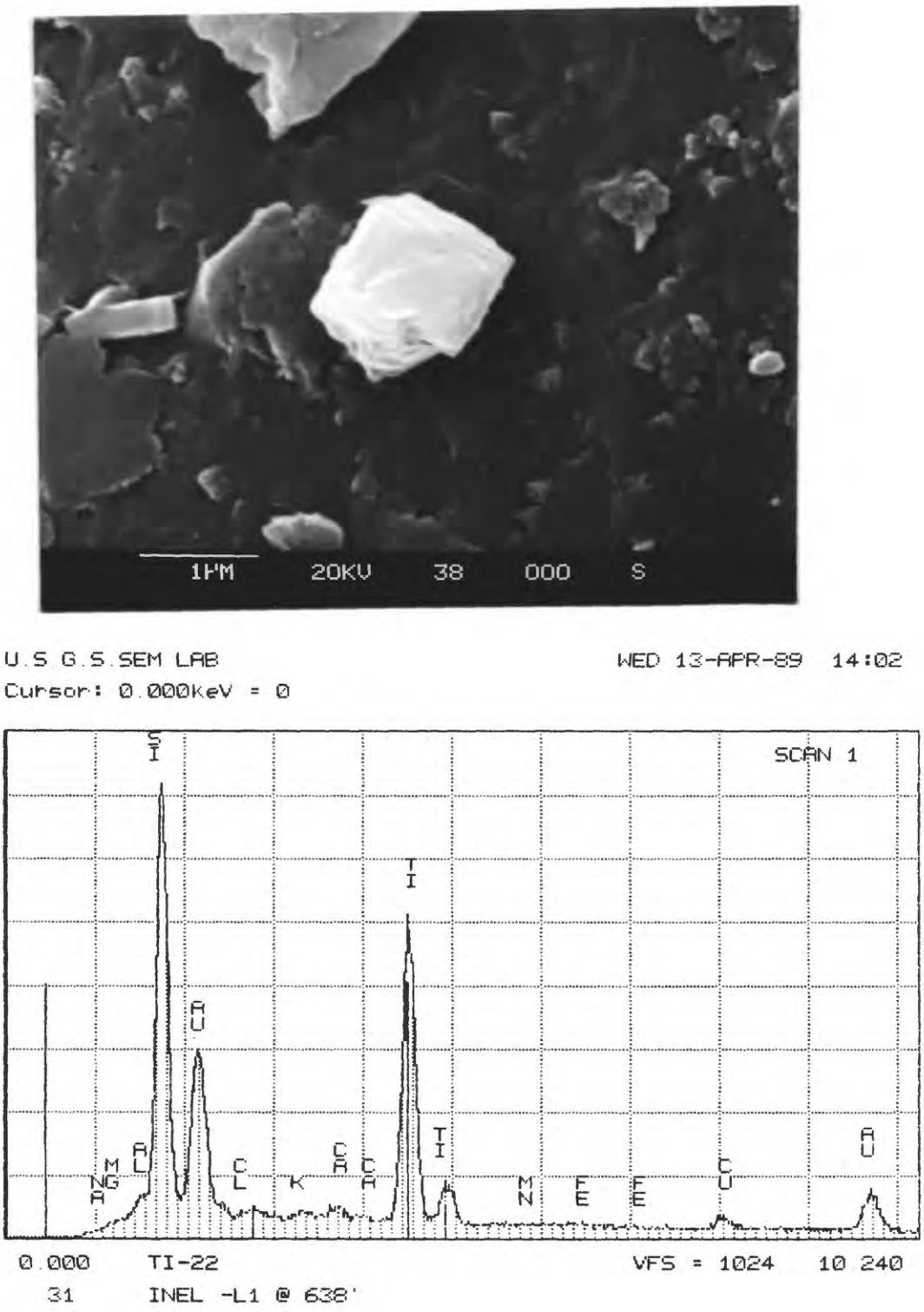

Figure 16. Detail SEM photograph and EDS spectra of a rutile grain.

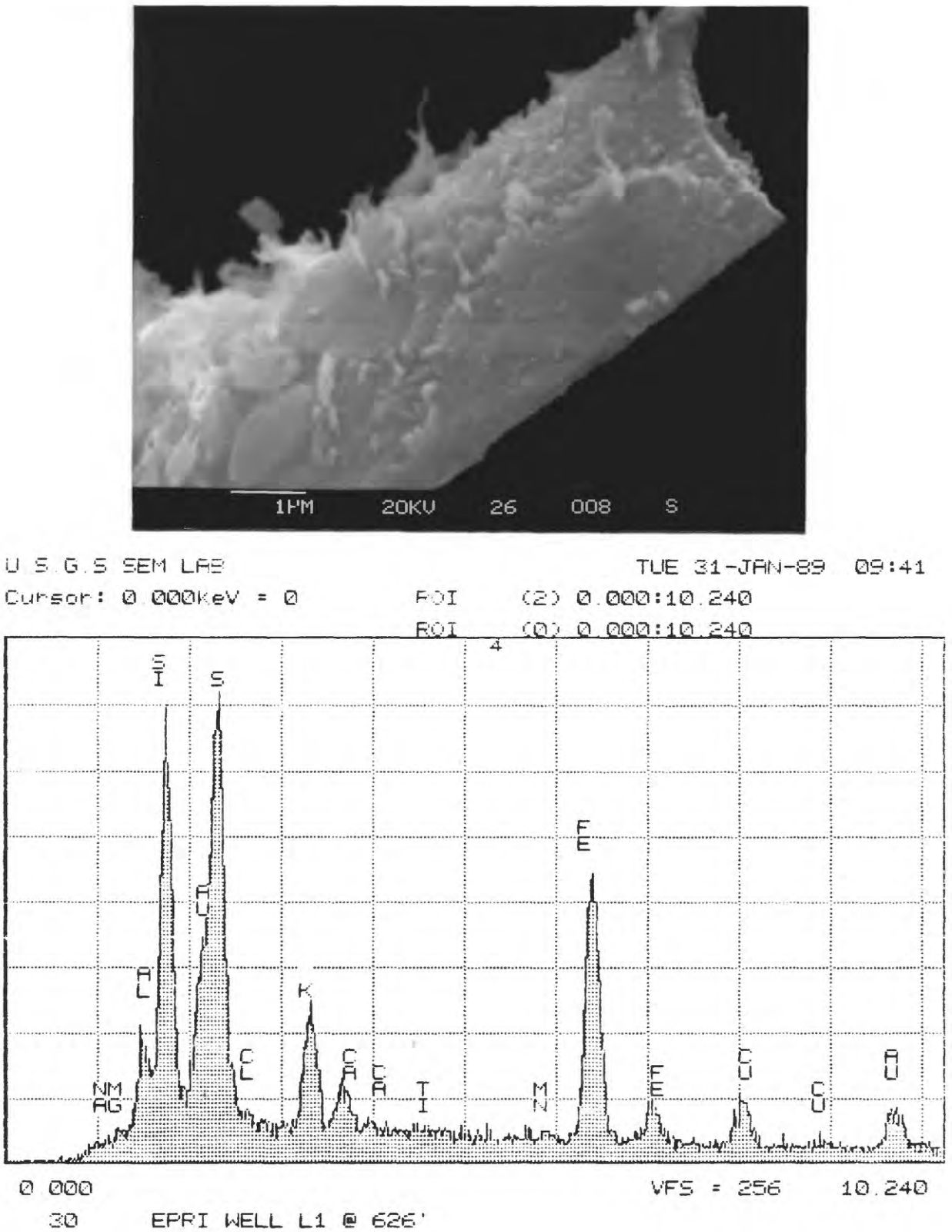

Figure 17. An SEM photograph and EDX spectra of an iron sulfide grain coated with illite.

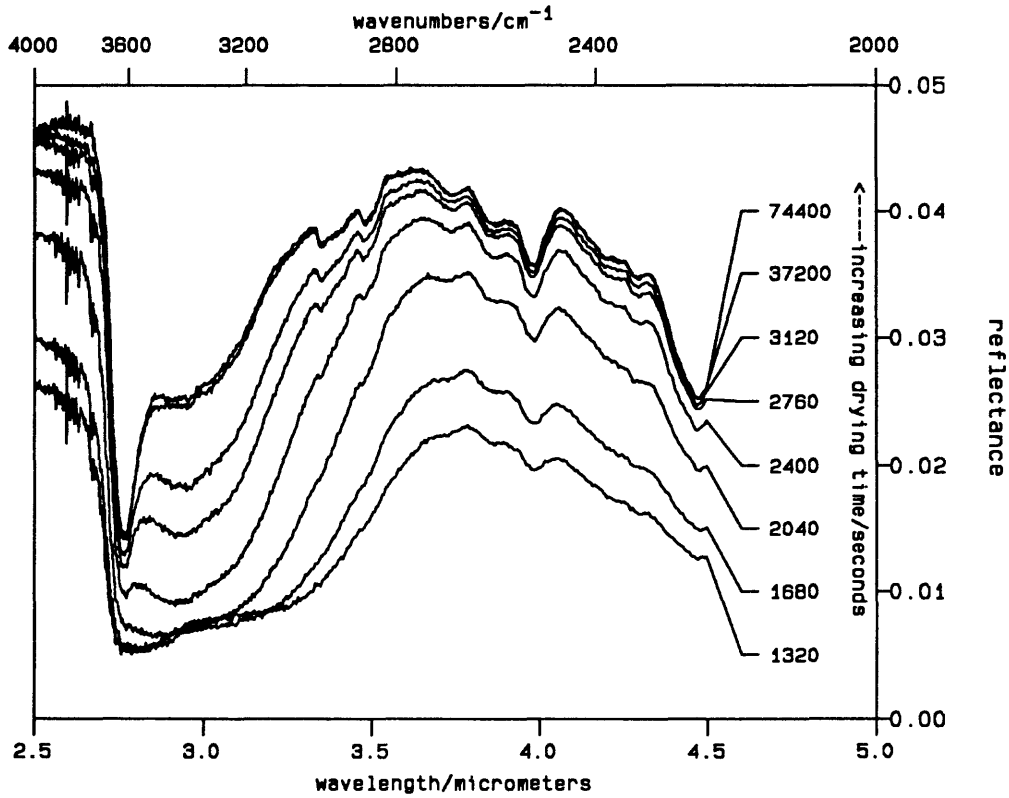

Figure 18 -- This figure shows the reflectance spectra in the 2.5 to 4.5 micron wavelength region of the Pittsfield L-1 625' sample as a function of drying time. The sample was kept from exposure to air and stored in a nitrogen environment prior to the spectral measurements. A humid, oxygen-enriched atmosphere flowed through the sample chamber of the spectrometer. As the sample becomes drier, absorption features which were masked by the absorbed water, become more apparent. Absorption features near 2.7 and 4 microns are attributed to the presence of illite/smectites, and absorption features near 3.4 microns result from carbonates.

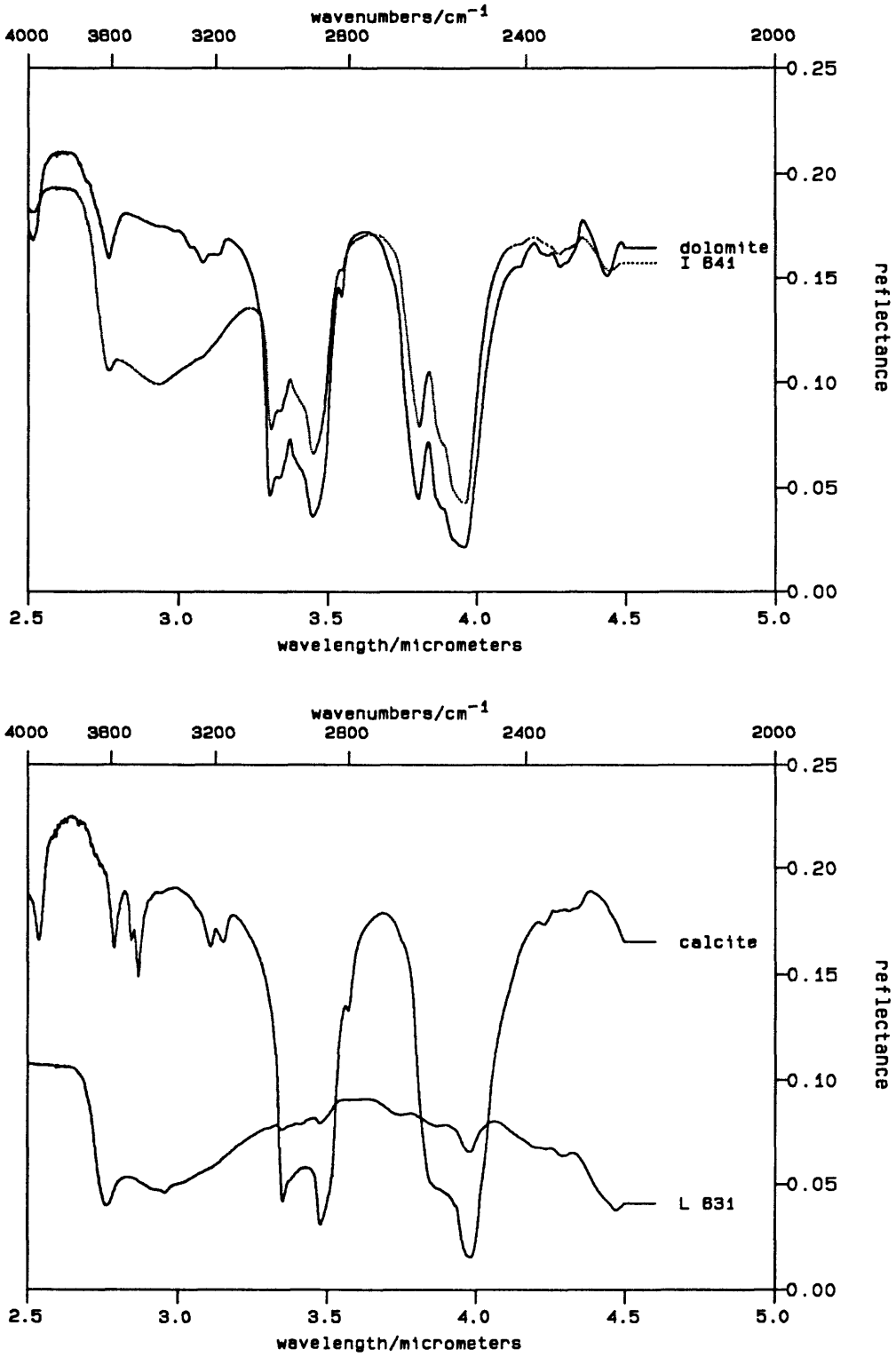

Figure 19 -- This figure compares the reflectance spectra of standard laboratory dolomite with a sample from EPRI well I-1 641' containing dolomite (top), and a standard calcite with a sample from well L-1 631' containing calcite (bottom).

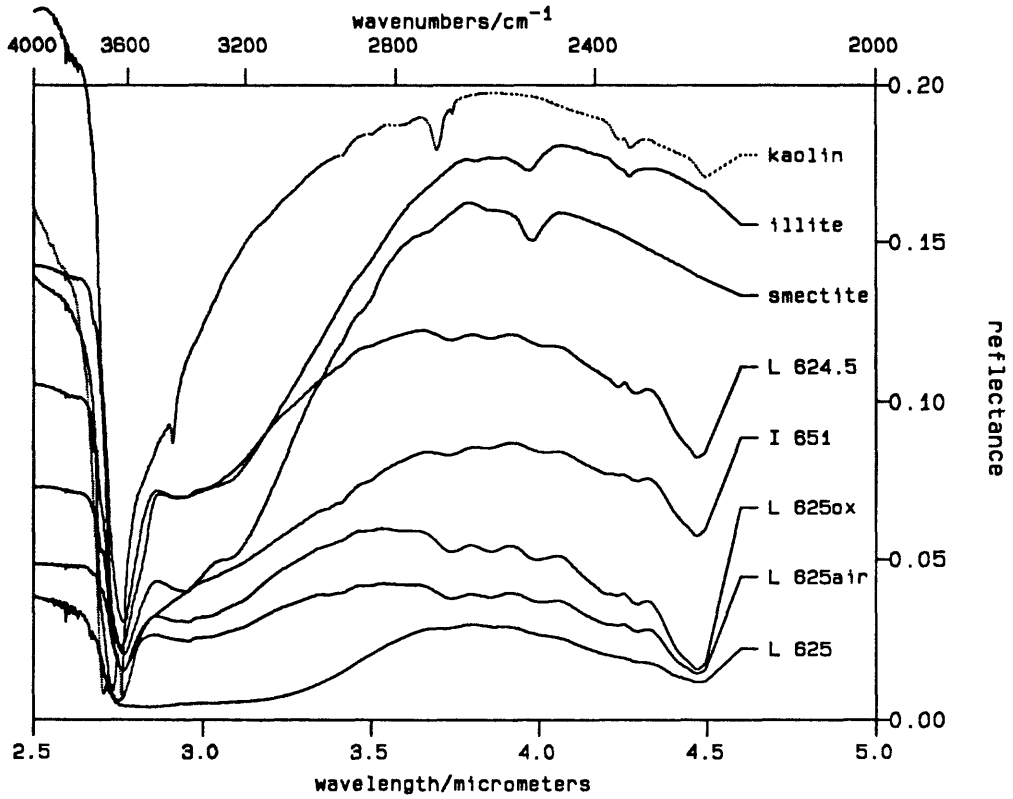

Figure 20 -- This figure shows the reflectance spectra of EPRI samples from the L-1 well at 624.5' and 625', I-1 651' samples, and standard laboratory spectra of kaolinite, smectite and illite. All EPRI samples have absorption features (near 2.7 and 4 microns) which can be attributed to the presence of illite and/or smectite plus carbonate (as in Figure 19). No absorption features can be attributed to the presence of kaolinite which has a characteristic absorption near 3.65 microns.

EXPERIMENTAL METHOD

From May, 1988 to December, 1989 a series of dissolved oxygen, pH, and Eh measurements were conducted on the capability of a variety of materials to affect the aqueous dissolved oxygen balance in a closed system. These materials included Na- and Ca-montmorillonites, kaolinite, fumed silica, illite, pyrite, and pieces of core samples from the EPRI Pittsfield, Illinois, compressed air test facility. All the samples were measured in a neutral solution, and the clays and pyrite were also measured in basic and acidic solutions.

Two sets of EPRI core samples from well L-1 were received. The first set of samples was received in January, 1989, and had been exposed to air. This exposure made the core samples unreliable in so far as quantitative oxygen depletion studies were concerned. However, two specimens were used in SEM and EDX analysis, and as trial samples in the oxygen depletion system. The second set of EPRI core samples from Pittsfield well L-1 were received in April, 1989. These latter core samples were received on the assumption that great care had been taken to exclude them from contact with air since their collection at the well site and subsequent handling by Core Labs. The core samples had been shipped to us sealed under nitrogen, and upon receipt were placed in a sealed glove bag containing a nitrogen gas atmosphere. After twenty four hours, the shipping containers were opened, and the cores were visually examined. Small samples of the individual lithologies were taken. The white sandstone cores were returned to their shipping containers and kept in a nitrogen filled glove bag. The remainder of the cores were individually double sealed in heat-sealed plastic bags and placed in a nitrogen atmosphere glove box.

The repository clays (Appendix B) were vacuum oven dried. The oven was re-pressurized with nitrogen gas. The clays were placed in the sealed glove box for at least three days prior to use.

The water used in this study is of pharmaceutical grade with a resistivity of 1.2×10^5 ohm-meters, produced by a Millipore Milli-RO4/Milli-Q reverse-osmosis filtration system. The water was exposed to air and contained normal atmospheric gasses except where oxygen-free and oxygen-enriched water were used. Oxygen-free water was produced by stripping with nitrogen gas. It was stored in the glove box and used in sample preparation. Oxygen-enriched water was produced by bubbling with oxygen gas. It was added to standard water to increase oxygen content.

The sample material to be tested was mixed with oxygen-free water, loaded into the syringe, and sealed with a flexible polymer film (Parafilm). The sample material was prepared in the glove box in one of two ways, depending on the nature of the sample.

The first method was used with the repository clays in a nitrogen glove box. A quantity of clay was measured into a beaker and mixed thoroughly with a measured mass of oxygen-free water. The produced gel was placed into the barrel of the syringe, sealed with Parafilm, and weighed. The ratio of clay to water in the gel was calculated so the exact amounts of clay and water injected into the flask would be known. The syringe was placed in the glove box's air lock until ready for use.

The second method of sample preparation also occurred in the nitrogen glove box and was used with the pyrite and the EPRI samples. A measured mass of the sample was crushed coarsely in a mortar and pestle and placed directly in the syringe. Enough oxygen free water was added to cover the sample and the whole slurry was brought to the brim of the syringe, sealed with Parafilm, and weighed.

When the loaded syringe was taken from the glove box, it was fitted snugly into half a ground glass joint and sealed with paraffin. Final instrument checks and calibrations were made at this point in the measurement process.

Standard filtered water was collected and any necessary pH adjustment performed. Neutral solutions were not adjusted and usually had a pH near seven. Acid

solutions, pH approximately four, were made by adding hydrochloric acid (HCL). Basic solutions, pH approximately ten, were made by adding sodium hydroxide (NaOH). This water and 150ml of oxygen-enriched water, was used to fill the reaction vessel. Seating the probes, sample assembly, and overflow valve completed the assembly of the reaction vessel. The reaction vessel was placed on a magnetic stirrer within a Faraday shield and the measurement cycle begun.

Eh and pH of the blank system were measured prior to agitation. The system was stirred for two minutes with a magnetic stirring bar before the oxygen measurement. Stirring was stopped for two minutes prior to Eh and pH measurements. Thereafter, oxygen measurements were made in an approximately logrithmic pattern in time while the system was stirred. Eh and pH measurements were made in a similar pattern and after stirring was halted for two minutes. After twenty three minutes of stabilization time, the overflow valve and hose were opened, and the sample was injected into the reaction vessel. Depressing the syringe plunger ruptured the Parafilm covering, expelling the sample and free syringe stopper into the oxygenated test solution. The duration of the measurement cycle was approximately twenty four hours. The general presentation of data is given in Figures 21 through 48. Comparison of measurement cycles with different sampling points was made using a cubic spline interpolation computer program to calculate the oxygen values for each minute of the measurement cycle. Examples of the oxygen comparisons are shown in Figures 50 through 68.

CALIBRATION

The oxygen probe and Eh meter are calibrated according to specifications outlined in their operating manuals (Orion Research, 1978 and 1983). The oxygen probe has a battery check, an instrument zero, and an air calibration. The air calibration uses the oxygen partial pressure of water-vapor-saturated air as a calibration standard. The saturated air standard for calibrating the oxygen probe is the probe storage container which contains approximately 20ml of water. This container is sealed when not in use for storage and maintains a water saturated atmosphere. The calibration setting reads out as one hundredth of the atmospheric pressure. The air pressure is checked using a mercury barometer. Adjustments to the internal amplifier are made if necessary. The optimum oxygen range for the Orion oxygen probe is 0 to 14 parts per million (ppm).

The pH system is calibrated using two solutions of different pH, 4.01 and 6.86, using the calibration and temperature adjustments to balance the readings to properly read the differing solutions.

There are no calibration procedures recommended for the redox system. Proper operation is checked by measuring solutions of potassium ferricyanide, potassium ferrocyanide, and potassium flouride to determine the relative value of the redox potential between them. The Eh system was very stable and potential difference changes between solutions of greater than ten millivolts from normal indicated the need to change reference solutions or probes. The probes were changed once.

After the measurement cycle is complete, the oxygen probe is re-calibrated to show the amount of drift that has occurred. The pH system is very stable and does not change over a week's span of time.

RESULTS

The results of the dissolved oxygen, pH, and Eh measurements are presented in Figures 21 through 48. Also included in the figures presenting the data is the Eh value calculated from the formula for the O_2-H_2O couple

$$Eh = 1.220 - 0.074 \log PO_2 - 0.059\ pH \qquad \text{(in volts)}$$

as initially given in the introduction. The pH is adjusted using hydrochloric acid or sodium hydroxide buffering to make the system initially acidic or basic (no buffer is used for neutral). As the Eh measurements were not tied to an absolute calibration

standard, the formula used to fit the data was

$$Eh(pH) = E_0 - 59\ pH\ (\text{in millivolts})$$

where E_0 was fixed by the Eh and pH values just prior to injection (or the first measured values for blank runs). The -74 log PO_2 dependency upon oxygen term was found to be insignificant compared to the pH and neglected (PO_2 contributed less than 16 mV to the observed changes in Eh, compared to hundreds of mV due to pH changes).

Injection of oxygen-free water and sample material diluted the oxygen-enriched water in the reaction vessel. The amount of oxygen-free water injected ranged from three milliliters to thirtysix milliliters. The volume of sample injected ranged from two milliliters to twelve milliliters. This would have diluted the total amount of oxygen in the system in the range of 0.4% to 0.38%. If the initial solution had an oxygen content of ten ppm, dilution losses would have been in the range of 0.04ppm to 0.38ppm.

The blank system response with no material injected into a sealed system is seen in Figure 21. There is a slow change with time as the system comes to equilibrium and the instruments drift. There does not appear to be significant oxygen escape by leakage around or through gaskets and seals. The calculated Eh values are in close agreement with the measured values, indicating that Eh is controlled by pH in the O_2-H_2O couple.

The system response of basic, acidic, and neutral systems with only oxygen-free water injected into them is shown in Figures 22, 23, and 24 respectively. The close agreement of theoretical Eh values with the measured values indicates no reaction occurring other that caused by the O_2-H_2O couple. The value of Eh is dominated by the value of pH.

The responses caused by fumed silica and kaolinite (KGa-1) injected into neutral water are shown in Figures 25 and 26. The oxygen loss is due to system losses. System losses consist primarily of oxygen exolving from solution, forming bubbles, and secondly of oxygen leaking through the greased joints and seals of the system, though this appears to be minor (Figure 21). There is no observed oxidation reaction caused by the injection of these samples.

Gene Whitney, U.S.G.S., personal communication, suggested that the cause of Eh and pH variations seen when clay is injected into a sealed system (Figure 27) could be explained by clay particles adhering to the Eh and pH electrode probe surfaces. Thus, the clay surface would be the substance measured instead of the aqueous system. To test this hypothesis, the Eh and pH probes were covered with a a Spectrapor brand dialysis membrane with a molecular weight cutoff of twelve to fourteen thousand grams per mole. To test the effect of only the dialysis membrane a blank, no injected sample, system measurement was performed. The results are presented in Figure 28. Eh and pH results are in close agreement with Figure 21. Next a Na-montmorillonite clay was injected into the system duplicating the conditions of Figure 27, except for the dialysis membranes (Figure 29). The response of this setup replicates the response of Figure 27 but is slower due to the time delay caused by diffusion through the dialysis membranes. Thus, the pH and Eh measurements accurately reflect the properties of the aqueous system, not just the clay.

When pyrite is injected into an aqueous system, its capability to deplete oxygen from that system is controlled by on pH. Figures 30, 31, and 32 show this clearly. Also indicated by the different characters of the calculated and observed Eh, is that a chemical process other that the O_2-H_2O couple is occurring and controlling Eh. This reaction is the oxidation of the iron in pyrite. The oxygen depletion from solution caused by pyrite in the three systems can be seen in Figures 50, 51, and 52. Figures 32 and 52 show th most PO_2 loss, and Figures 30 and 50 the least. The discrepancy between the low strength of the oxidation reaction indicated by the Eh curves, and the severe loss of PO_2 can be explained by the dominance of pH in calculating Eh. A constant rate of production of sulfuric acid from the oxidation of pyrite would change the pH of the basic solution slowly at first and then more quickly as the pH of the

solution approached neutrality. Figure 32 exhibits this behavior.

The responses of acidic, neutral, and basic aqueous systems to the injection of Ca-montmorillonite are shown in Figures 33, 34, and 35 respectively. In acid and basic solutions, the system is controlled by pH, as indicated by the close agreement of calculated and measured Eh. There is a slight loss of oxygen in the acid system. In the neutral system, the cause of the divergence between calculated and measured Eh indicates that a mild reduction reaction is occurring, or oxygen was added to the system. A slight increase above system losses in measured oxygen is shown in Figure 54. The entrance of extra oxygen is a possible explanation to the appearent reduction reaction occurring in Figure 34. Its entrance from outside the system, from the atmosphere, is unlikely since the partial pressure of oxygen in the system is greater that atmospheric oxygen partial pressure.

No significant loss of oxygen was caused by injecting Na-montmorillonite into acidic, neutral, or basic aqueous solutions. Eh and pH varied in a typical clay fashion, and there is close agreement between calculated and observed Eh. This data is presented is Figures 36, 37, 38, 56, 57, and 58.

The responses caused by injection of illite (IMt-1) into acidic, neutral, and basic aqueous solutions are shown in Figures 39, 40, and 41 respectively. In neutral and basic solutions, the controlling condition appears to be pH, and the changes in pH and Eh are typical of those caused by montmorillonites: a rise in pH and a drop in Eh values. In an acidic environment, there is an oxidation reaction indicated by the divergence of the calculated and measured Eh values, though there is no significant loss of measured oxygen (Figures 59, 60, and 61).

Both of the tested L-1 samples from the first set of cores had been exposed to air. Their responses to a neutral aqueous solution (Figures 42, 43, 62, and 63) are similar to Figure 34 (Ca-montmorillonite in neutral water). There is mild reduction reaction indicated. Net oxygen loss characteristics are shown in Figures 62 and 63 and are probably due to the exposure of metallic iron when the stirring bar coating wore away..

The sample from the L-1 core at 624.5' was not exposed to air. The response it caused in a neutral aqueous solution is shown in Figure 44. There was no significant loss of measured oxygen caused by this sample (Figure 64). However, an oxidation reaction is indicated by the calculated and measured Eh values. In character, the measured Eh curve resembles both Figure 31 (pyrite in neutral water) and Figure 39 (illite in acidic water). The pH curves in these two latter figures change in opposite directions in response to their respective samples. It appears that both pyrite and illite exist in the 624.5' sample, and that both affect the Eh and pH response.

The measurements from the L-1 core samples injected into acidic, neutral, and basic aqueous solutions are given in Figures 45, 46, and 47 respectively. The initial low pH of the neutral solution is caused by the addition of 11μg of $HgCl_2$ to arrest any biological growth. There is a significant loss of dissolved oxygen caused by this sample in neutral environments (Figure 66). In acidic and basic environments, there is no significant loss measured (Figures 65 and 67). In character, the Eh and pH responses of Figures 45 and 46 resemble Figure 36 (Na-montmorillonite in acidic water) and Figure 40 (illite in neutral water). In Figure 46, an oxidation reaction is indicated. The character of Figure 47 most resembles that of Figure 41 (illite in basic water) and Figure 38 (Na-montmorillonite in basic water). A very mild oxidation reaction is indicated by the calculated and measured Eh values.

The L-1 core sample from 631' was measured in neutral water with 11μg of $HgCl_2$ added (Figure 48). There was no significant oxygen loss caused by this sample (Figure 68). It resembles Figure 36 (Na-montmorillonite in acidic water), and there is a slight oxidation reaction indicated.

The stability field for an aqueous system containing oxygen, sulfur, and iron as a function of Eh and pH is shown in Figure 49. The samples of pyrite that have been

measured (Figures 30, 31, and 32) when compared to Figure 49, indicate that the region where $Fe^{++}aq$ is stable is where the Eh and pH are headed with time. That is towards a relatively acidic environment with moderate to high values of Eh. The small changes and lack of oxygen consumption shown in Figure 30 are offered as confirmation.

The chemical changes indicated by Figures 34, 39, 42, and 43 when compared to Figure 49 indicate a regime where hematite is stable. Any free or reduced iron would be oxidized quickly. The pH and Eh values of all the clays indicate stability in this hematite field. The exception is Figure 44. It appears to be in the border area between $Fe^{++}aq$ and hematite stability. It probably contains both illite and pyrite. Yet the oxygen consumption is low. Plumlee and Ridley's (1989) modeling studies show that an iron bearing clay would buffer the effect of pyrite oxygen consumption. Figure 44 seems to corroborate this result.

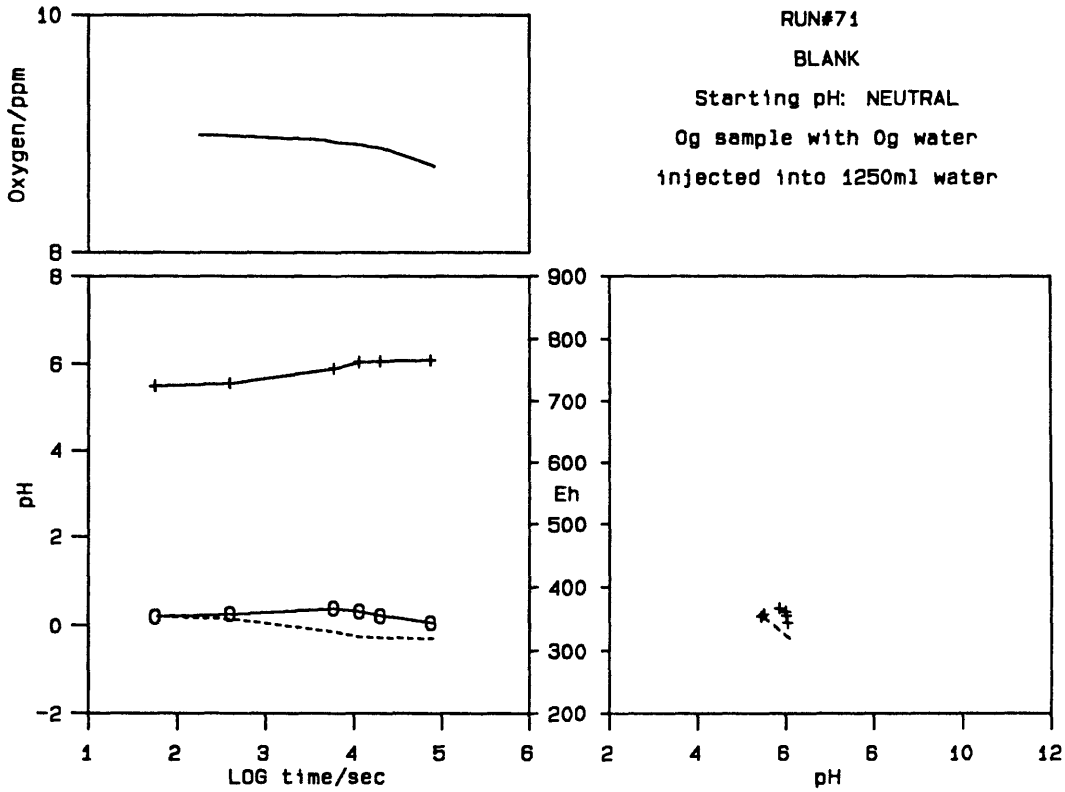

Figure 21 -- This figure demonstrates the stability and drift of the measurement system with a blank run -- the sample holder is filled with pharmaceutical grade water containing 9 ppm dissolved oxygen and stirred without disturbance at neutral pH for 10^5 seconds. In the lower left sub-plot, the solid line with pluses is the measured pH data (left scale), the solid line with O's is the measured Eh data (right scale), and the dashed line is the Eh predicted from the equation for the O_2-H_2O couple using the measured pH data (the partial pressure of oxygen has a negligible contribution). In the Eh-pH plot to the right, the dashed line similarly traces the projected Eh(pH)-pH line for the O_2-H_2O couple. Small differences between the dashed line and the measured Eh data indicate relatively inactive chemistry. In this case, the differences between measured and expected Eh are indicative of measurement repeatability and drift stability.

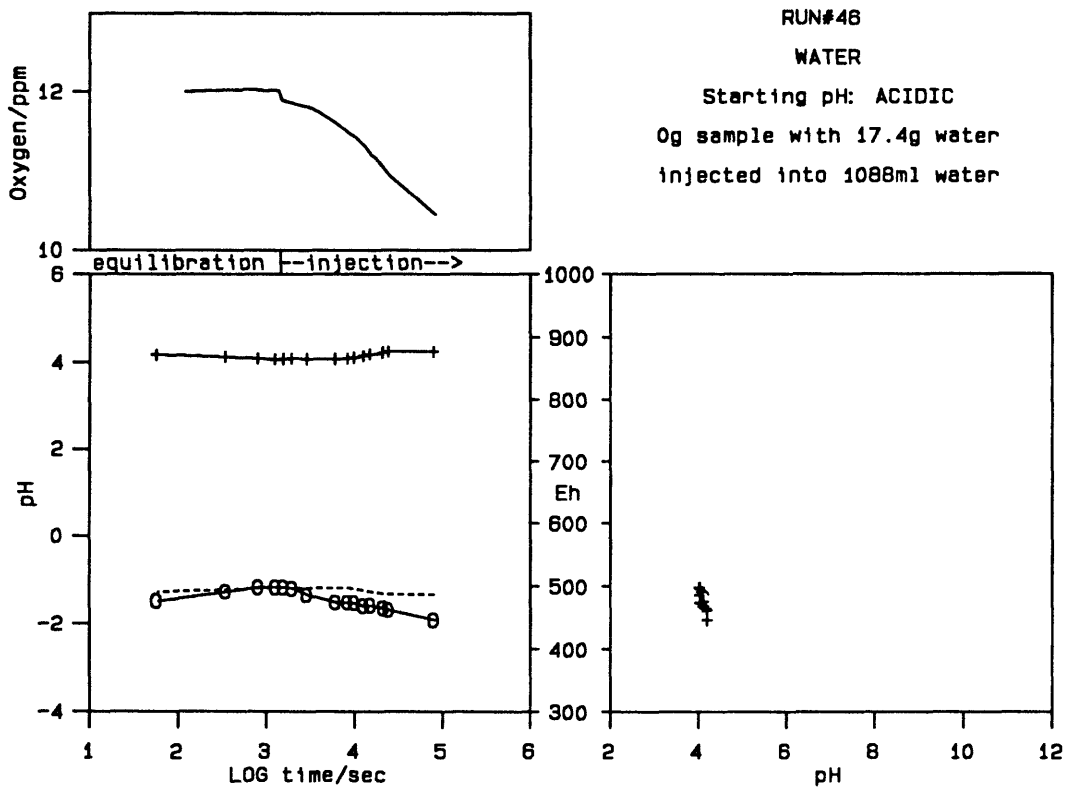

Figure 22 -- This figure demonstrates the stability of the measurement system to physical disturbance by injection of neutral water into acidic water at acidic pH 4 buffered by HCl. In the lower left sub-plot, the solid line with pluses is the measured pH data (left scale), the solid line with O's is the measured Eh data (right scale), and the dashed line is the Eh predicted from the equation for the O_2-H_2O couple using the measured pH data (the partial pressure of oxygen has a negligible contribution). In the Eh-pH plot to the right, the dashed line similarly traces the projected Eh(pH)-pH line for the O_2-H_2O couple. Small differences between the dashed line and the measured Eh data indicate relatively inactive chemistry. In this case, the differences between measured and expected Eh are indicative of measurement repeatability and drift stability, and of insensitivity to physical disturbance from injection of additional material. The small decline in PO_2 is due to bubbles created by the injection and dilution from injection of O_2-free material.

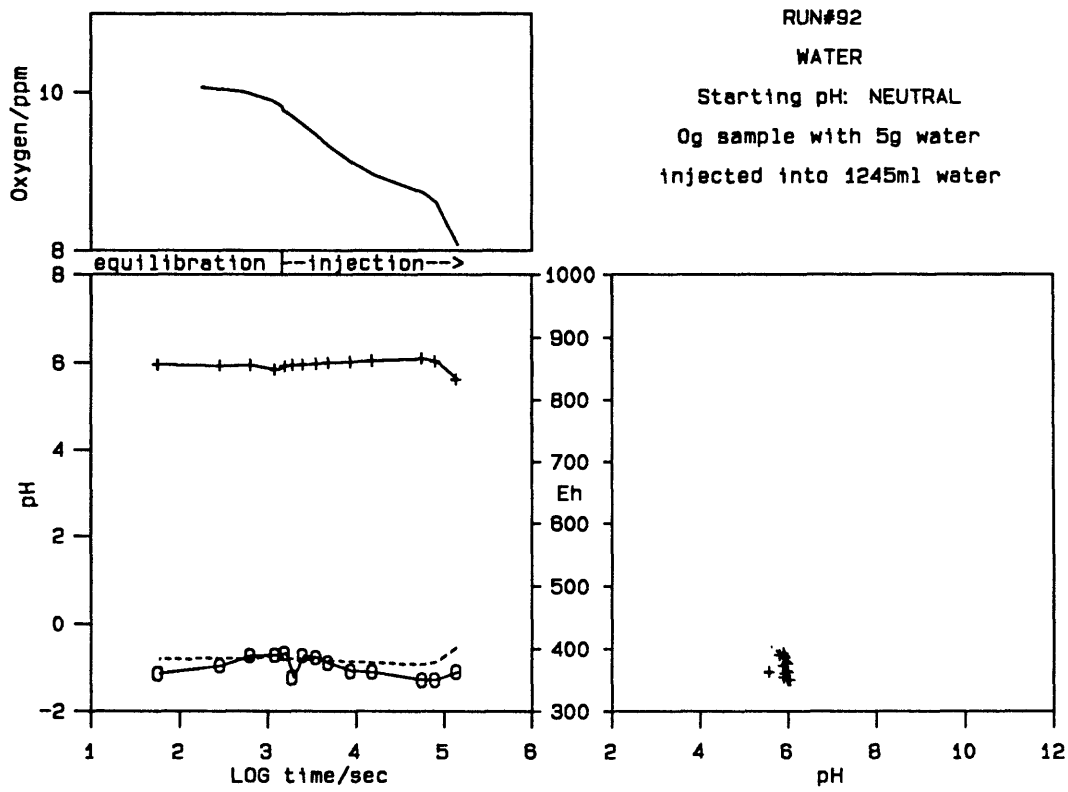

Figure 23 -- This figure demonstrates the stability of the measurement system to physical disturbance by injection of neutral water into water at neutral pH (unbuffered). In the lower left sub-plot, the solid line with pluses is the measured pH data (left scale), the solid line with O's is the measured Eh data (right scale), and the dashed line is the Eh predicted from the equation for the O_2-H_2O couple using the measured pH data (the partial pressure of oxygen has a negligible contribution). In the Eh-pH plot to the right, the dashed line similarly traces the projected Eh(pH)-pH line for the O_2-H_2O couple. Small differences between the dashed line and the measured Eh data indicate relatively inactive chemistry. In this case, the differences between measured and expected Eh are indicative of measurement repeatability and drift stability, and of insensitivity to physical disturbance from injection of additional material. The small decline in PO_2 is due to bubbles created by the injection and dilution from injection of O_2-free material.

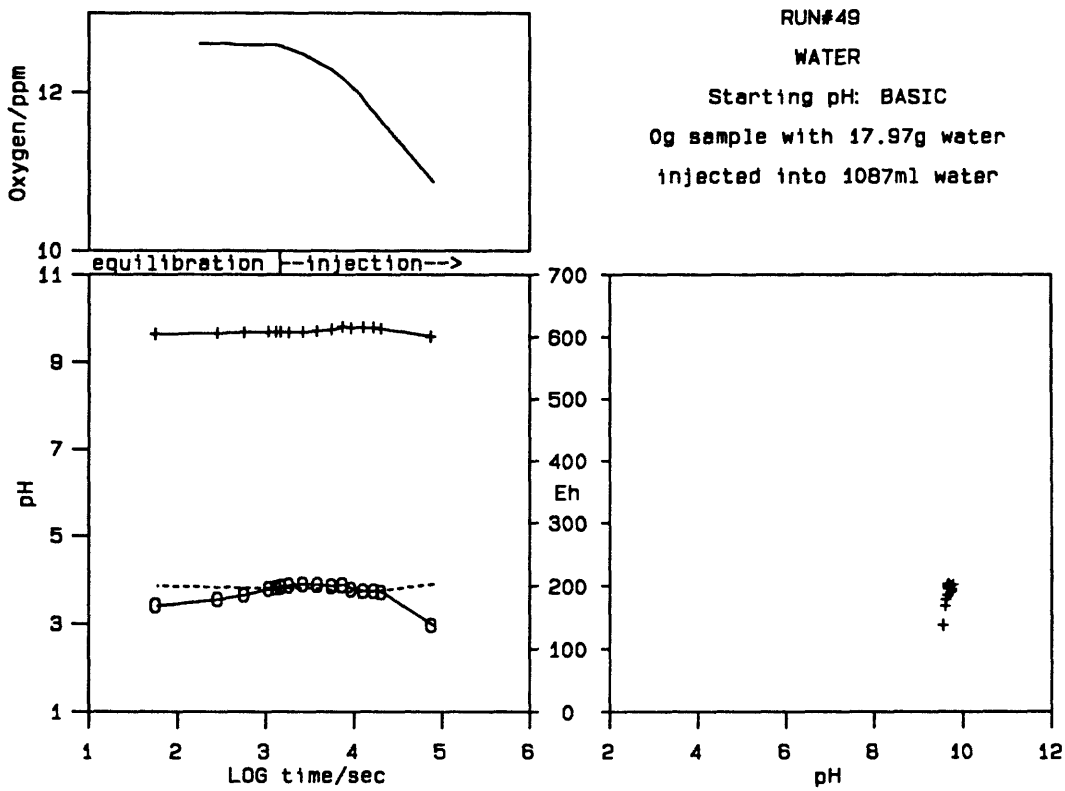

Figure 24 -- This figure demonstrates the stability of the measurement system to physical disturbance by injection of neutral water into basic water at pH 10, buffered by NaOH. In the lower left sub-plot, the solid line with pluses is the measured pH data (left scale), the solid line with O's is the measured Eh data (right scale), and the dashed line is the Eh predicted from the equation for the O_2-H_2O couple using the measured pH data (the partial pressure of oxygen has a negligible contribution). In the Eh-pH plot to the right, the dashed line similarly traces the projected Eh(pH)-pH line for the O_2-H_2O couple. Small differences between the dashed line and the measured Eh data indicate relatively inactive chemistry. In this case, the differences between measured and expected Eh are indicative of measurement repeatability and drift stability, and of insensitivity to physical disturbance from injection of additional material. The small decline in PO_2 is due to bubbles created by the injection and dilution from injection of O_2-free material.

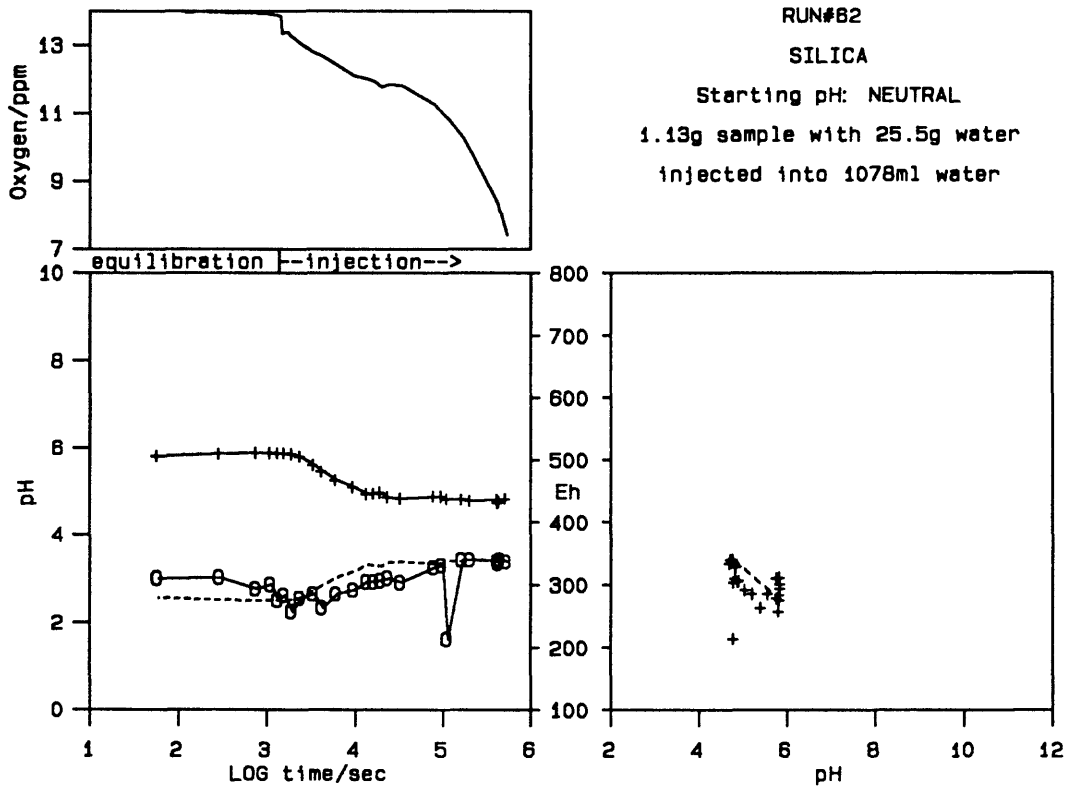

Figure 25 -- This figure demonstrates the injection of a material (fumed silica) that was not expected to chemically react (and substantially did not), into neutral water. In the lower left sub-plot, the solid line with pluses is the measured pH data (left scale), the solid line with O's is the measured Eh data (right scale), and the dashed line is the Eh predicted from the equation for the O_2-H_2O couple using the measured pH data (the partial pressure of oxygen has a negligible contribution). In the Eh-pH plot to the right, the dashed line similarly traces the projected Eh(pH)-pH line for the O_2-H_2O couple. Small differences between the dashed line and the measured Eh data indicate relatively inactive chemistry. The injection of silica produced a decrease in pH to more acid solution. The small decline in PO_2 is due to bubbles created by the injection and dilution from injection of O_2-free material.

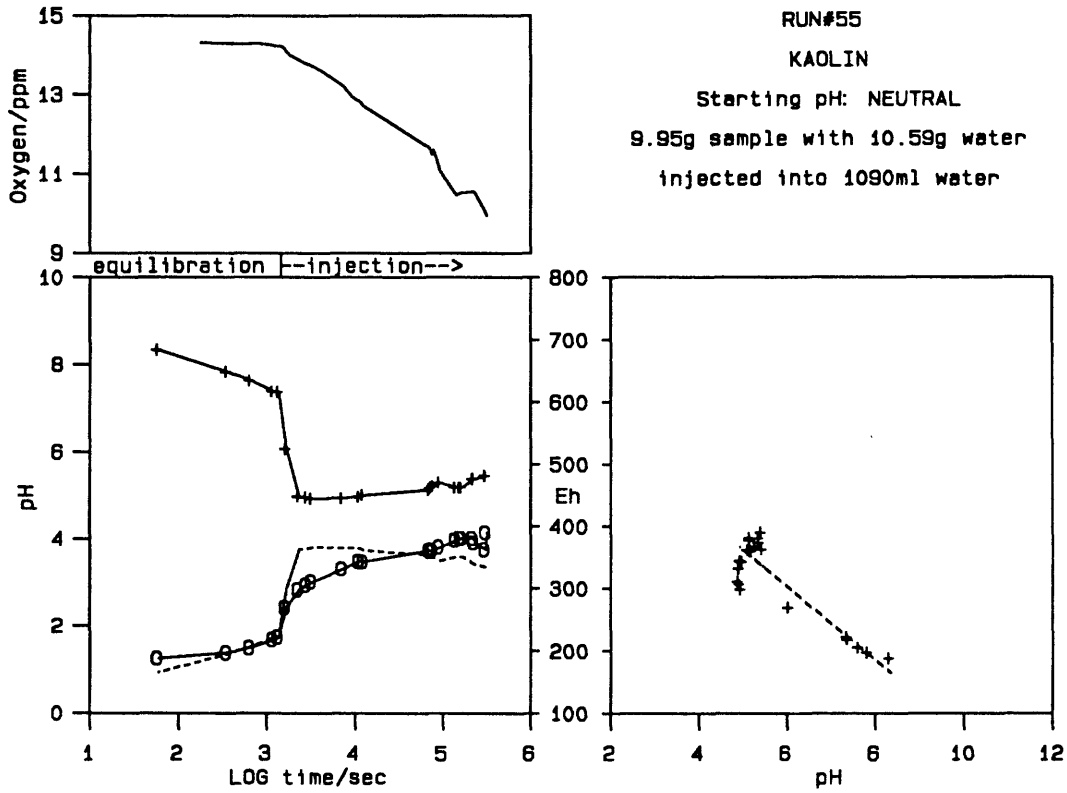

Figure 26 -- This figure shows the reaction from the injection of kaolinite into a neutral solution. Compare with the baselines in Figures 21 through 24 and the relatively inert silica in Figure 25. In the lower left sub-plot, the solid line with pluses is the measured pH data (left scale), the solid line with O's is the measured Eh data (right scale), and the dashed line is the Eh predicted from the equation for the O_2-H_2O couple using the measured pH data (the partial pressure of oxygen has a negligible contribution). In the Eh-pH plot to the right, the dashed line similarly traces the projected Eh(pH)-pH line for the O_2-H_2O couple. Small differences between the dashed line and the measured Eh data indicate relatively inactive chemistry. The small decline in PO_2 is due to bubbles created by the injection and dilution from injection of O_2-free material.

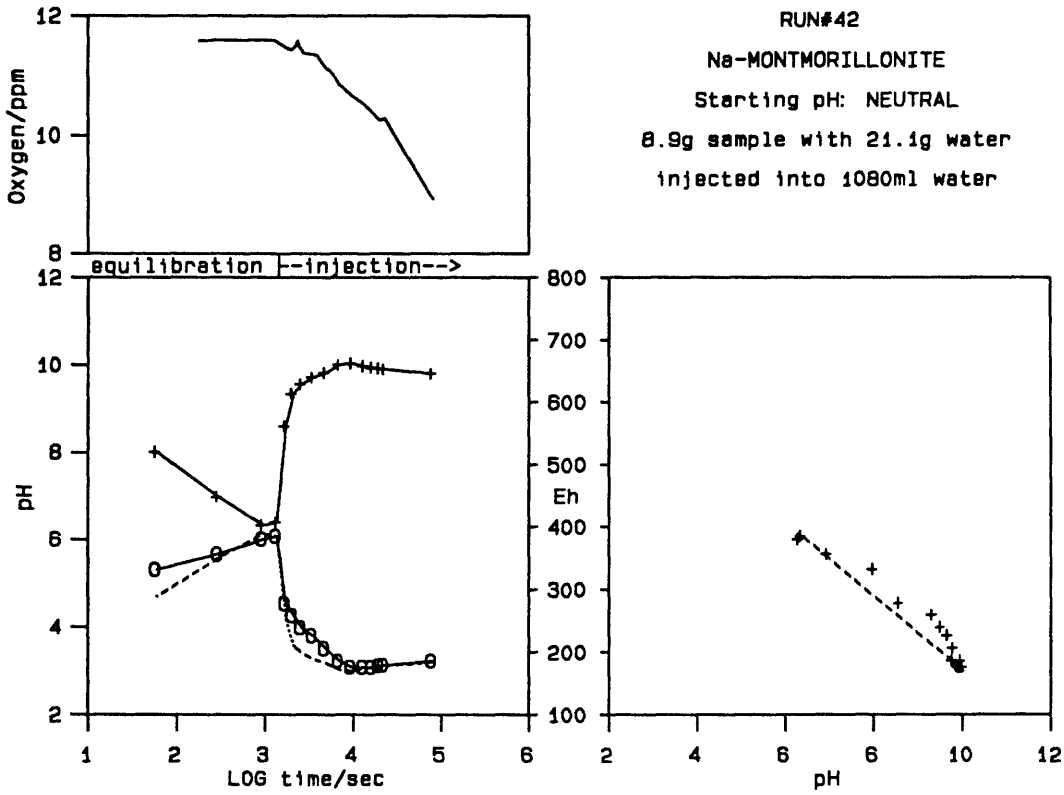

Figure 27 -- This figure shows the reaction from the injection of Na-montmorillonite into a neutral solution. Compare with the baselines in Figures 21 through 24 and the relatively inert silica in Figure 25. In the lower left sub-plot, the solid line with pluses is the measured pH data (left scale), the solid line with O's is the measured Eh data (right scale), and the dashed line is the Eh predicted from the equation for the O_2-H_2O couple using the measured pH data (the partial pressure of oxygen has a negligible contribution). In the Eh-pH plot to the right, the dashed line similarly traces the projected Eh(pH)-pH line for the O_2-H_2O couple. Small differences between the dashed line and the measured Eh data indicate relatively inactive chemistry. Note that the direction of change for both pH and Eh with Na-montmorillonite injection is opposite to that observed in the previous to figures for silica and kaolinite, and the changes are greater in magnitude. The small decline in PO_2 is due to bubbles created by the injection and dilution from injection of O_2-free material.

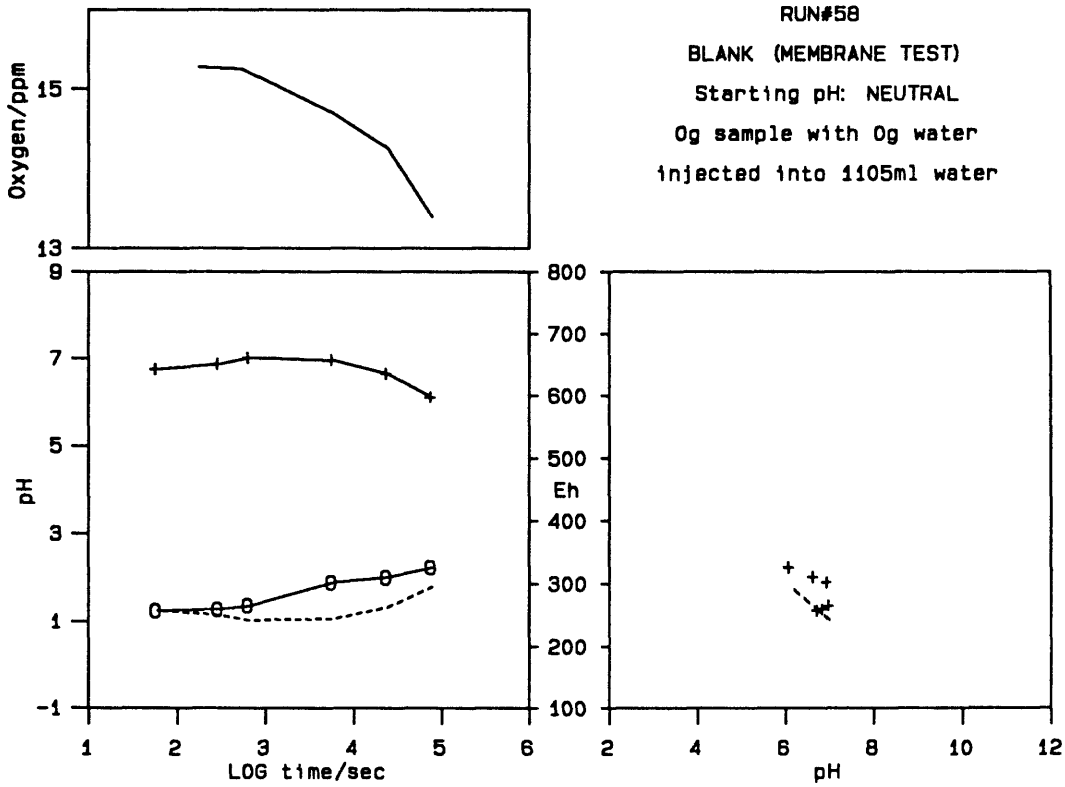

Figure 28 -- The presence of clay minerals sometimes bias pH and Eh electrode measurements. This figure tests the response of the electrodes to being isolated by dialysis membrane (compare with Figure 21). In the lower left sub-plot, the solid line with pluses is the measured pH data (left scale), the solid line with O's is the measured Eh data (right scale), and the dashed line is the Eh predicted from the equation for the O_2-H_2O couple using the measured pH data (the partial pressure of oxygen has a negligible contribution). In the Eh-pH plot to the right, the dashed line similarly traces the projected Eh(pH)-pH line for the O_2-H_2O couple. Small differences between the dashed line and the measured Eh data indicate relatively inactive chemistry. In this case, the differences between measured and expected Eh are indicative of measurement repeatability and drift stability with membrane-covered pH and Eh electrodes. The small decline in PO_2 is due to bubbles created by the injection and dilution from injection of O_2-free material.

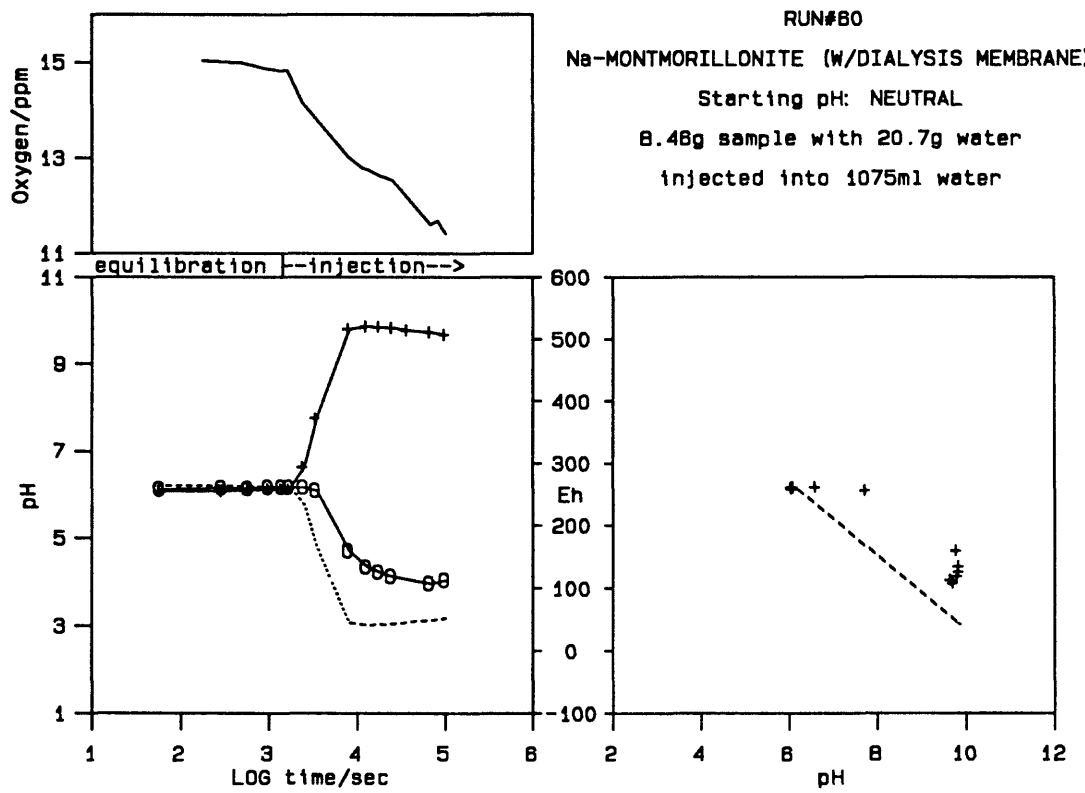

Figure 29 -- This figure tests the effect of clay minerals on the Eh-pH electrodes by isolating them with dialysis membrane. Compared with Figure 27, the clays do not appear to substantially effect the Eh-pH electrodes; the largest effect is the delay in response caused by diffusion through the dialysis membrane. In the lower left sub-plot, the solid line with pluses is the measured pH data (left scale), the solid line with O's is the measured Eh data (right scale), and the dashed line is the Eh predicted from the equation for the O_2-H_2O couple using the measured pH data (the partial pressure of oxygen has a negligible contribution). In the Eh-pH plot to the right, the dashed line similarly traces the projected Eh(pH)-pH line for the O_2-H_2O couple. The small decline in PO_2 is due to bubbles created by the injection and dilution from injection of O_2-free material.

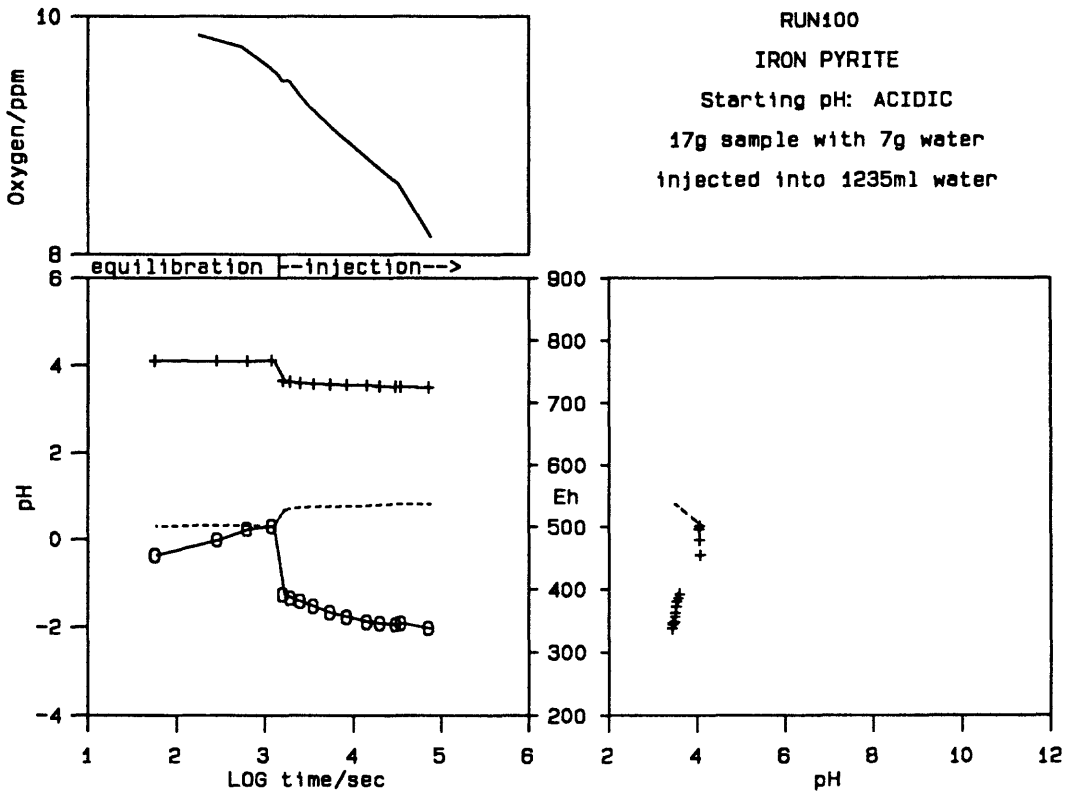

Figure 30 -- The injection of pyrite into acidic solution. In the lower left sub-plot, the solid line with pluses is the measured pH data (left scale), the solid line with O's is the measured Eh data (right scale), and the dashed line is the Eh predicted from the equation for the O_2-H_2O couple using the measured pH data (the partial pressure of oxygen has a negligible contribution). In the Eh-pH plot to the right, the dashed line similarly traces the projected Eh(pH)-pH line for the O_2-H_2O couple. Note the oxidation of pyrite indicated by the large decrease of the measured Eh compared to the expected Eh. The small decline in PO_2 is due to bubbles created by the injection and dilution from injection of O_2-free material. This situation exhibited the least drop of PO_2 when pyrite was the sample.

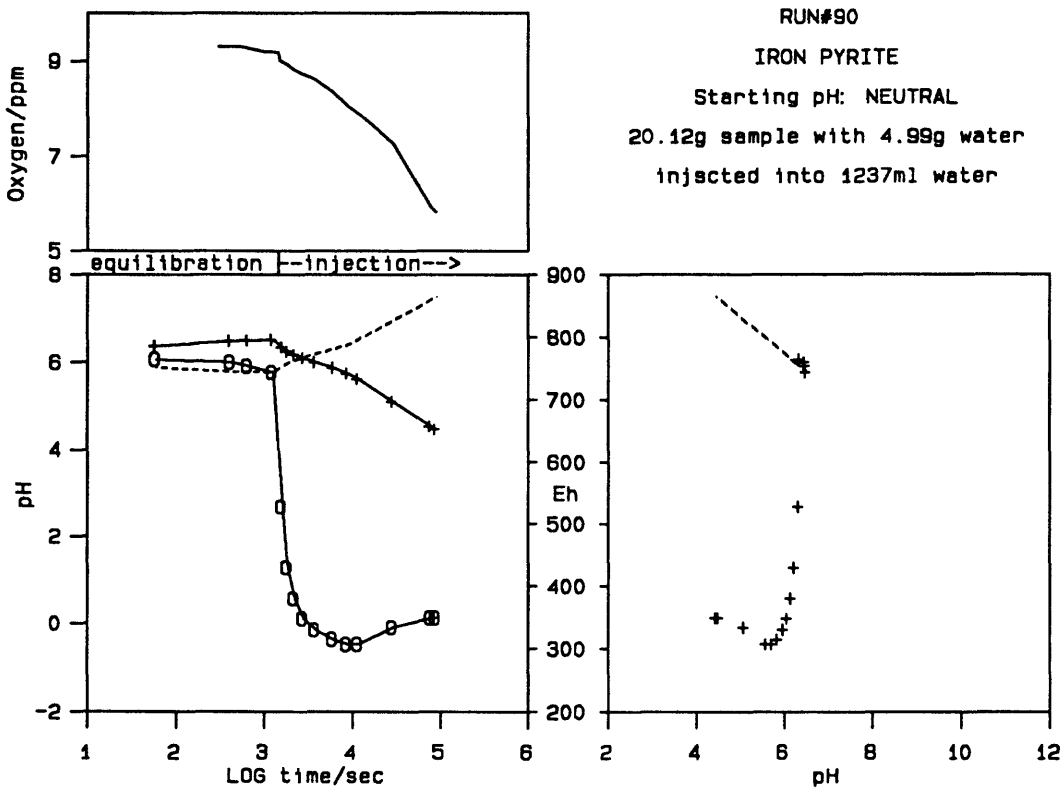

Figure 31 -- The injection of pyrite into neutral solution. In the lower left sub-plot, the solid line with pluses is the measured pH data (left scale), the solid line with O's is the measured Eh data (right scale), and the dashed line is the Eh predicted from the equation for the O_2-H_2O couple using the measured pH data (the partial pressure of oxygen has a negligible contribution). In the Eh-pH plot to the right, the dashed line similarly traces the projected Eh(pH)-pH line for the O_2-H_2O couple. Note the oxidation of pyrite indicated by the decrease of PO_2, and the large decrease of the measured compared to the expected Eh.

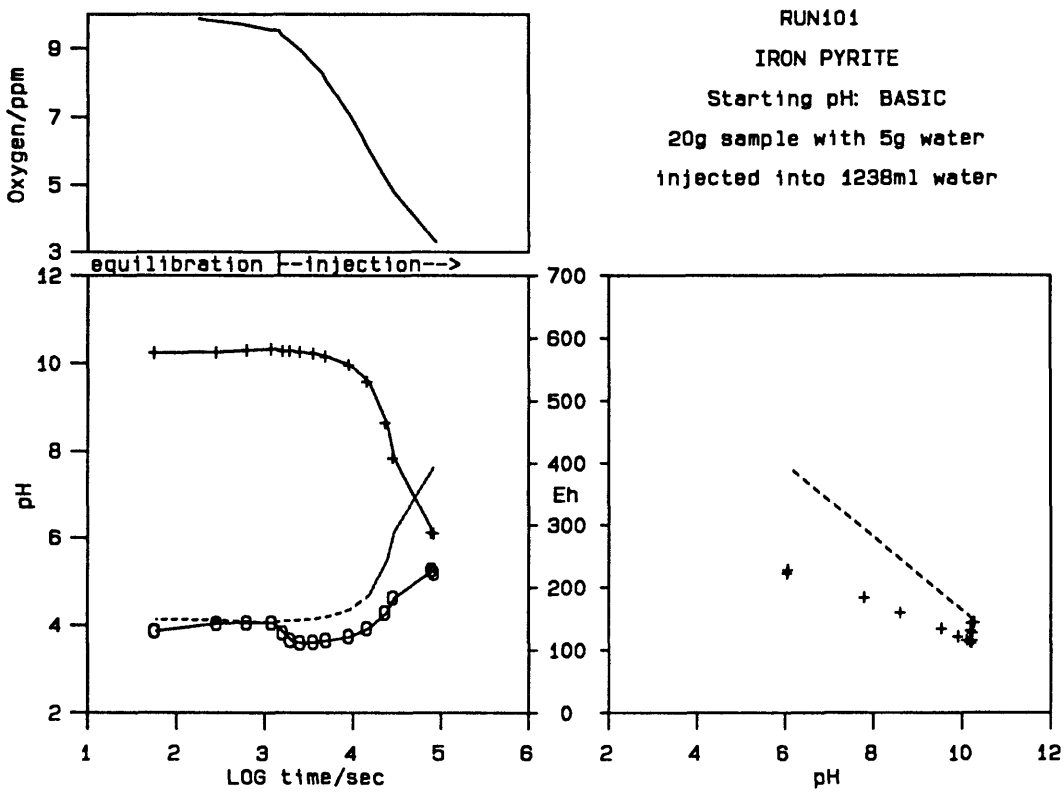

Figure 32 -- The injection of pyrite into basic solution. In the lower left sub-plot, the solid line with pluses is the measured pH data (left scale), the solid line with O's is the measured Eh data (right scale), and the dashed line is the Eh predicted from the equation for the O_2-H_2O couple using the measured pH data (the partial pressure of oxygen has a negligible contribution). In the Eh-pH plot to the right, the dashed line similarly traces the projected Eh(pH)-pH line for the O_2-H_2O couple. Note that a mild oxidation reaction is indicated by the difference between observed and calculated Eh. However, PO_2 loss is great.

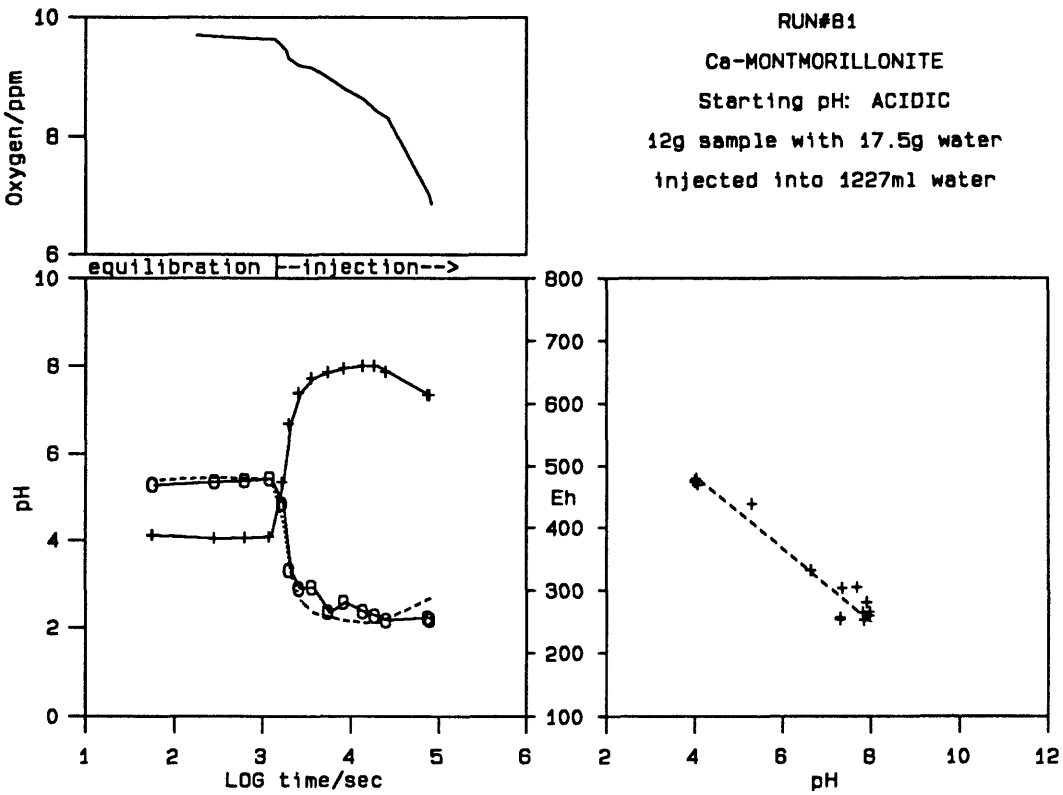

Figure 33 -- The injection of Ca-montmorillonite into acidic solution. In the lower left sub-plot, the solid line with pluses is the measured pH data (left scale), the solid line with O's is the measured Eh data (right scale), and the dashed line is the Eh predicted from the equation for the O_2-H_2O couple using the measured pH data (the partial pressure of oxygen has a negligible contribution). In the Eh-pH plot to the right, the dashed line similarly traces the projected Eh(pH)-pH line for the O_2-H_2O couple. Small differences between the dashed line and the measured Eh data indicate relatively inactive chemistry. The small decline in PO_2 is due to bubbles created by the injection and dilution from injection of O_2-free material.

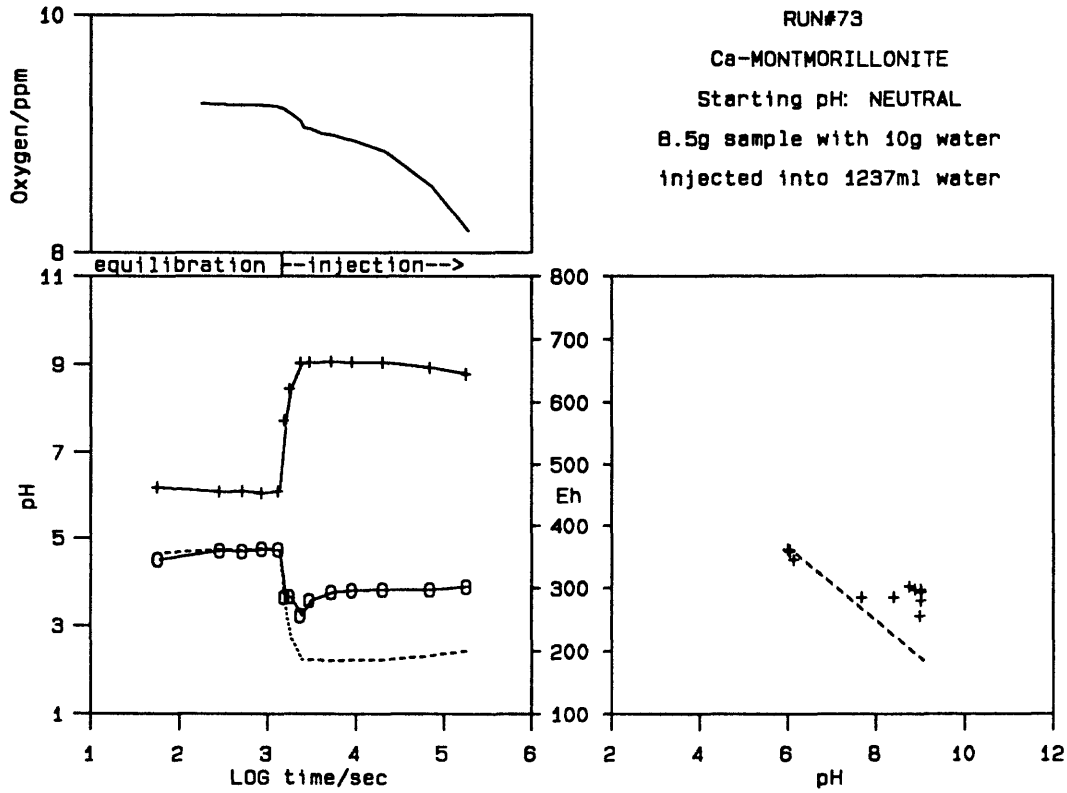

Figure 34 -- The injection of Ca-montmorillonite into neutral solution. In the lower left sub-plot, the solid line with pluses is the measured pH data (left scale), the solid line with O's is the measured Eh data (right scale), and the dashed line is the Eh predicted from the equation for the O_2-H_2O couple using the measured pH data (the partial pressure of oxygen has a negligible contribution). In the Eh-pH plot to the right, the dashed line similarly traces the projected Eh(pH)-pH line for the O_2-H_2O couple. Note the indication of a reduction process, as the expected Eh is lower than observed (compare the pyrite oxidation in Figure 30). This may also result from the injected clay bringing more oxygen into solution. The small decline in PO_2 is due to bubbles created by the injection and dilution from injection of O_2-free material.

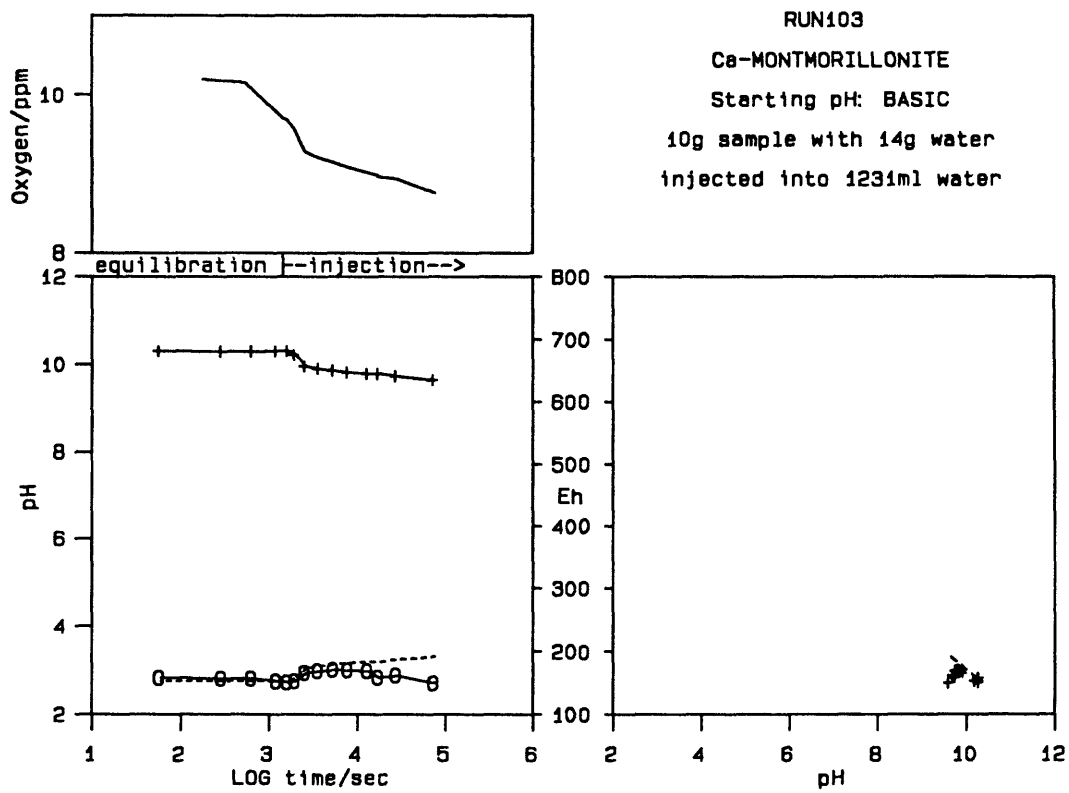

Figure 35 -- The injection of Ca-montmorillonite into basic solution. In the lower left sub-plot, the solid line with pluses is the measured pH data (left scale), the solid line with O's is the measured Eh data (right scale), and the dashed line is the Eh predicted from the equation for the O_2-H_2O couple using the measured pH data (the partial pressure of oxygen has a negligible contribution). In the Eh-pH plot to the right, the dashed line similarly traces the projected Eh(pH)-pH line for the O_2-H_2O couple. Small differences between the dashed line and the measured Eh data indicate relatively inactive chemistry. The small decline in PO_2 is due to bubbles created by the injection and dilution from injection of O_2-free material.

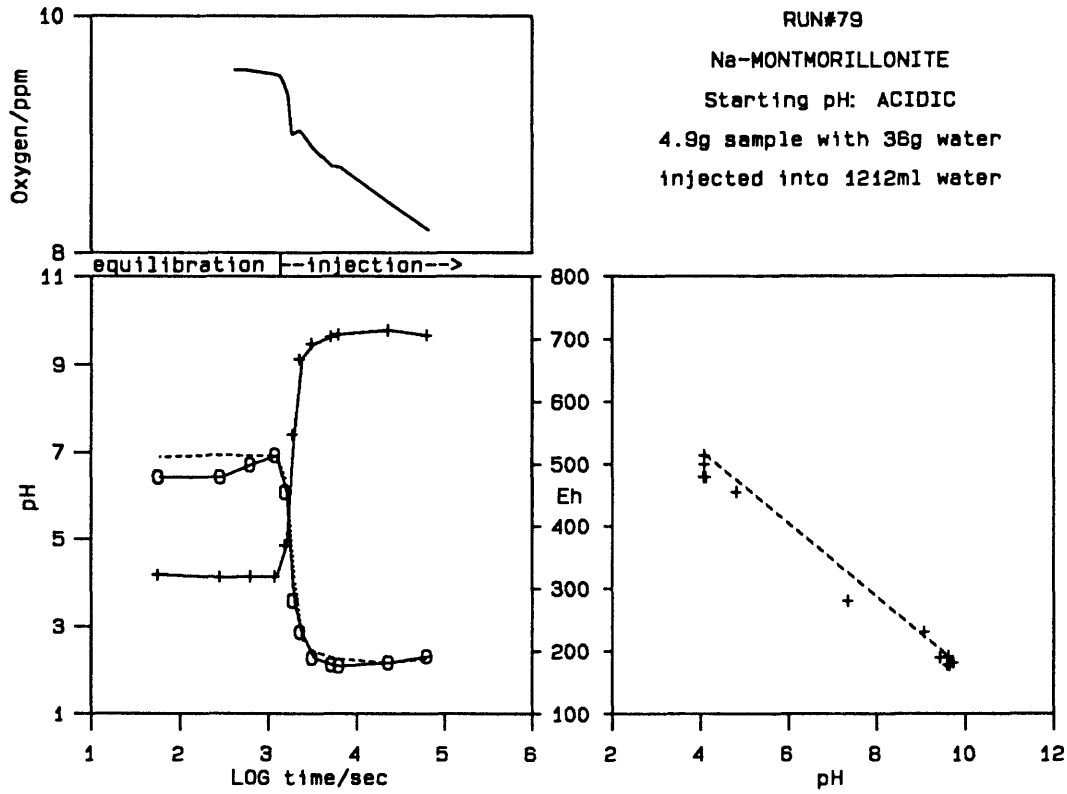

Figure 36 -- The injection of Na-montmorillonite into acidic solution. In the lower left sub-plot, the solid line with pluses is the measured pH data (left scale), the solid line with O's is the measured Eh data (right scale), and the dashed line is the Eh predicted from the equation for the O_2-H_2O couple using the measured pH data (the partial pressure of oxygen has a negligible contribution). In the Eh-pH plot to the right, the dashed line similarly traces the projected Eh(pH)-pH line for the O_2-H_2O couple. Small differences between the dashed line and the measured Eh data indicate relatively inactive chemistry. The small decline in PO_2 is due to bubbles created by the injection and dilution from injection of O_2-free material.

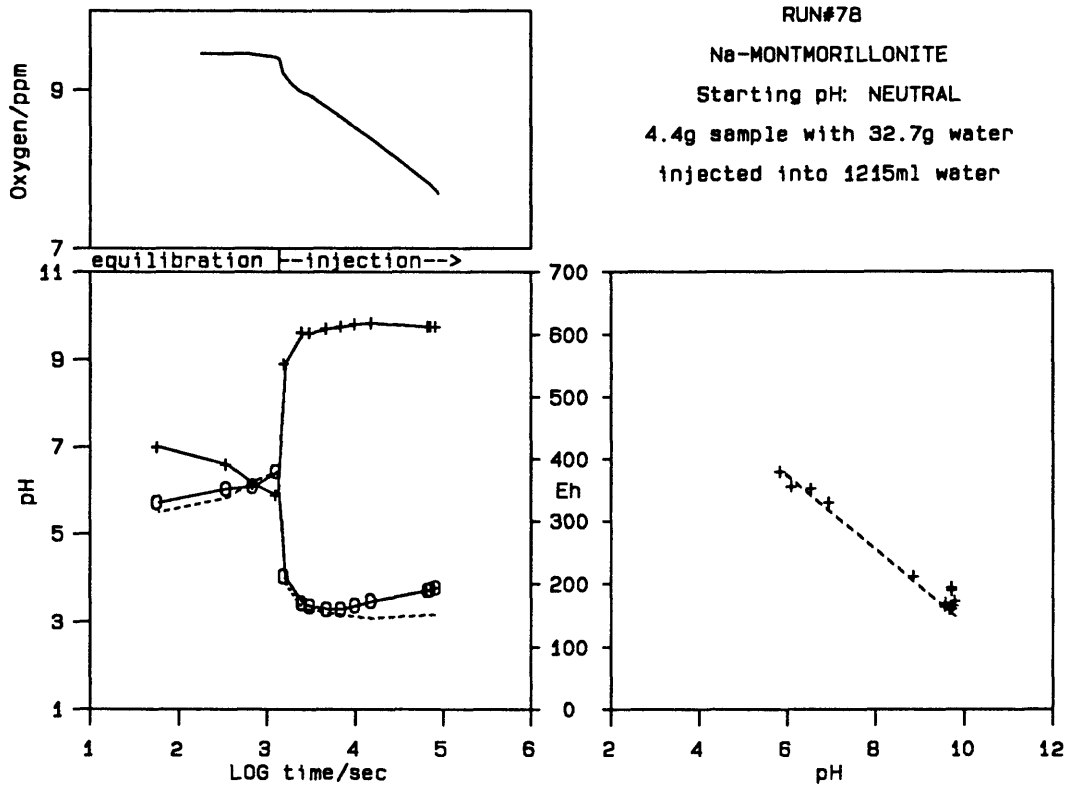

Figure 37 -- The injection of Na-montmorillonite into neutral solution. In the lower left sub-plot, the solid line with pluses is the measured pH data (left scale), the solid line with O's is the measured Eh data (right scale), and the dashed line is the Eh predicted from the equation for the O_2-H_2O couple using the measured pH data (the partial pressure of oxygen has a negligible contribution). In the Eh-pH plot to the right, the dashed line similarly traces the projected Eh(pH)-pH line for the O_2-H_2O couple. Small differences between the dashed line and the measured Eh data indicate relatively inactive chemistry. The small decline in PO_2 is due to bubbles created by the injection and dilution from injection of O_2-free material.

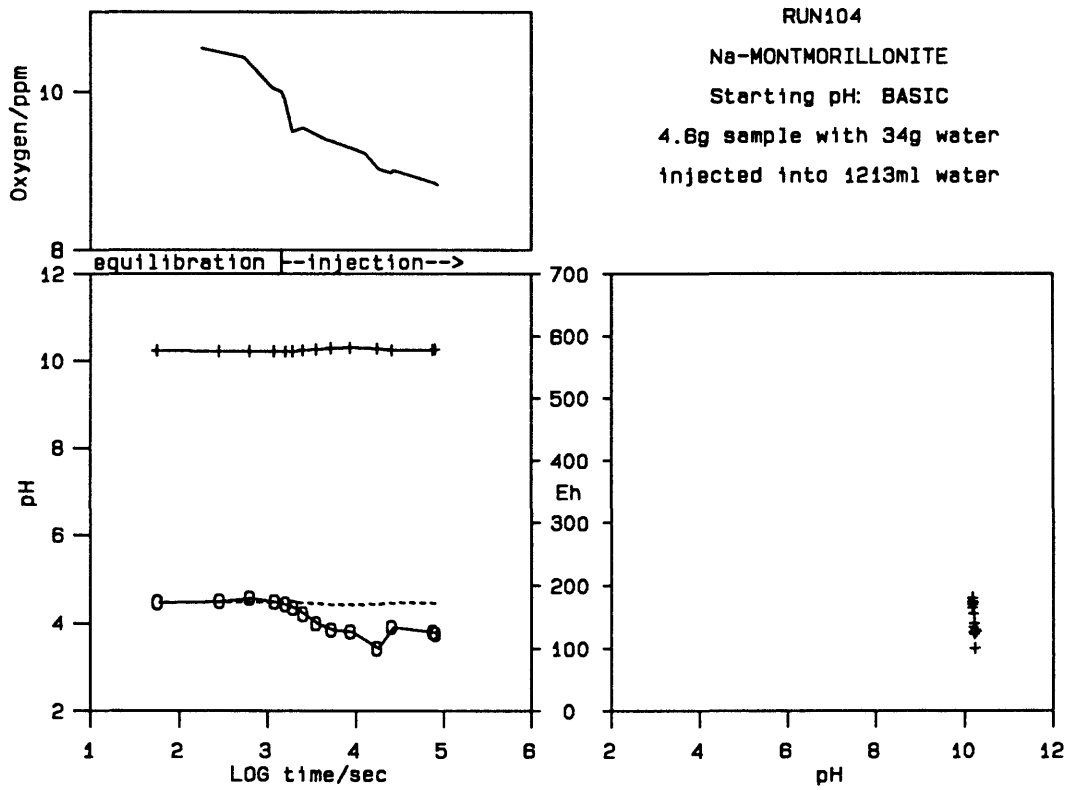

Figure 38 -- The injection of Na-montmorillonite into basic solution. In the lower left sub-plot, the solid line with pluses is the measured pH data (left scale), the solid line with O's is the measured Eh data (right scale), and the dashed line is the Eh predicted from the equation for the O_2-H_2O couple using the measured pH data (the partial pressure of oxygen has a negligible contribution). In the Eh-pH plot to the right, the dashed line similarly traces the projected Eh(pH)-pH line for the O_2-H_2O couple. Small differences between the dashed line and the measured Eh data indicate relatively inactive chemistry. The small decline in PO_2 is due to bubbles created by the injection and dilution from injection of O_2-free material.

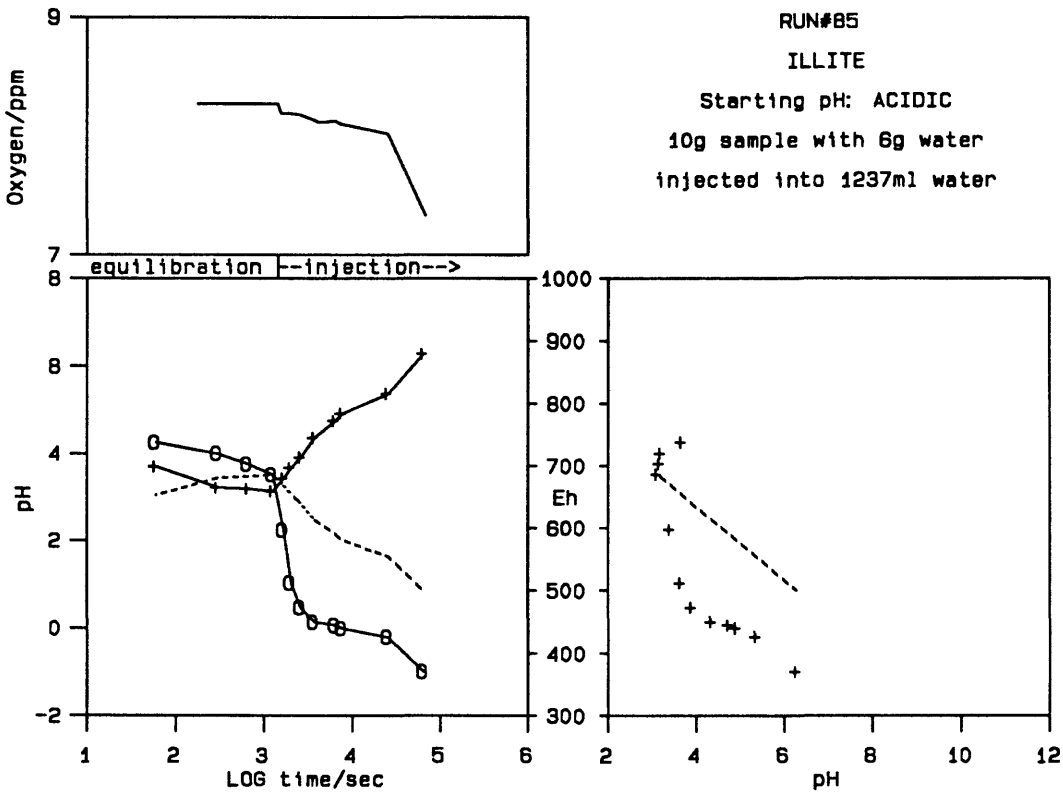

Figure 39 -- The injection of illite into acidic solution. In the lower left sub-plot, the solid line with pluses is the measured pH data (left scale), the solid line with O's is the measured Eh data (right scale), and the dashed line is the Eh predicted from the equation for the O_2-H_2O couple using the measured pH data (the partial pressure of oxygen has a negligible contribution). In the Eh-pH plot to the right, the dashed line similarly traces the projected Eh(pH)-pH line for the O_2-H_2O couple. Note the indication of an active oxidation process (the measured Eh is below the expected), assumed to be oxidation of structural iron in the clay mineral.

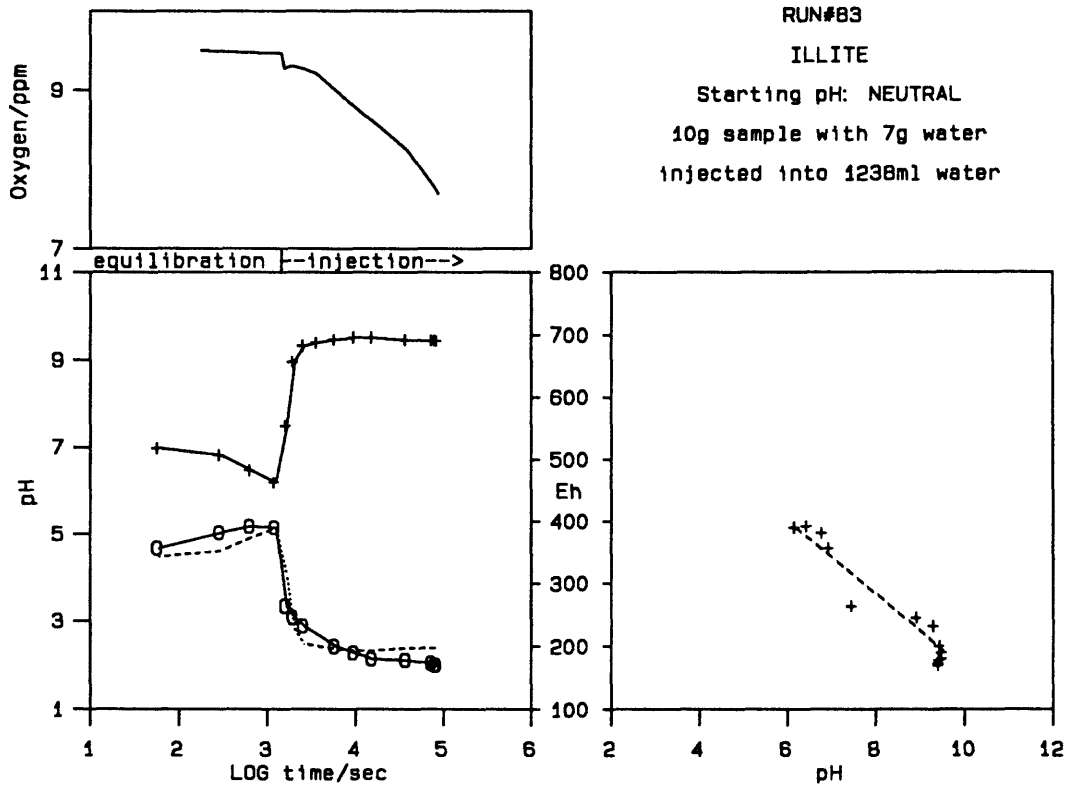

Figure 40 -- The injection of illite into neutral solution. In the lower left sub-plot, the solid line with pluses is the measured pH data (left scale), the solid line with O's is the measured Eh data (right scale), and the dashed line is the Eh predicted from the equation for the O_2-H_2O couple using the measured pH data (the partial pressure of oxygen has a negligible contribution). In the Eh-pH plot to the right, the dashed line similarly traces the projected Eh(pH)-pH line for the O_2-H_2O couple. Small differences between the dashed line and the measured Eh data indicate relatively inactive chemistry. The small decline in PO_2 is due to bubbles created by the injection and dilution from injection of O_2-free material.

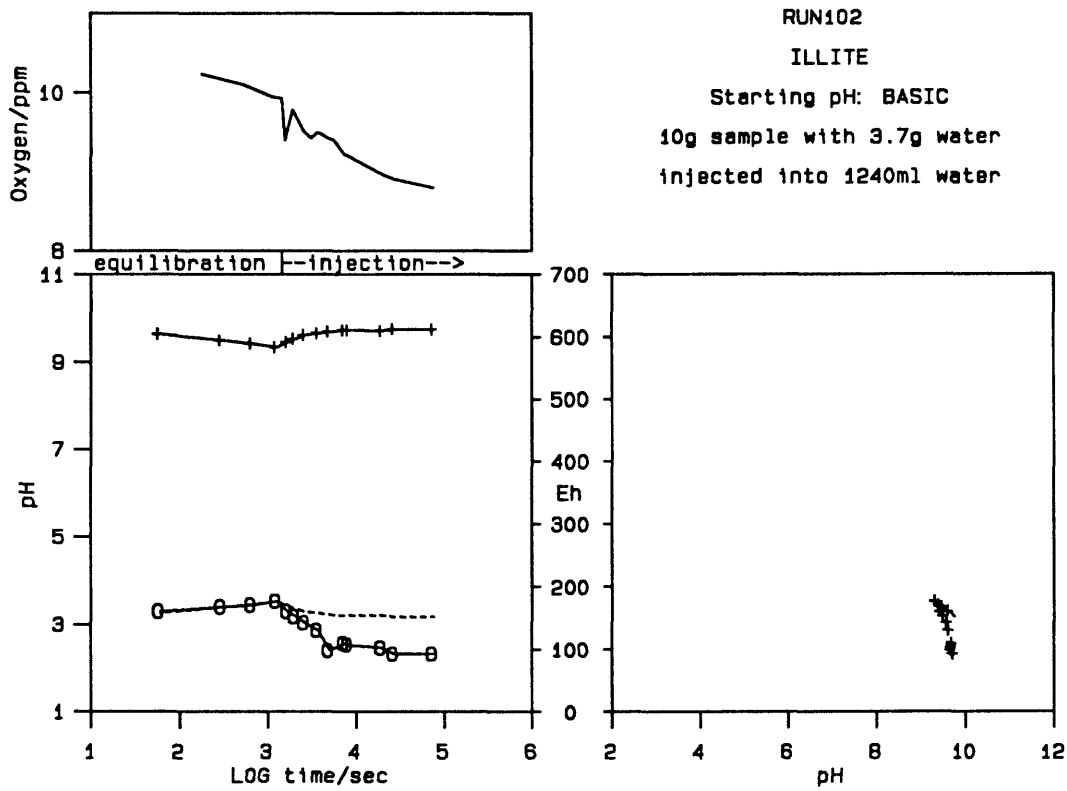

Figure 41 -- The injection of illite into basic solution. In the lower left sub-plot, the solid line with pluses is the measured pH data (left scale), the solid line with O's is the measured Eh data (right scale), and the dashed line is the Eh predicted from the equation for the O_2-H_2O couple using the measured pH data (the partial pressure of oxygen has a negligible contribution). In the Eh-pH plot to the right, the dashed line similarly traces the projected Eh(pH)-pH line for the O_2-H_2O couple. A mild oxidation reaction is indicated.

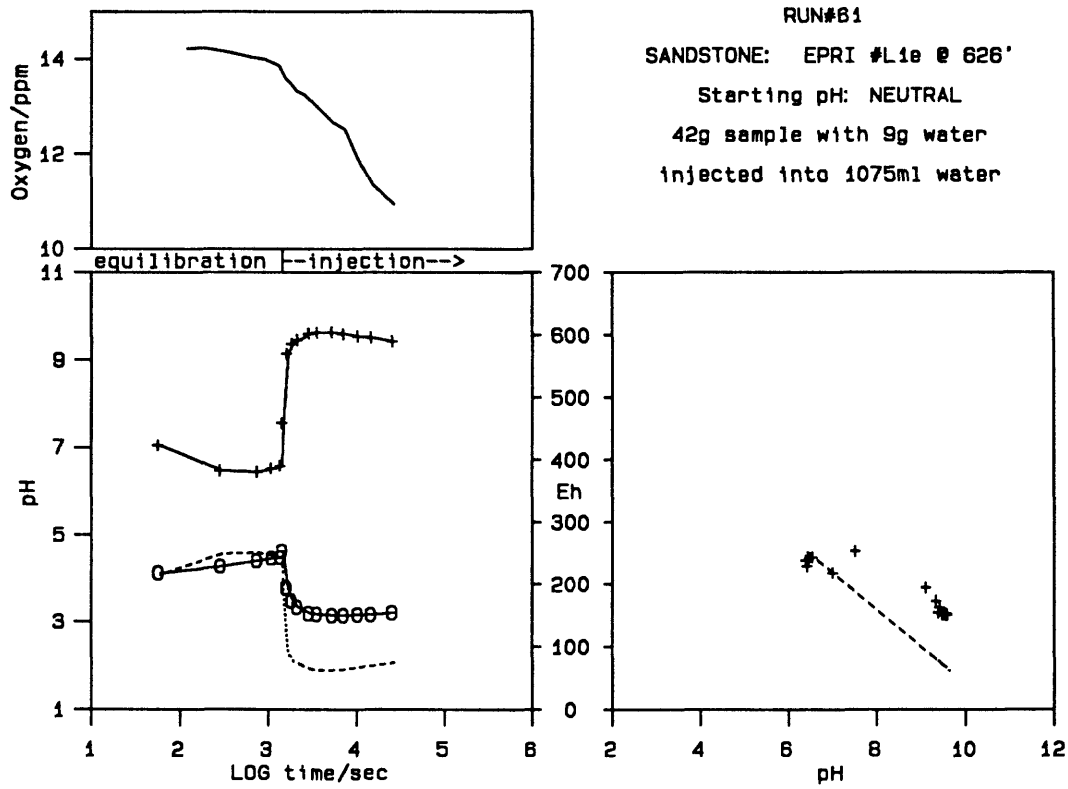

Figure 42 -- Sample of core from EPRI well L-1 at depth 626' sandstone (exposed to air) injected into neutral solution. Note the similarity with the Ca-montmorillonite in neutral solution (Figure 34), which was being reduced. In the lower left sub-plot, the solid line with pluses is the measured pH data (left scale), the solid line with O's is the measured Eh data (right scale), and the dashed line is the Eh predicted from the equation for the O_2-H_2O couple using the measured pH data (the partial pressure of oxygen has a negligible contribution). In the Eh-pH plot to the right, the dashed line similarly traces the projected Eh(pH)-pH line for the O_2-H_2O couple. Note the indication of reduction (or entrance of extra oxygen) in the Eh curves, though the PO_2 plot (Figure 62) indicates a net loss of oxygen.

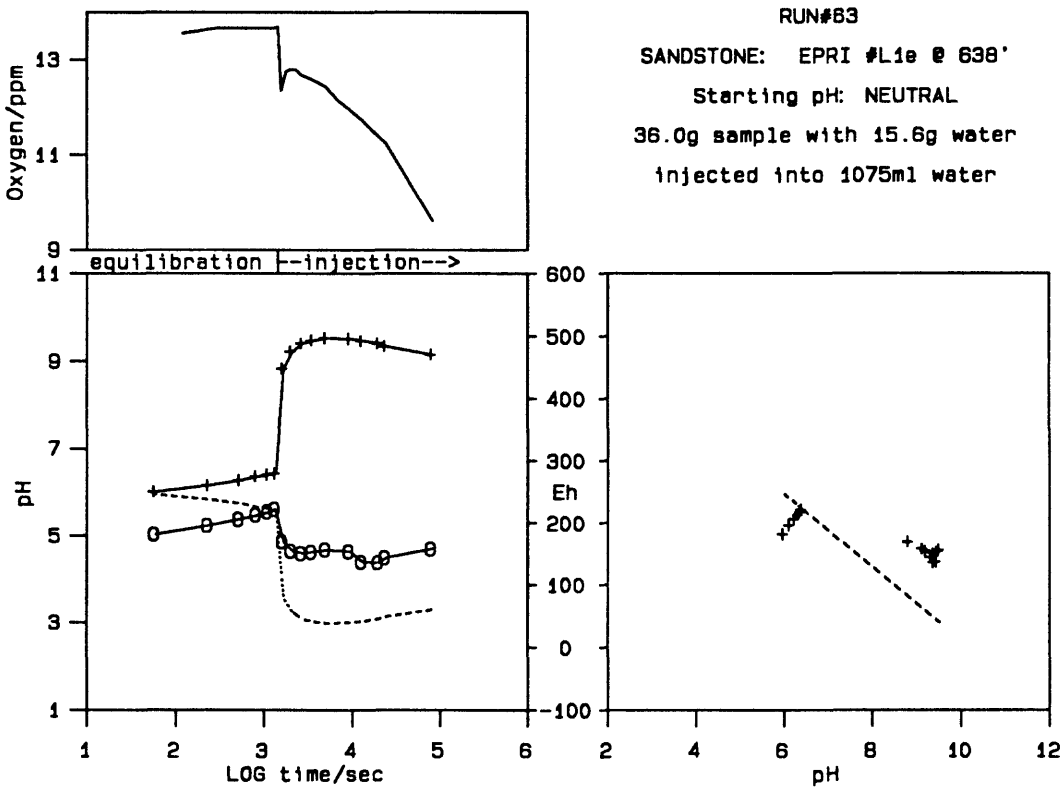

Figure 43 -- Sample of core from EPRI well L-1 at depth 638' sandstone (exposed to air) injected into neutral solution. Note the similarity with the Ca-montmorillonite in neutral solution (Figure 34), which was being reduced. In the lower left sub-plot, the solid line with pluses is the measured pH data (left scale), the solid line with O's is the measured Eh data (right scale), and the dashed line is the Eh predicted from the equation for the O_2-H_2O couple using the measured pH data (the partial pressure of oxygen has a negligible contribution). In the Eh-pH plot to the right, the dashed line similarly traces the projected Eh(pH)-pH line for the O_2-H_2O couple. Note the indication of reduction (or entrance of extra oxygen) by the Eh curves, enven though the PO_2 plot (Figure 63) indicates a net loss of oxygen.

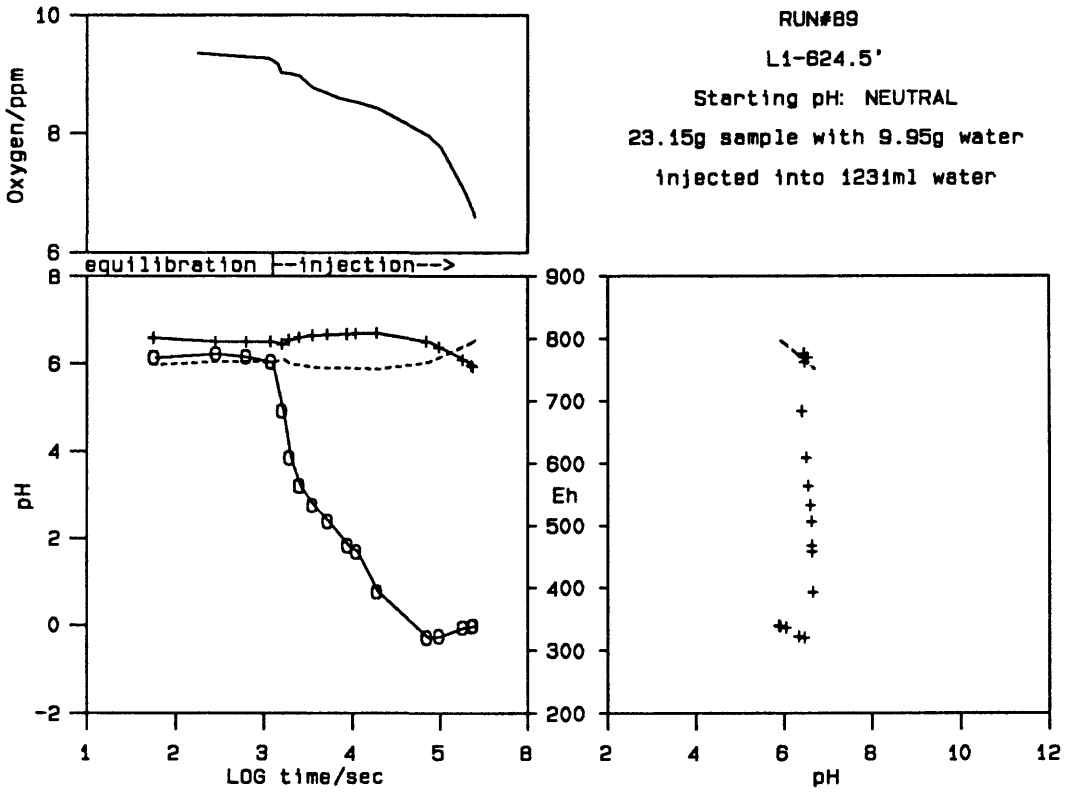

Figure 44 -- Sample of core from EPRI well L-1 at depth 624.5' (acquired without exposure to air) injected into neutral solution. Note the similarity with the pyrite in neutral solution (Figure 31) and the illite into acid solution (Figure 39), both of which were being oxidized. In the lower left sub-plot, the solid line with pluses is the measured pH data (left scale), the solid line with O's is the measured Eh data (right scale), and the dashed line is the Eh predicted from the equation for the O_2-H_2O couple using the measured pH data (the partial pressure of oxygen has a negligible contribution). In the Eh-pH plot to the right, the dashed line similarly traces the projected Eh(pH)-pH line for the O_2-H_2O couple. This sample has a major indication of oxidation (possibly of both pyrite and illite) in the Eh curves, yet the PO_2 plot (Figure 64) indicates no net loss of oxygen from solution. The infrared spectrum also indicates the presence of illite (see Figure 20).

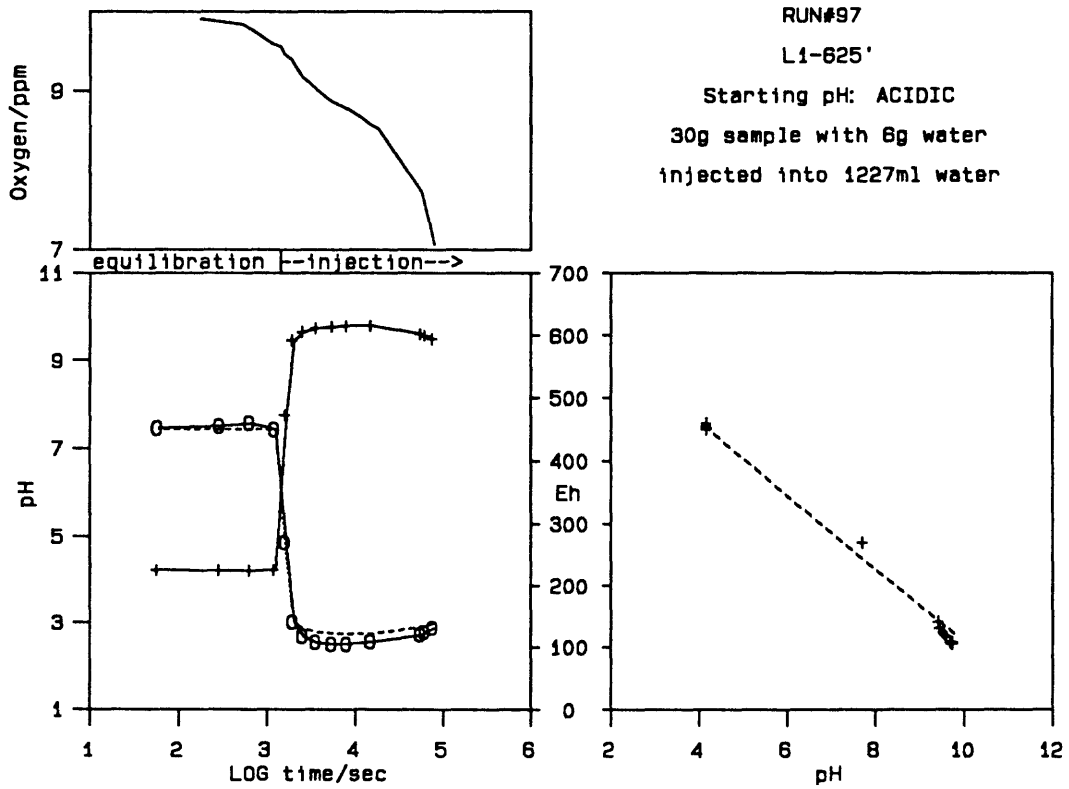

Figure 45 -- Sample of core from EPRI well L-1 at depth 625' (acquired without exposure to air) injected into acid solution. Note the similarity with the Ca- and Na-montmorillonites in acid solution (Figures 33 and 36). In the lower left sub-plot, the solid line with pluses is the measured pH data (left scale), the solid line with O's is the measured Eh data (right scale), and the dashed line is the Eh predicted from the equation for the O_2-H_2O couple using the measured pH data (the partial pressure of oxygen has a negligible contribution). In the Eh-pH plot to the right, the dashed line similarly traces the projected Eh(pH)-pH line for the O_2-H_2O couple. Note there is a slight indication of oxidation.

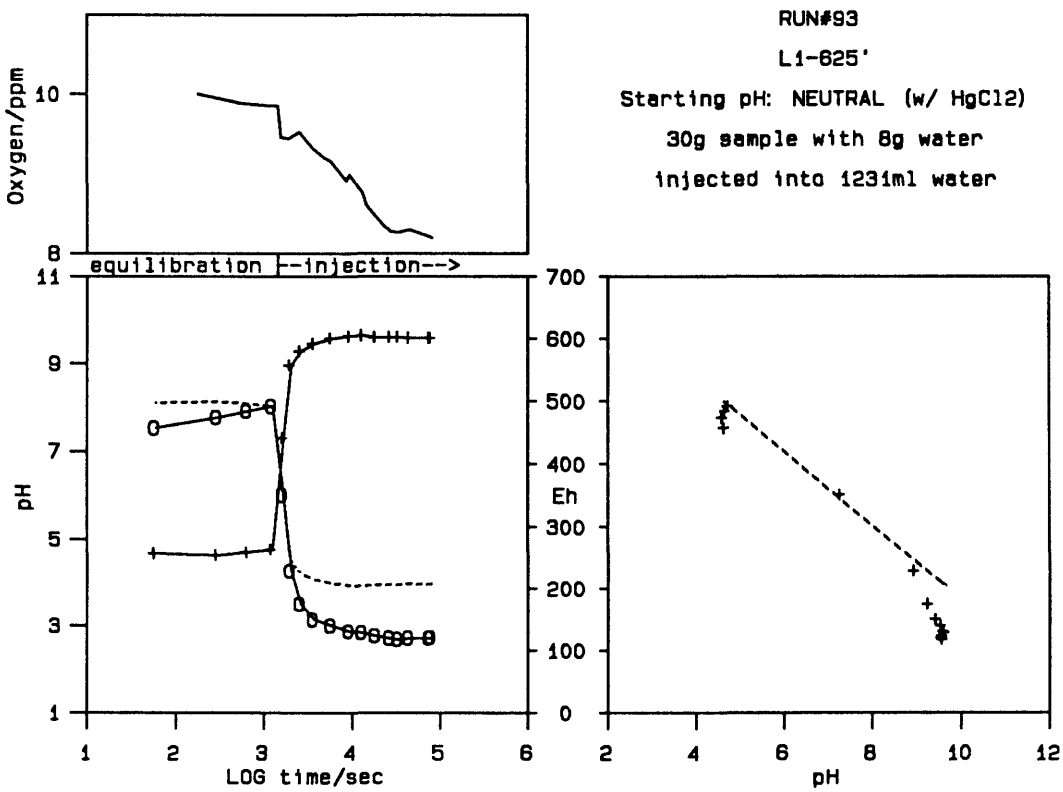

Figure 46 -- Sample of core from EPRI well L-1 at depth 625' (without exposure to air) injected into neutral solution with mercuric chloride sterilization. Note the similarity with the illite in acidic solution (Figure 39), which was being oxidized. In the lower left sub-plot, the solid line with pluses is the measured pH data (left scale), the solid line with O's is the measured Eh data (right scale), and the dashed line is the Eh predicted from the equation for the O_2-H_2O couple using the measured pH data (the partial pressure of oxygen has a negligible contribution). In the Eh-pH plot to the right, the dashed line similarly traces the projected Eh(pH)-pH line for the O_2-H_2O couple. Note the indication of oxidation.

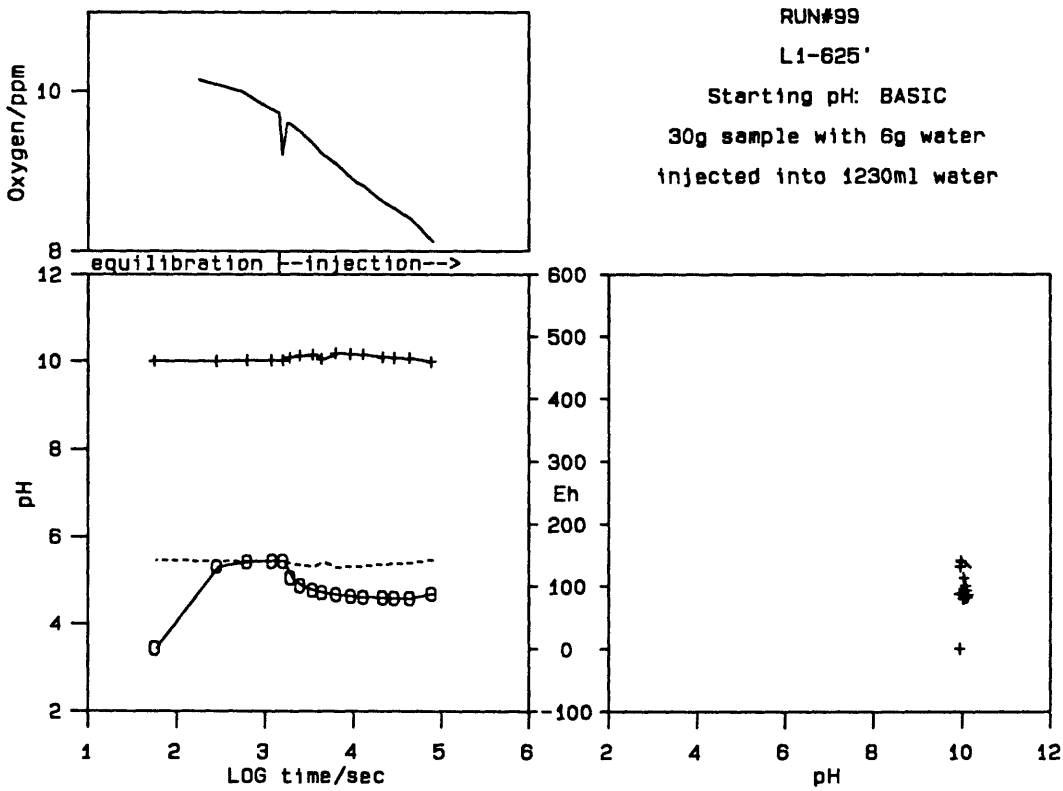

Figure 47 -- Sample of core from EPRI well L-1 at depth 625' (without exposure to air) injected into basic solution. Note the similarity with the Illite in basic solution (Figure 41), which was being oxidized. In the lower left sub-plot, the solid line with pluses is the measured pH data (left scale), the solid line with O's is the measured Eh data (right scale), and the dashed line is the Eh predicted from the equation for the O_2-H_2O couple using the measured pH data (the partial pressure of oxygen has a negligible contribution). In the Eh-pH plot to the right, the dashed line similarly traces the projected Eh(pH)-pH line for the O_2-H_2O couple. Note the slight indication of oxidation.

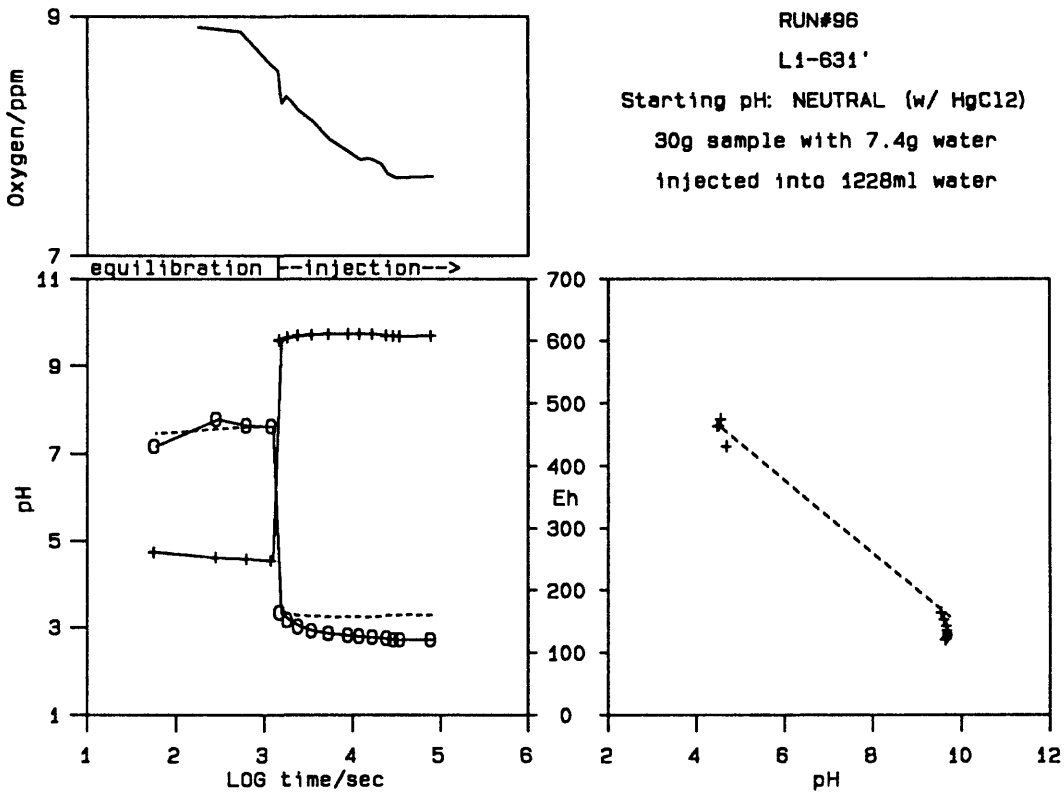

Figure 48 -- Sample of core from EPRI well L-1 at depth 631' (without exposure to air) injected into neutral solution with mercuric chloride sterilization. Note the similarity with the Na-montmorillonite in acid solution (Figure 36), though this sample exhibits more oxidation. In the lower left sub-plot, the solid line with pluses is the measured pH data (left scale), the solid line with O's is the measured Eh data (right scale), and the dashed line is the Eh predicted from the equation for the O_2-H_2O couple using the measured pH data (the partial pressure of oxygen has a negligible contribution). In the Eh-pH plot to the right, the dashed line similarly traces the projected Eh(pH)-pH line for the O_2-H_2O couple. Note the slight indication of oxidation.

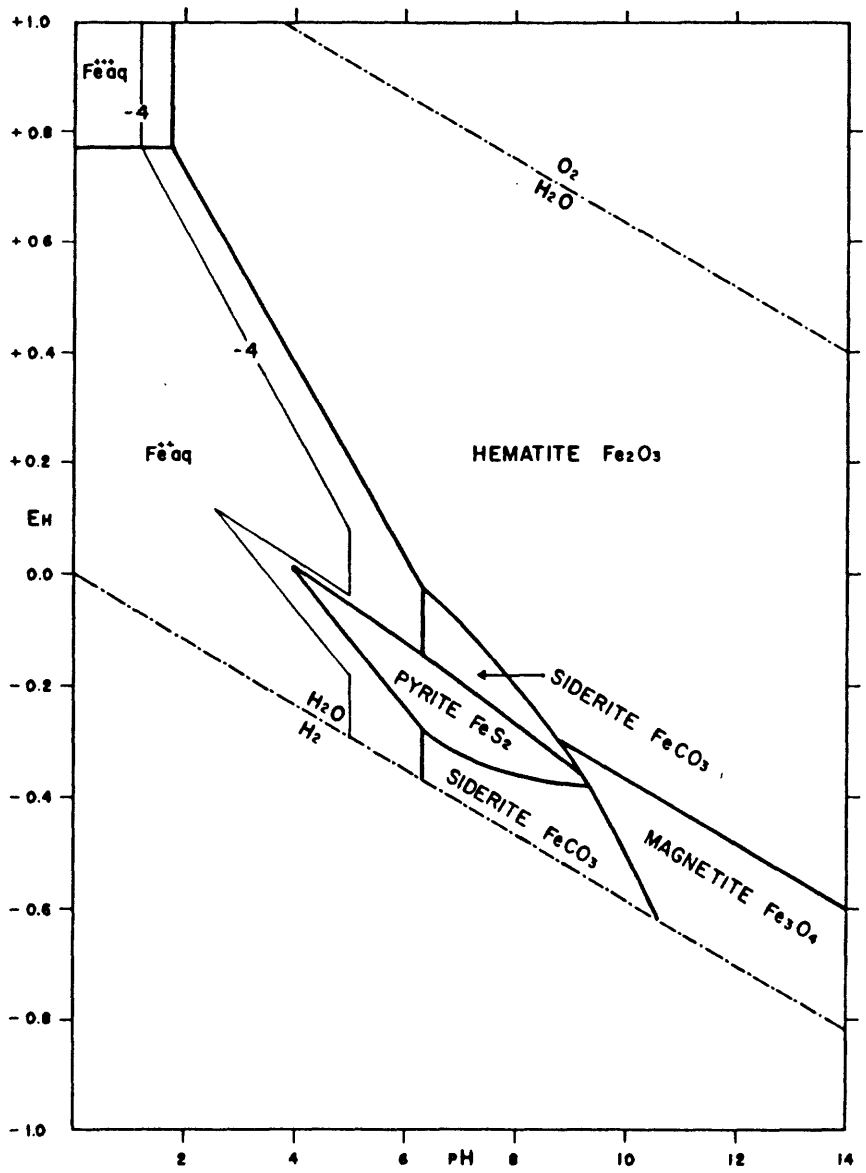

Figure 49. Stability relations of iron oxides, sulfides, and carbonate in water at 25° C and one atmosphere total pressure. Total dissolved sulfur=10^{-6}. Total dissolved carbonate=10^{0}. Note the elimination of FeS field by $FeCO_3$ under strongly reducing conditions, and stability of pyrite in the presence of small amounts of dissolved sulfur (Garrels and Christ, 1965).

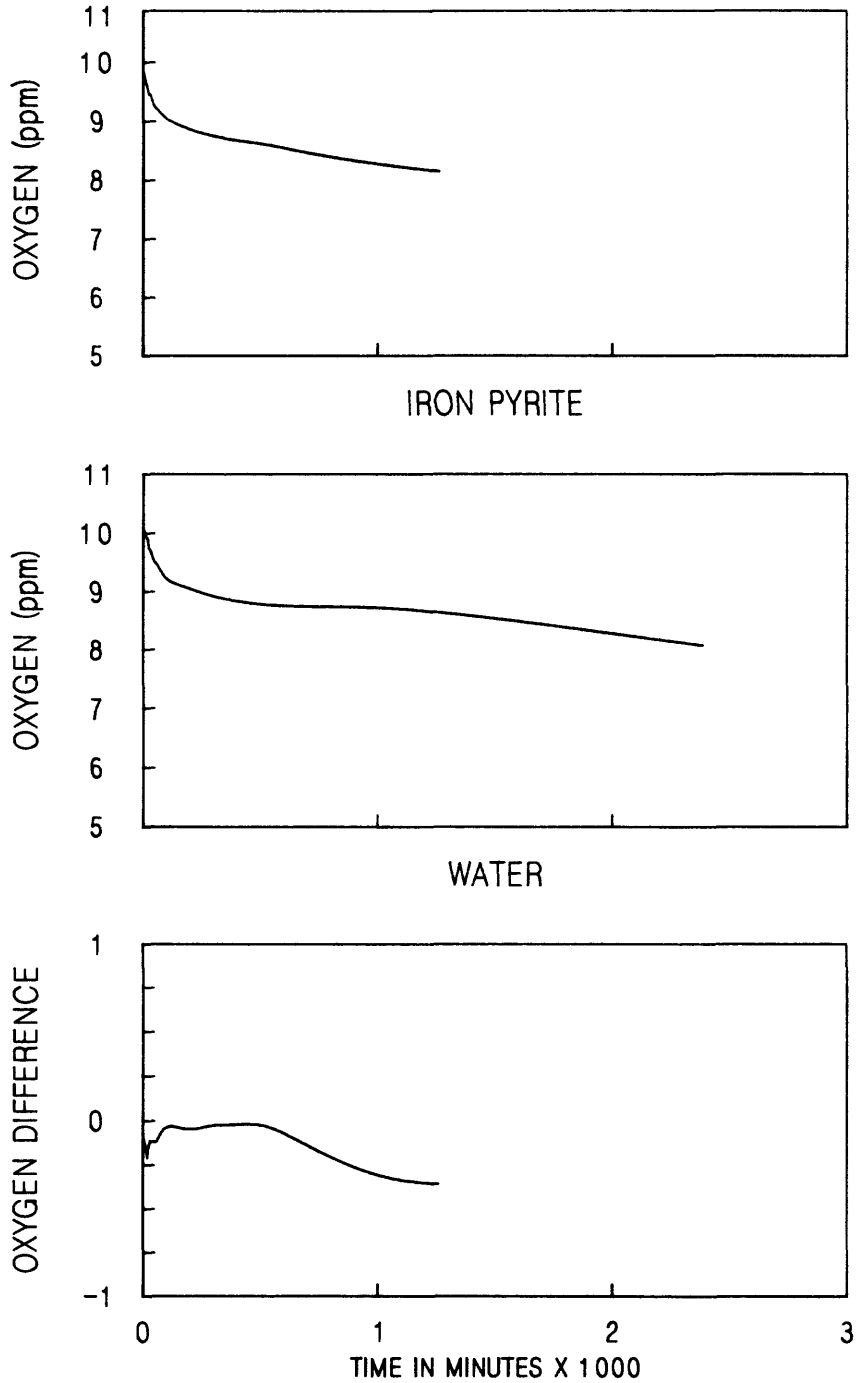

Figure 50. Oxygen behaviors of iron pyrite injected into acidic water, water injected into acidic water, and the difference between them in ppm dissolved oxygen.

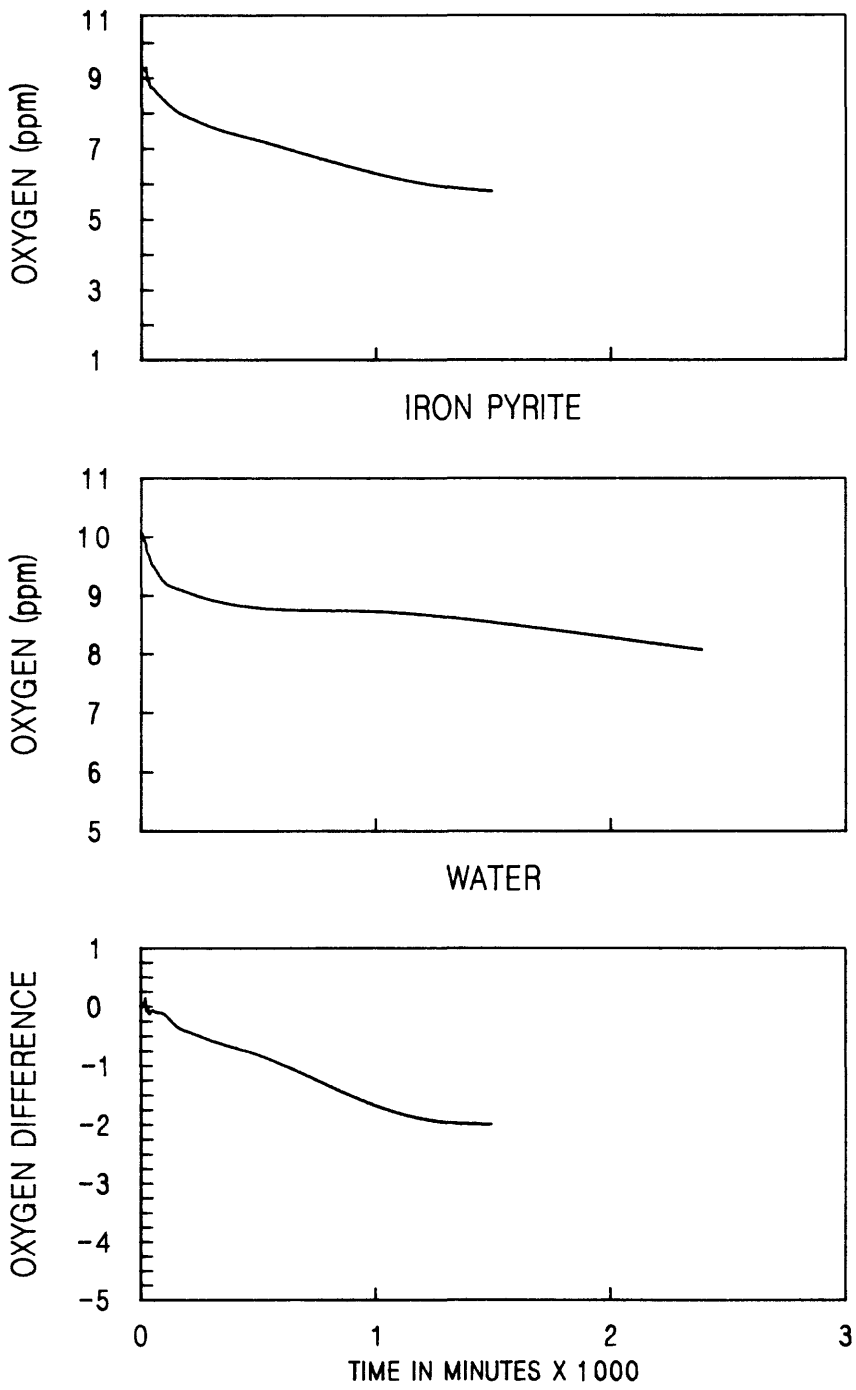

Figure 51. Oxygen behaviors of iron pyrite injected into neutral water, water injected into neutral water, and the difference between them in ppm dissolved oxygen.

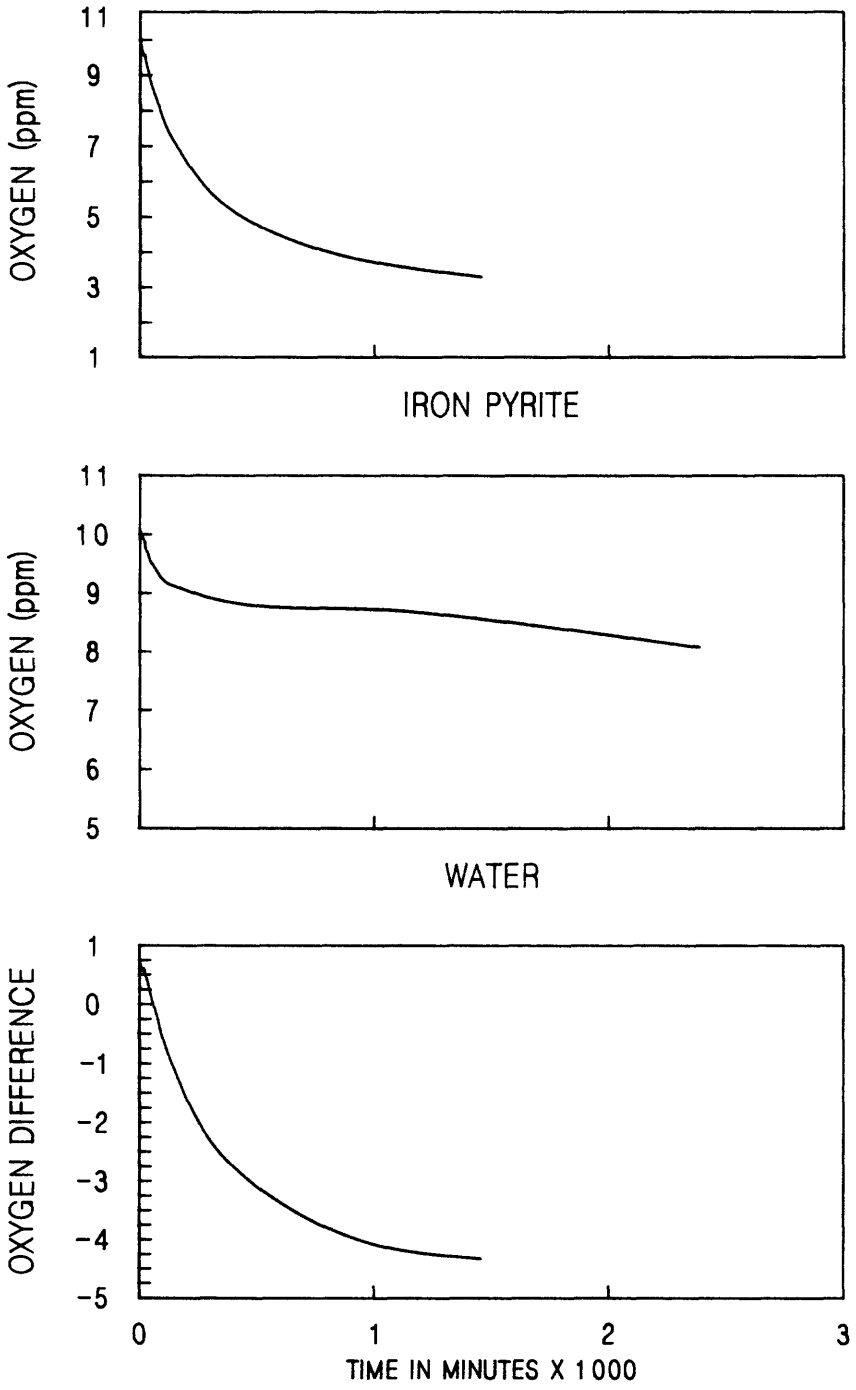

Figure 52. Oxygen behaviors of iron pyrite injected into basic water, water injected into basic water, and the difference between them in ppm dissolved oxygen.

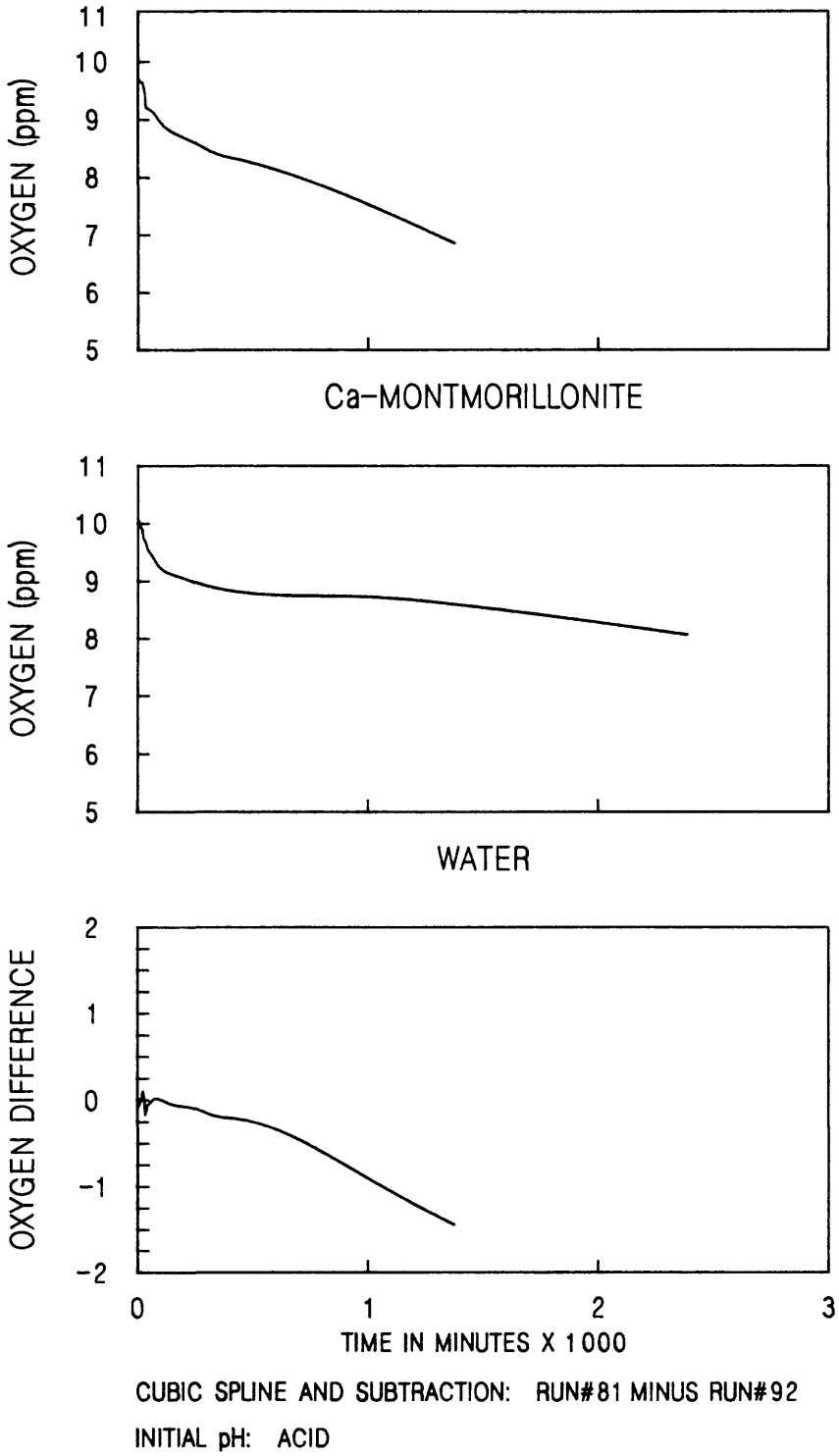

Figure 53. Oxygen behaviors of calcium montmorillonite injected into acidic water, water injected into acidic water, and the difference between them in ppm dissolved oxygen.

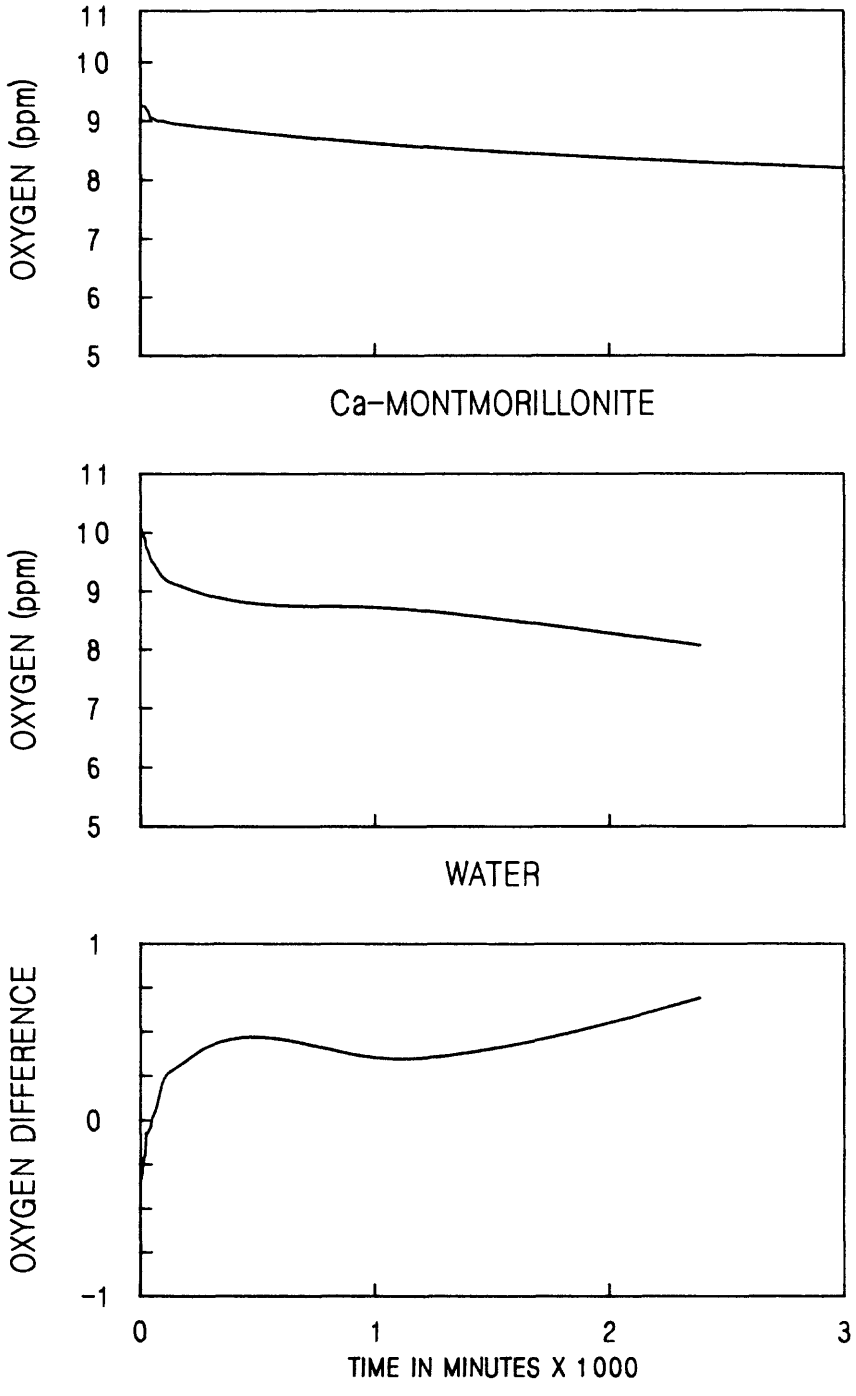

Figure 54. Oxygen behaviors of calcium montmorillonite injected into neutral water, water injected into neutral water, and the difference between them in ppm dissolved oxygen.

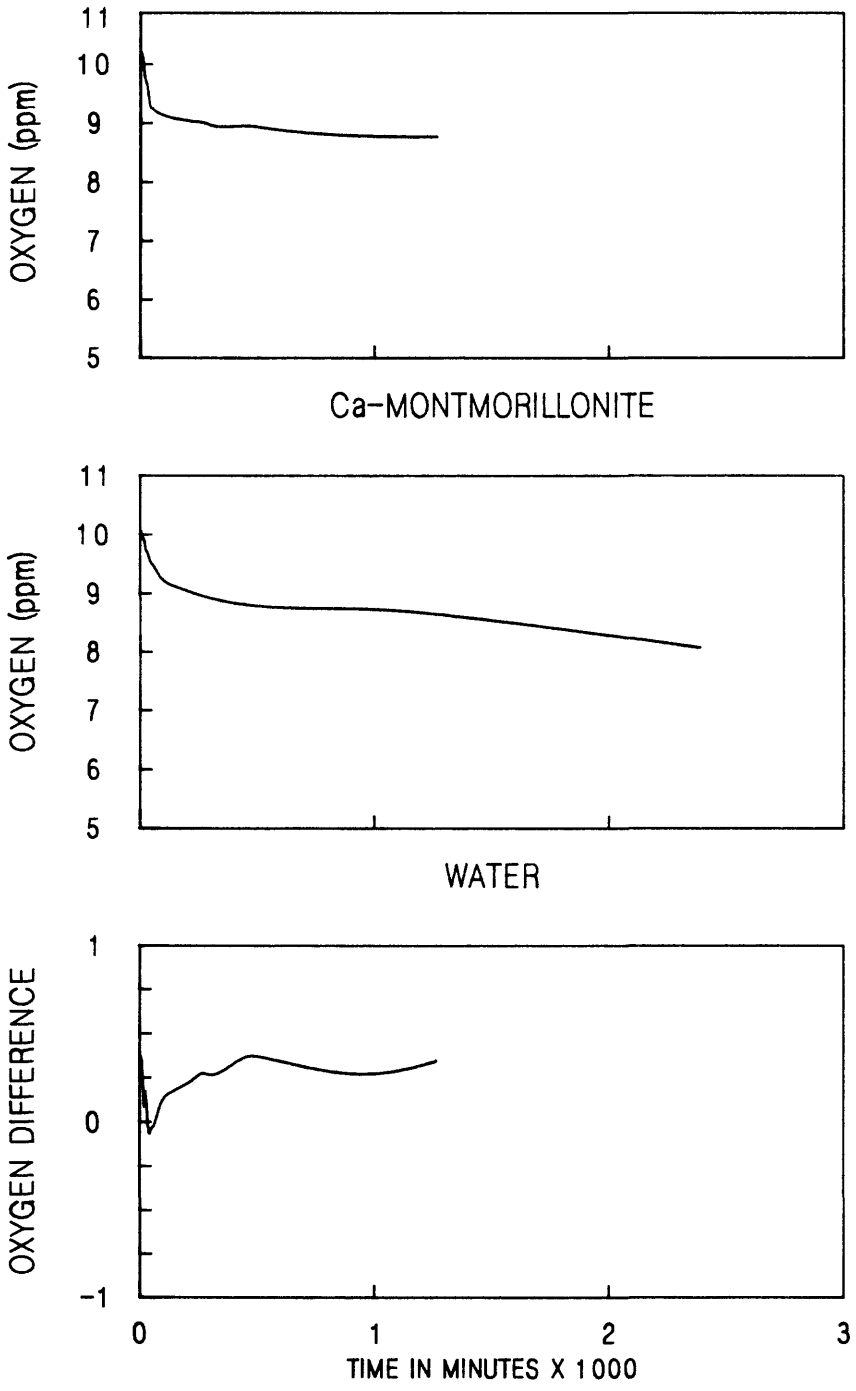

Figure 55. Oxygen behaviors of calcium montmorillonite injected into basic water, water injected into basic water, and the difference between them in ppm dissolved oxygen.

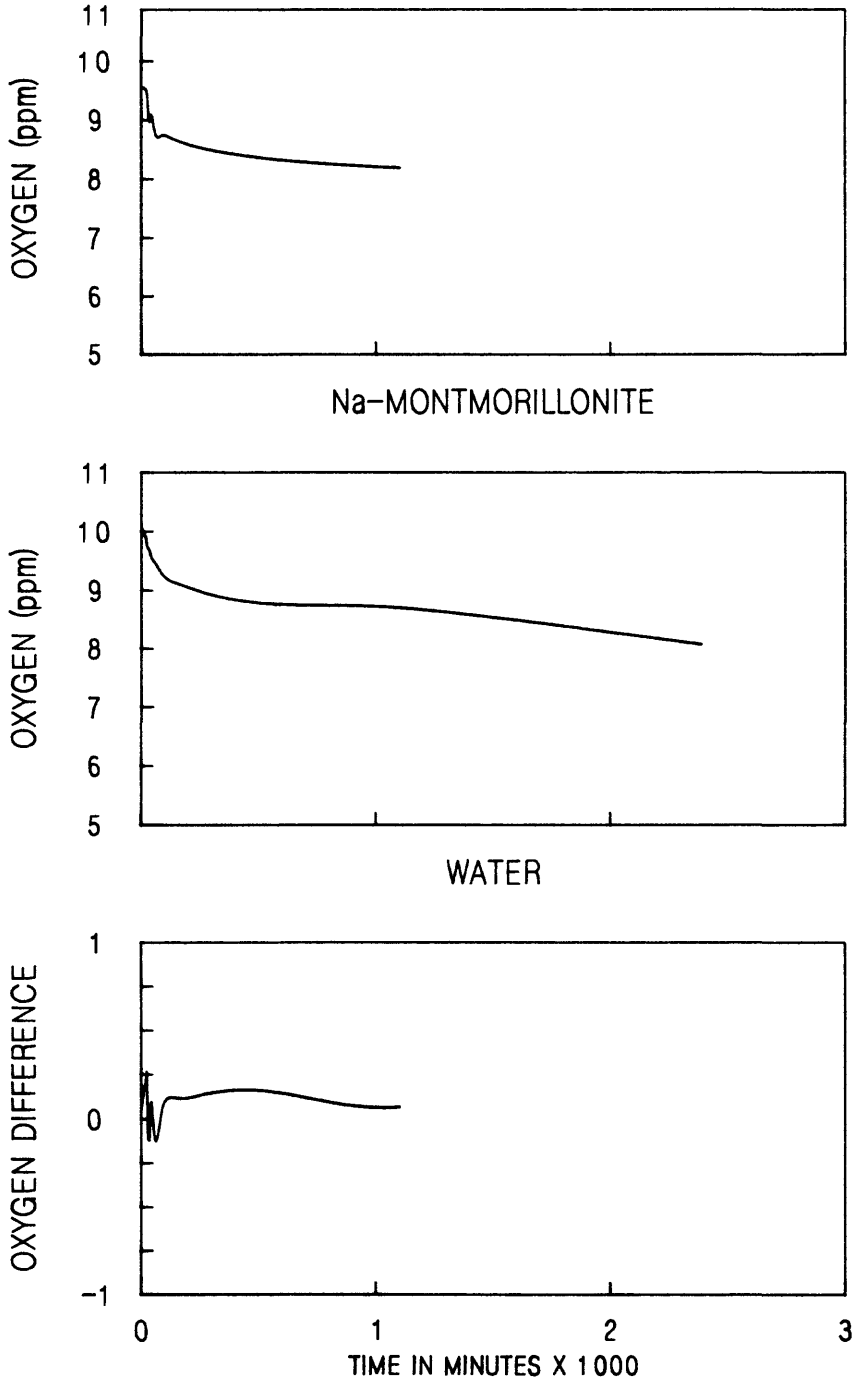

Figure 56. Oxygen behaviors of sodium montmorillonite injected into acidic water, water injected into acidic water, and the difference between them in ppm dissolved oxygen.

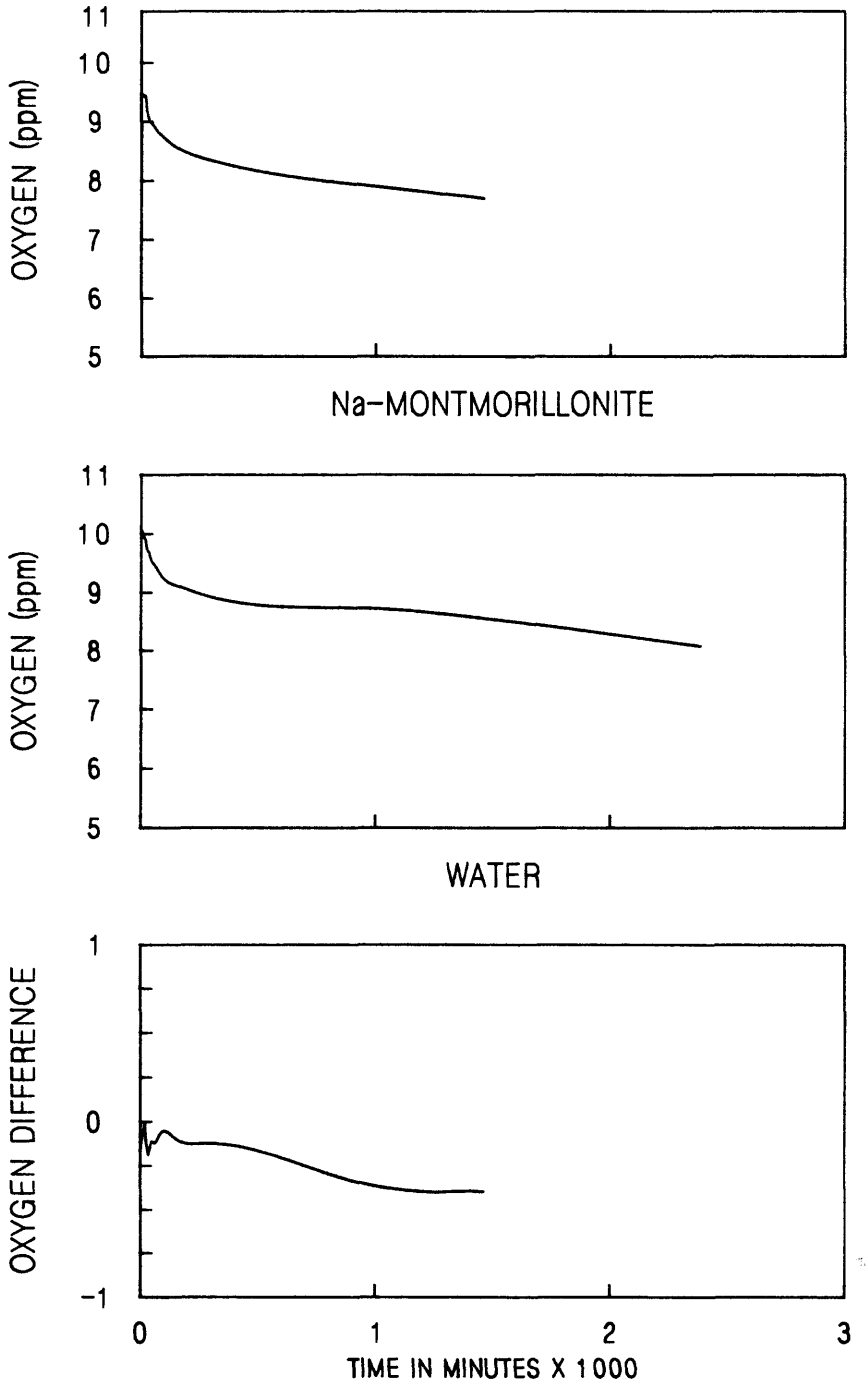

Figure 57. Oxygen behaviors of sodium montmorillonite injected into neutral water, water injected into neutral water, and the difference between them in ppm dissolved oxygen.

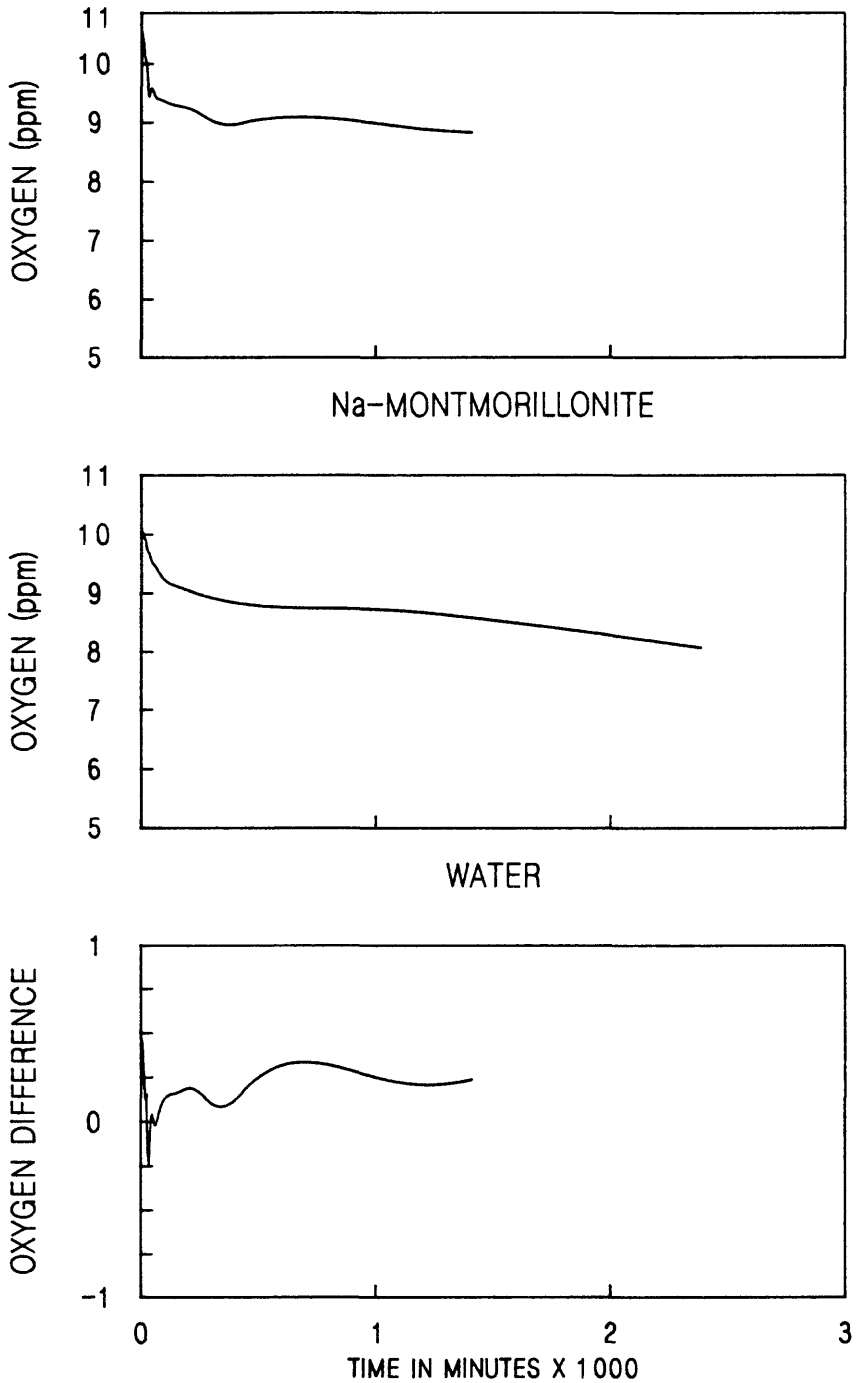

Figure 58. Oxygen behaviors of sodium montmorillonite injected into basic water, water injected into water, and the difference between them in ppm dissolved oxygen.

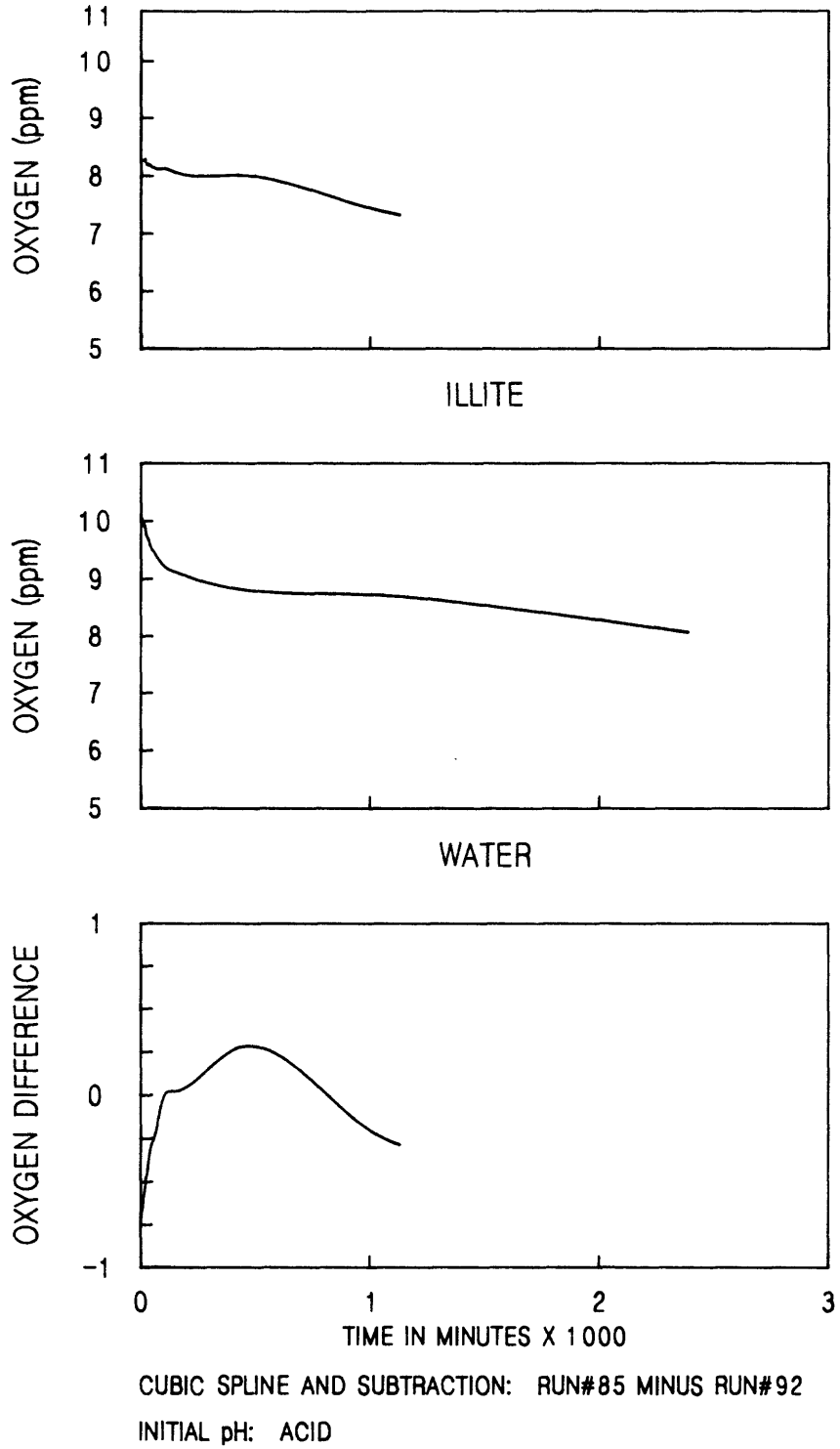

Figure 59. Oxygen behaviors of illite injected into acidic water, water injected into water, and the difference between them in ppm dissolved oxygen.

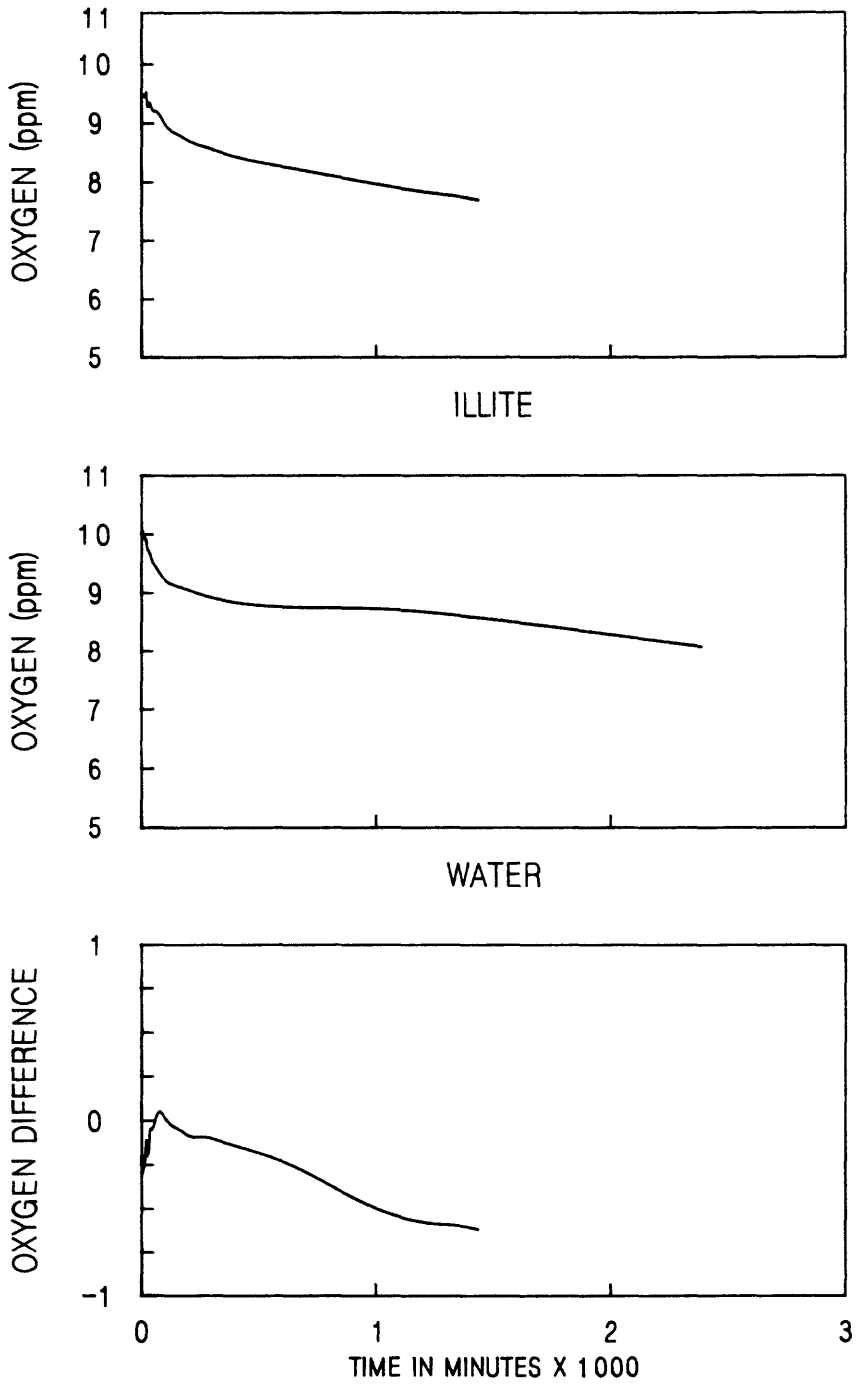

Figure 60. Oxygen behaviors of illite injected into neutral water, water injected into water, and the difference between them in ppm dissolved oxygen.

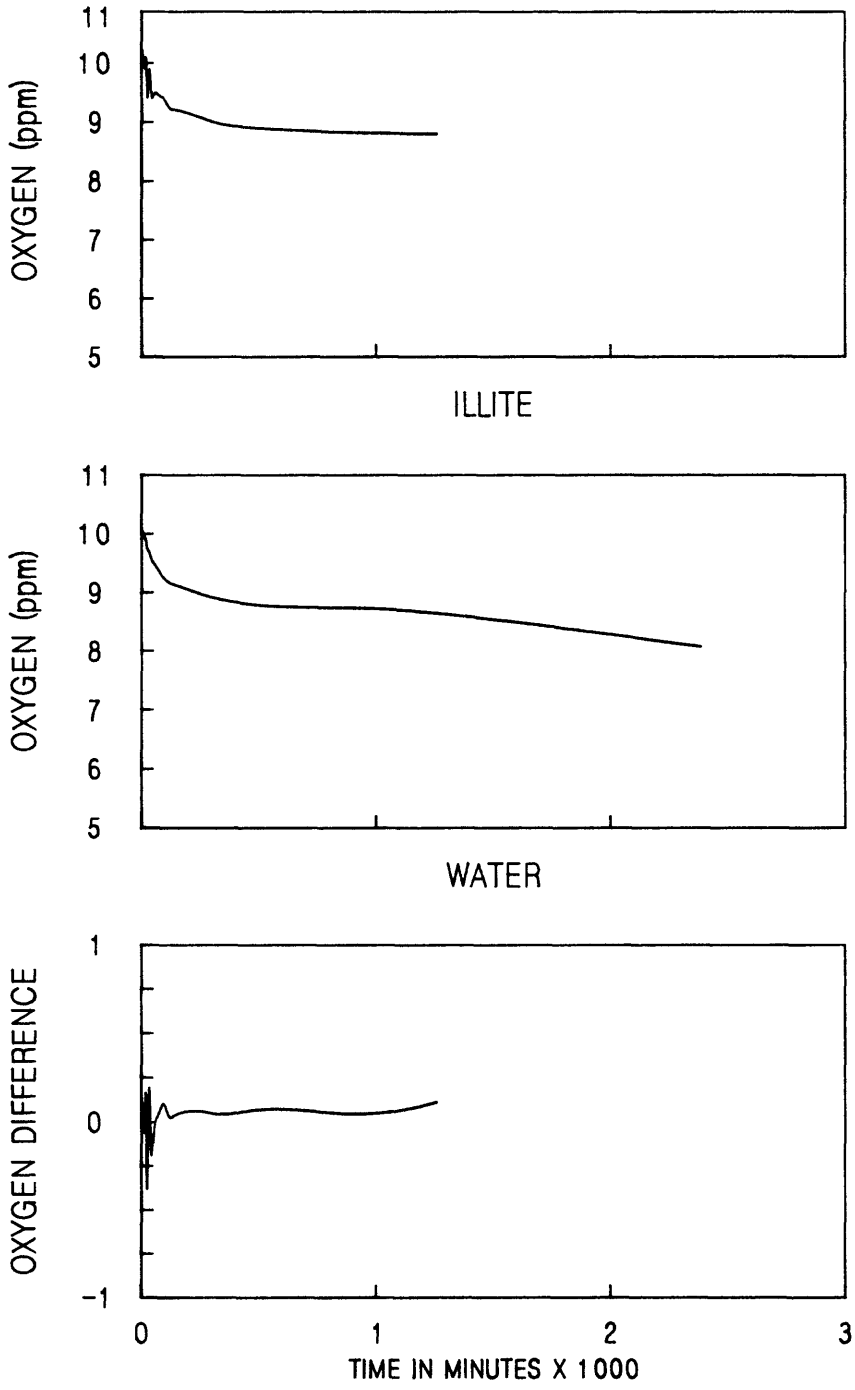

Figure 61. Oxygen behaviors of illite injected into basic water, water injected into water, and the difference between them in ppm dissolved oxygen.

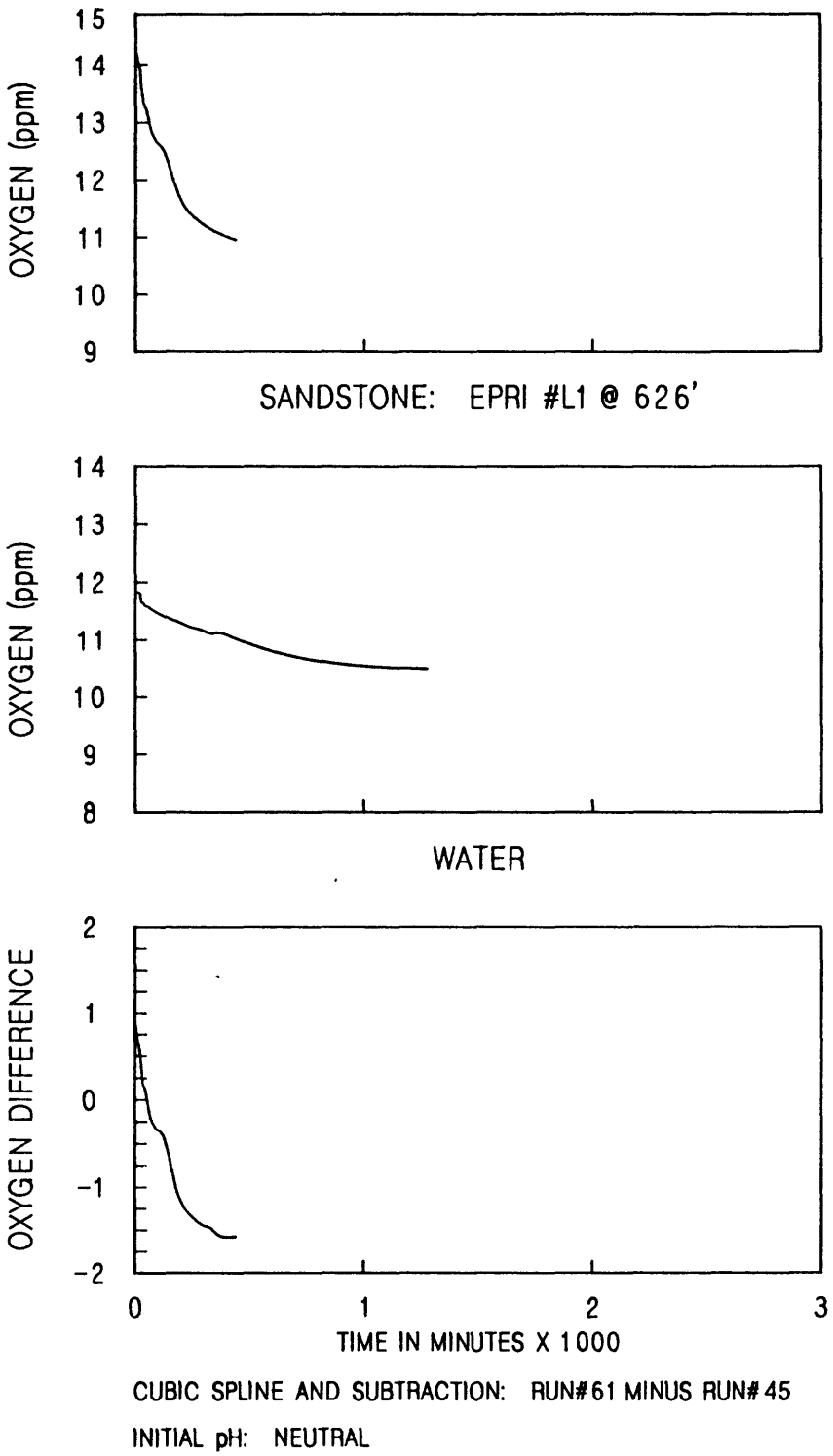

Figure 62. Oxygen behaviors of L-1 626' injected into neutral water, water injected into water, and the difference between them in ppm dissolved oxygen.

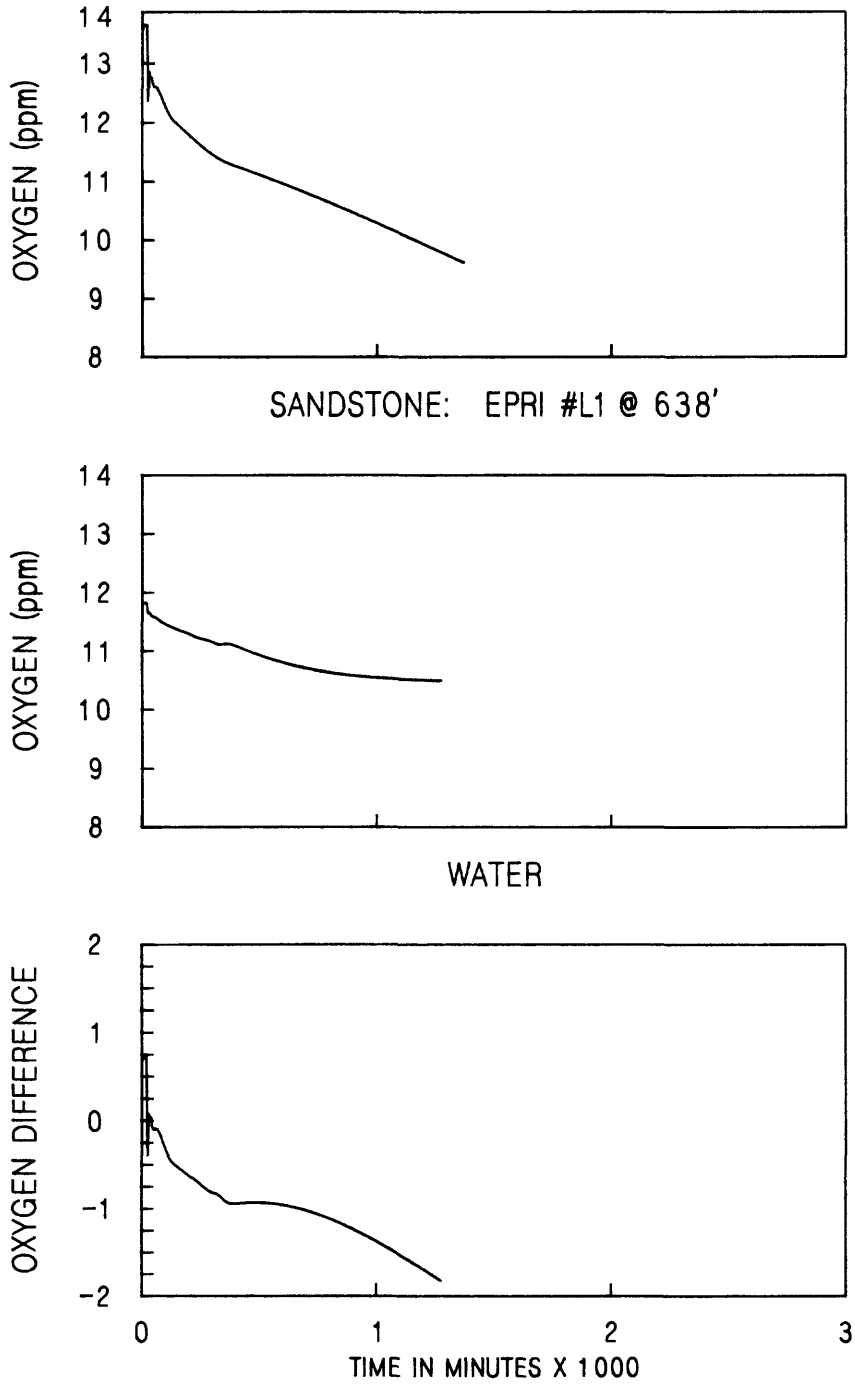

Figure 63. Oxygen behaviors of L-1 638' injected into neutral water, water injected into water, and the difference between them in ppm dissolved oxygen.

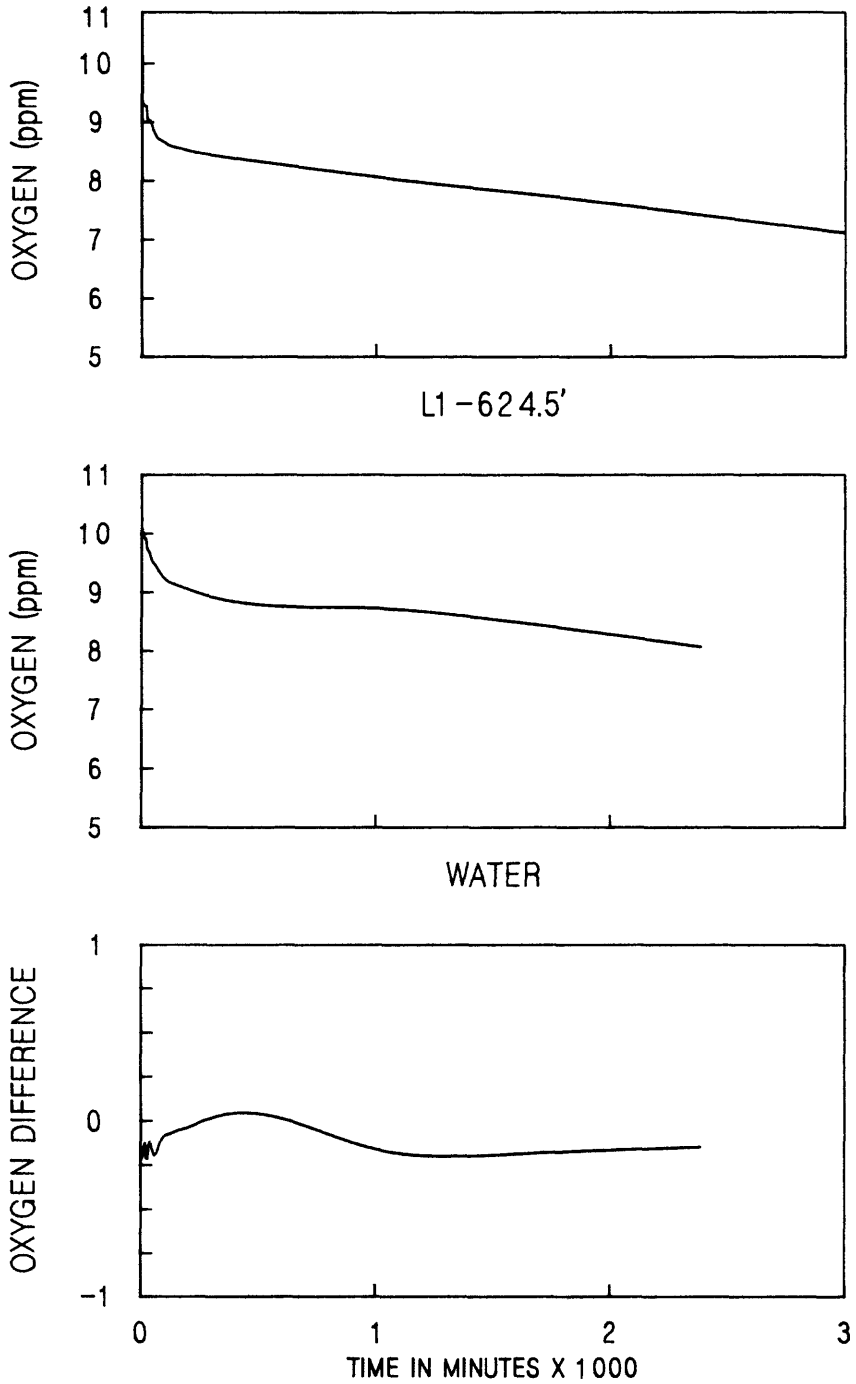

Figure 64. Oxygen behaviors of L-1 624.5' injected into neutral water, water injected into water, and the difference between them in ppm dissolved oxygen.

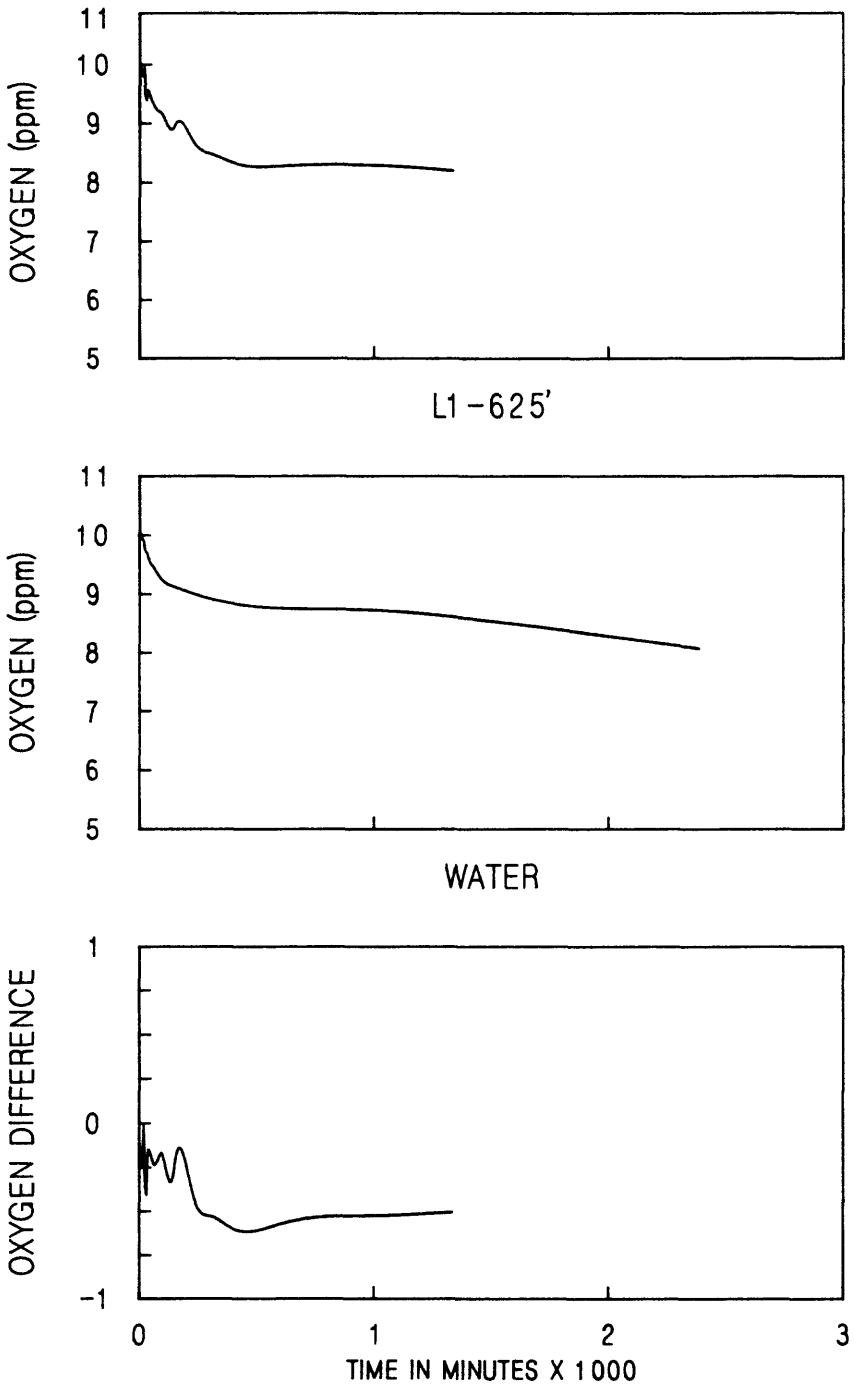

Figure 65. Oxygen behaviors of L-1 625' injected into acidic water, water injected into water, and the difference between them in ppm dissolved oxygen.

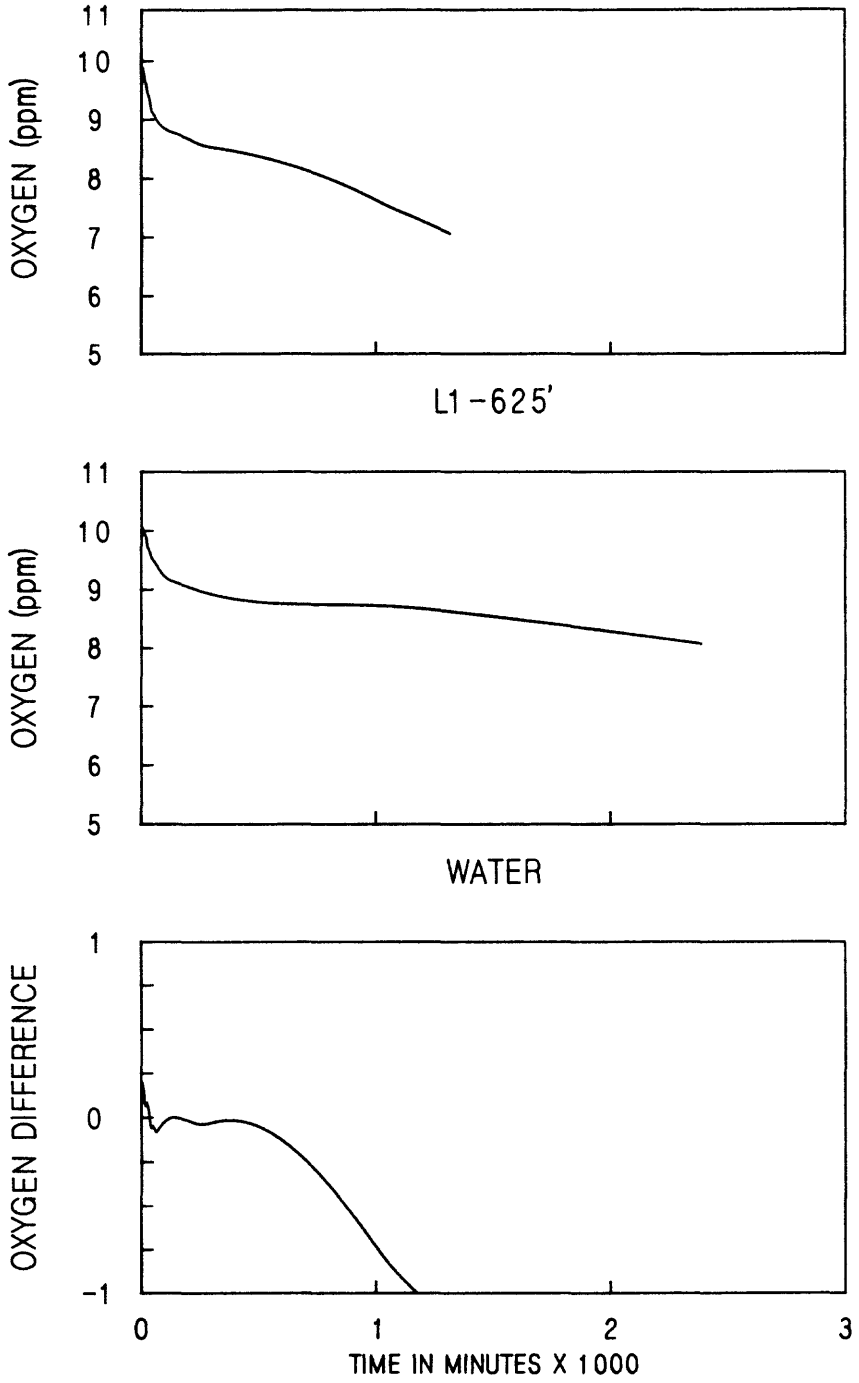

Figure 66. Oxygen behaviors of L-1 625' injected into neutral water, water injected into water, and the difference between them in ppm dissolved oxygen.

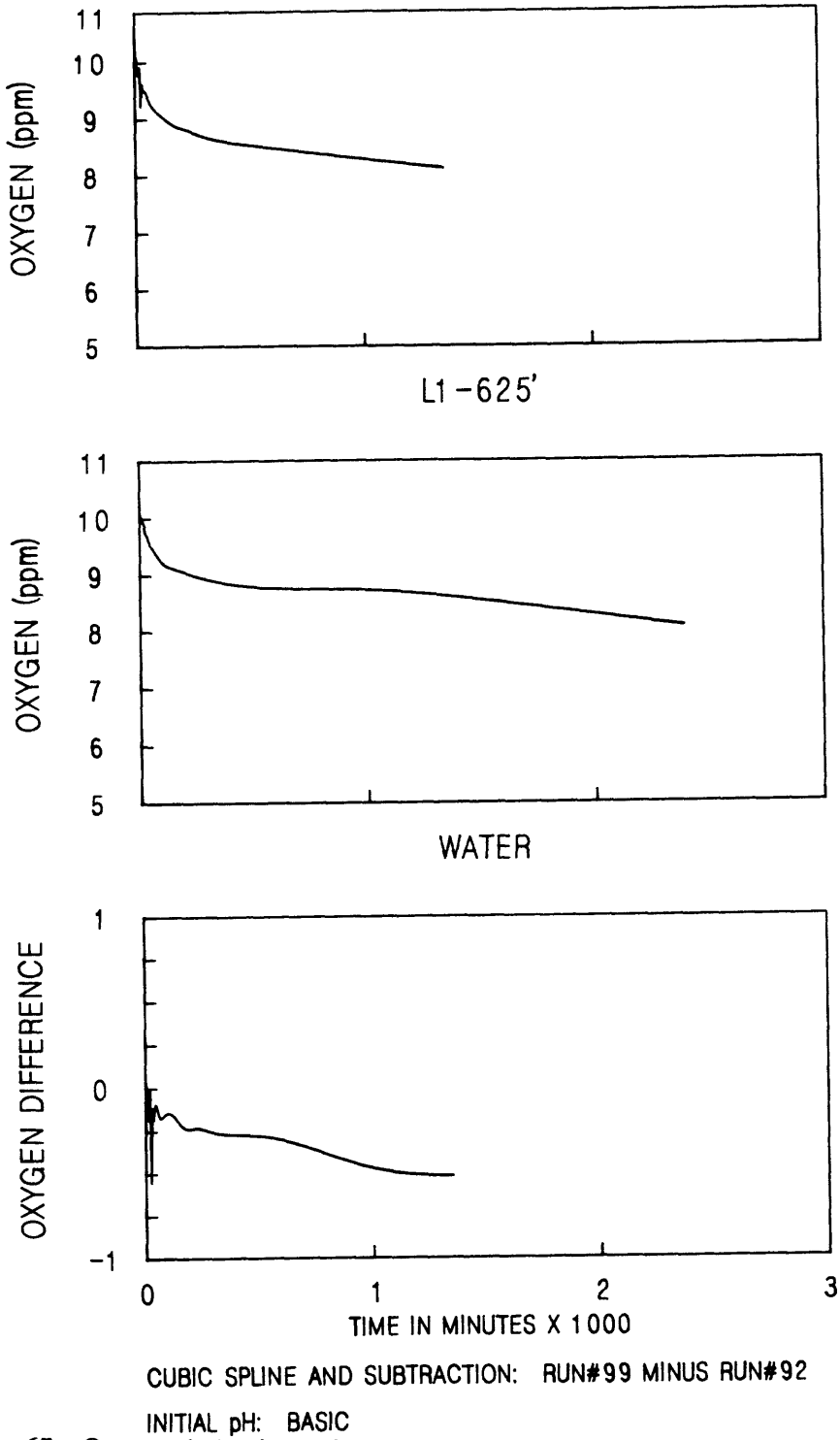

Figure 67. Oxygen behaviors of L-1 625' injected into basic water, water injected into water, and the difference between them in ppm dissolved oxygen.

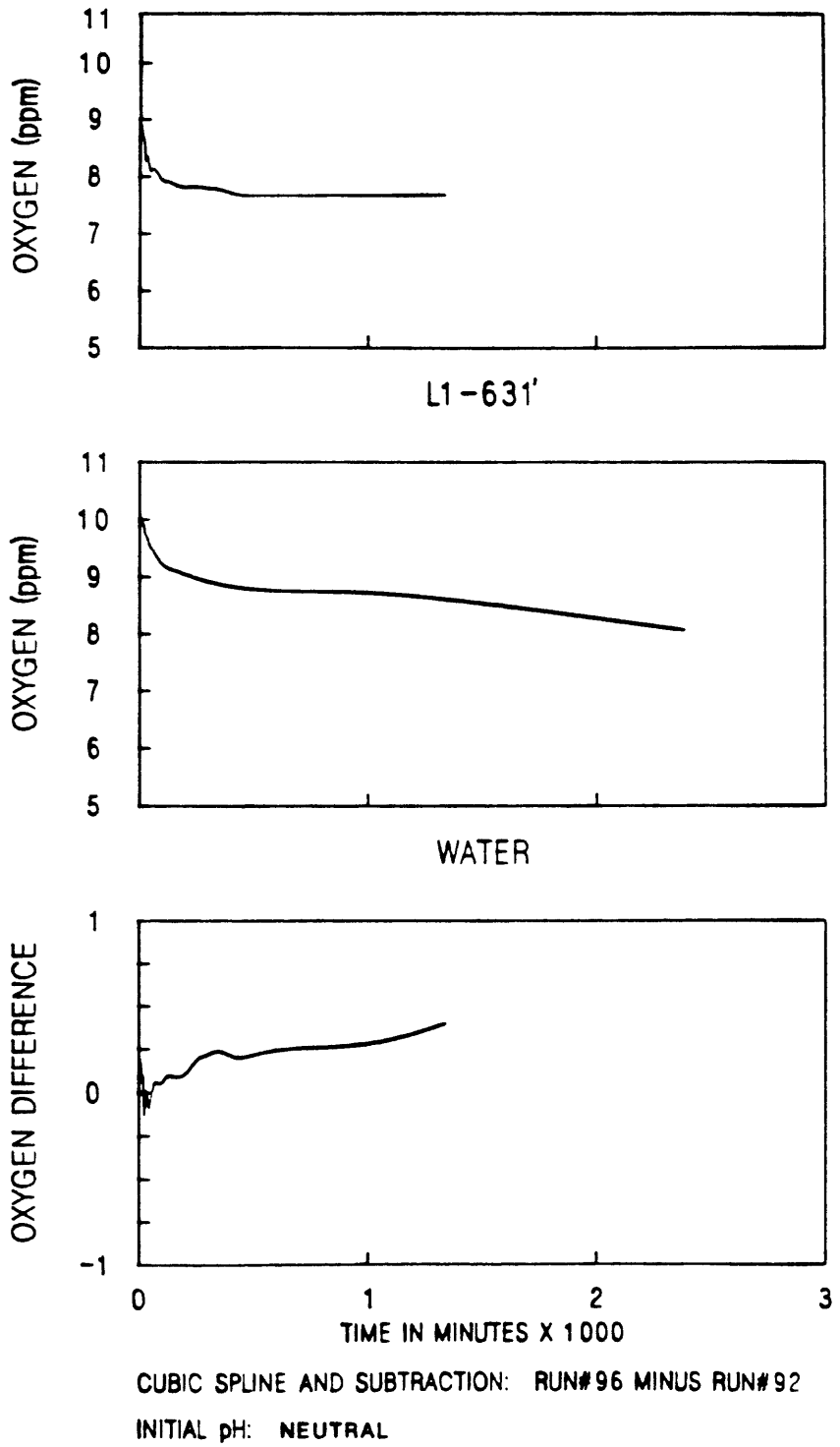

Figure 68. Oxygen behaviors of L-1 625' injected into neutral water, water injected into water, and the difference between them in ppm dissolved oxygen.

ERROR AND BIAS

The sources of experimental error can be divided into systematic and non-systematic regimes. The systematic errors are the result of faults in technique, calibration, instrument drift, and bias on the part of the observer. Non-systematic errors are the result of individual faults of measurement, transient environmental effects, and statistical variation. Non-systematic errors are usually easier to deal with in that their effect is obvious and they do not fit the usually pattern of the data. Systematic errors are more subtle and hard to detect in that the error is propagated through the measurement process (Bevington, 1969).

There are five measurement systems operating: oxygen content, pH, Eh, temperature, and time. Time is measured in minutes, and it is the difference between the particular measurement time and the beginning of the measurement process that is relevant. The error is estimated to be plus or minus five seconds as timed with a digital watch. The oxygen probe system is calibrated before and after each measurement cycle using a mercury barometer located in the same building. The barometer measures absolute atmospheric pressure.

The pH system is calibrated every two days. It is calibrated according to the instrument handbook to two reference solutions. The redox measurement system is checked every two days in accordance with the operations manual (Orion Research, 1983).

The mean and standard deviation for the oxygen content, Eh, and pH are calculated from the following equations.

mean $\quad x = (1/N)\ \Sigma x_i$

standard deviation $\quad \sigma = \{(1/N\text{-}1)\ \Sigma(x_i - x)^2\}^{1/2}$

Where N is the number of data points, and x_i is the measured value of a data point.
The following table lists standard deviations, σ, for dissolved oxygen, pH, and Eh for some of the representative systems measured.

System	$\sigma(Po_2)$	σ(pH)	σ(Eh)
Blank	0.09ppm	0.27	8mv
Water	0.31ppm	0.27	25mv
Pyrite	1.10ppm	0.68	189mv
Ca-montmorillonite	0.29ppm	1.39	36mv
Na-montmorillonite	0.46ppm	2.64	148mv
Illite	0.64ppm	1.51	90mv
625'	0.84ppm	2.51	156mv

This table shows that the changes in the system caused by injection of samples are measurably significant compared to the standard deviation of error in the measurements.

CONCLUSIONS AND RECOMMENDATIONS

The evidence of this study indicates that the sandstone lithology from EPRI well L-1 at 625' will deplete oxygen from aqueous solution in an acid or neutral environment. The cause of this oxygen depletion is not likely caused only by pyrite. It is also caused by the oxidation of iron-bearing illite coating the surfaces of the quartz grains of the sandstone. In an acidic environment, pyrite did not produce appreciable oxygen depletion and clay did. In a basic environment, the iron pyrite reacted, consuming oxygen, while the clay did not. The stability of iron pyrite in the Eh-pH range shown in Figure 49 generally agrees with the results of Garrels and Christ (1965, p.221), who suggest (1965, p.224) that the addition of carbonate to this system will reduce the size of the Eh-pH stability region for pyrite. As the Pittsfield site does contain carbonates, the stability field for pyrite is very small.

In order to minimize the loss of oxygen stored in a geologic reservoir, the pH of the reservoir should be disturbed minimally by the processes of drilling and completion. Small changes in pH can have pronounced effects on the chemical stability of iron-bearing minerals causing them to oxidize in response to the presence of oxygen. The loss of oxygen content from the air stored the the St. Peter Formation at Pittsfield, Illinois, was caused primarily by the presence of iron-bearing minerals, and enhanced by the use of acid in the completion process.

APPENDIX A - EQUIPMENT LIST

The following is the pertinent equipment list for this series of measurements.

oxygen probe, Orion Research model 97-08

pH probe, VWR Scientific #43100-975

pH meter, Nester Instruments model 2000

Eh probe, Orion Research model 96-78-00

Eh and oxygen meter, Orion Research model 611

environment chamber, LABCONCO #50004

gas washing bottle, 500 ml, Pyrex

magnetic stirrer, Toyo model 16B

glass corrosion vessel, Princeton Applied Research

reaction vessel, Allen Scientific, custom model

conductivity cell, YSI model 3403

syringe, plastic disposable, 50ml

scanning electron microscope, Cambridge Stereo Scan 250 Mk 2

surface area analyzer, Micromeritics FlowSorb II 2300

spectrophotometer UV-VIS-NIR, Beckman UV 5270

FTIR mid-infrared spectrometer, Nicolet 740

flexible polymer membrane, Parafilm

APPENDIX B - REFERENCE CLAYS

The reference sample materials are:

SWy-1, a Na-montmorillonite from Crook County, Wyoming
STx-1, a Ca-montmorillonite from Gonzales County, Texas
IMt-1, an illite from Silver Hill, Montana
KGa-1, a kaolinite from Warren County, Georgia
iron pyrite from Georgetown, Colorado
fumed silica, Cabot brand Cab-O-Sil, Boston, Massachusetts

All of the clay samples were obtained from the Source Clay Minerals Repository, Department of Geology, University of Missouri, Columbia, Missouri, USA. (Van Olphen and Fripiat, 1979).

APPENDIX C - SURFACE AREA MEASUREMENTS

Sample	Surface Area (m^2/gram)
L-1 624.5	4.29
L-1 625'	2.97
L-1 638'	0.47
SWy-1	31.82
STx-1	83.79
Georgetown pyrite	0.05

APPENDIX D - CHEMICAL ANALYSIS WELL L-1 (Plumlee and Ridley, 1989)

Component	640.6'	638'	624.5'	631'	635.3
SiO_2	95.4	96.8	96.3	98.5	98.1
Al_2O_3	1.53	1.0	1.32	0.34	0.24
FeO	0.23	0.26	0.22	<0.04	0.15
MgO	0.21	0.14	0.17	<0.10	0.12
CaO	0.02	0.06	<0.02	0.06	0.45
Na_2O	<0.15	<0.15	<0.15	<0.15	<0.15
K_2O	0.86	0.59	0.78	0.20	0.07
TiO_2	0.08	0.04	0.05	<0.02	<0.02
P_2O_5	<0.05	<0.05	<0.05	<0.05	<0.05
MnO	<0.02	<0.02	<0.02	<0.02	<0.02
total	98.55	99.11	99.08	99.48	99.37

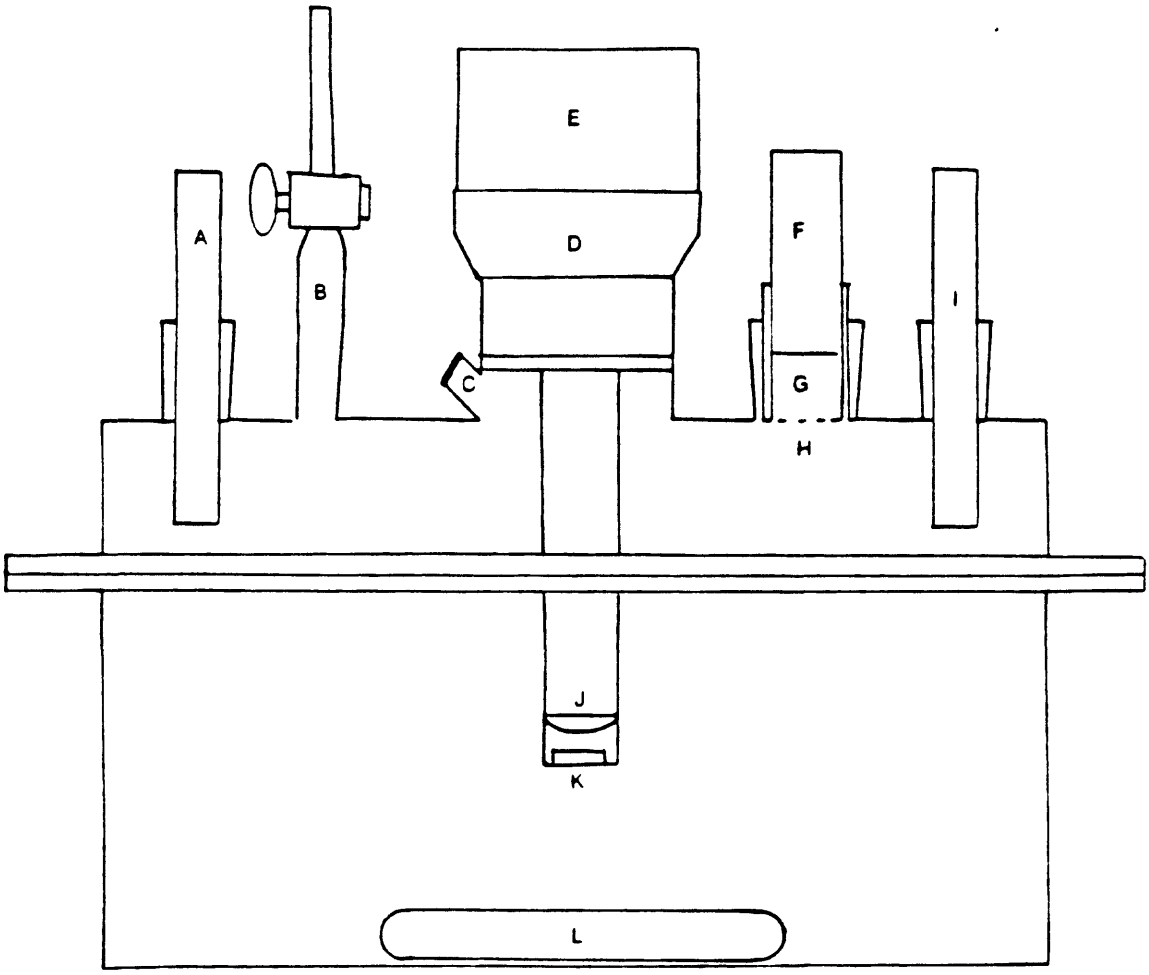

Figure 69. Schematic diagram of reaction vessel. A - pH probe; B - overflow valve; C - gas sample port; D - oxygen probe funnel; E - oxygen probe electronics; F - plunger; G - sample; H - polymer membrane; I - Eh probe; J - oxygen membrane; K - oxygen membrane stir bar; L - main stir bar.

REFERENCES

Aagaard, P. and Helgeson, H.C., 1982, Thermodynamic and kinetic constraints on reaction rates among minerals and aqueous solutions -- I. Theoretical considerations: Am. J. Sci., v. 282, p. 237-285.

Addison, W.E. and Sharp, J.H., 1963, Redox behavior of iron in hydroxylated silicates: Clays Clay Minerals, v. 11, p. 95-104.

Amonette, J., Ismail, F.T. and Scott, A.D., 1985, Oxidation of iron in biotite by different oxidizing solutions at room temperature: Soil Sci. Soc. Am. J., v.49, p. 772-777.

Anderson, W.L. and Stucki, J.W., 1978, Effect of structural Fe^{2+} on visible absorption spectra of nontronite suspensions: in Proc.Int'l.Clay Conf. (Oxford, 1978), M.M. Mortland and V.C. Farmer, eds., Amsterdam, Elsevier, p. 75-83.

Badaut, D., Besson, G., Decarreau, A. and Rautureau, M., 1985, Occurrence of a ferrous, trioctahedral smectite in recent sediments of Atlantis II Deep, Red Sea: Clay Minerals, v. 20, p. 389-404.

Bahranowski, K., Dubiel, S. and Stoch, L., 1981, Iron in the structure of some clay minerals and its extraction with 15% sulfuric acid in the light of Mossbauer spectroscopy: Mineral. Pol., v. 12, p. 3-14.

Barshad, I. and Kishk, F.M., 1968, Oxidation of ferrous iron in vermiculite and biotite alters fixation and replaceability of potassium: Science, v. 162, p. 1401-1402.

Bart, J.C., Burriesci, N., Cariati, F., Micera, G. and Gessa, C., 1980, Spectroscopic investigations of iron distribution in some bentonites from Sardinia: Clays Clay Minerals, v. 28, p. 233-236.

Besson, G., Drits, V.A., Daynyak, L.G. and Smoliar, B.B., 1987, Analysis of cation distribution in dioctahedral micaceous minerals on the basis of IR spectroscopy data: Clay Minerals, v. 22, p. 465-478.

Bevington, P. R., 1969, Data reduction and error analysis for the physical sciences: NY, McGraw-Hill, 336p.

Beyme, B. and von Reichenbach, H. Graf, 1977, Oxidation of structural Fe in an altered biotite with H_2O_2 under controlled redox conditions: Proc. 3rd European Clay Conf. (Oslo), v.1, p.10-21.

Bloomfield, C., 1972, The oxidation of iron sulfides in soils in relation to the formation of acid sulfate soils and ochre deposits in field drains: J.Soil Sci., v.23, p.1-16.

Bonnin, D., Calas, G., Suquet, H. and Pezerat, H., 1985, Site occupancy of Fe^{3+} in Garfield nontronite: a spectroscopic study: Phys.Chem.Miner., v. 12, p. 55-64.

Borchardt, G.A., 1977, Montmorillonite and other smectite minerals: in Minerals in soil environments, J.B. Dixon and S.B. Weed, co-eds., Madison, WI, Soil Sci. Soc. Am., p.293-330.

Bouda, S. and Isaac, K.P., 1986, Influence of soil redox conditions on oxidation of biotite: Clay Minerals, v. 21, p. 149-157.

Brigatti, M.F., 1983, Relationships between composition and structure in Fe-rich smectites: Clay Minerals, v. 18, p. 177-186.

Brindley, G. W., 1980, Order-disorder in clay mineral structures: in Crystal structures of clay minerals, G.W. Brindley and G. Brown eds, London, Mineralogical Society of London, p.125-195.

Chen, Y., Shaked, D., and Banin, A., 1979, The role of structural iron(III) in the UV absorption by smectites: Clay Minerals, v. 14, p. 93-102.

Core Laboratories, 1987, Preliminary progress report RP-8000-8 mineralogical and geochemical assessment of porous media for compressed air storage: Irving, Texas, 16 p.

Craciun, C., 1984, Influence of the Fe(+3) -for- Al(+3) octahedral substitutions on the IR spectra of montmorillonite minerals: Spectroscopy Lttrs., v. 17, p. 579-590.

Craw, D., 1981, Oxidation and microprobe-induced potassium mobility in iron-bearing phyllosilicates from the Otago Schists, New Zealand: Lithos., v. 14, p. 49-57.

Craw, D., 1984, Ferrous-iron-bearing vermiculite-smectite series formed during alteration of chlorite to kaolinite, Otago Schist, New Zealand: Clay Minerals, v. 19, p. 509-520.

De Vine, C.S. and Davies, D.K., 1985, Post-test geological and geochemical evaluation -- dolomite, dolomite/sandstone transition, and sandstones -- wells E-1, I-1, and K-1, Compressed air energy storage site, Pike County (near Pittsfield), Illinois: report prepared for John Istvan, PB-KBB, Inc., Houston, TX, David K. Davies Assoc., Inc., var.pag.

EPRI (Electric Power Research Institute), 1987, Proc. Geotechnology workshop on compressed-air energy storage in porous media sites (Traverse City, MI, Sept. 23-24, 1986), Palo Alto, EPRI AP-5301 proj. 2488-10, var.pag.

Eslinger, E., Highsmith, P., Albers, D. and De Mayo, B., 1979, Role of iron reduction in the conversion of smectite to illite in bentonite in the disturbed belt, Montana: Clays Clay Minerals, v. 27, p. 327-338.

Fanning, D.S., Rabenhorst, M.C., May, L. and Wagner, D.P., 1989, Oxidation state of iron in glauconite from oxidized and reduced zones of soil-geologic columns: Clays Clay Minerals, v. 37, p. 59-64.

Farmer, V.C. and Russell, J.D., 1964, The infrared spectra of silicates: Spectrochim.Acta, v. 20, p. 1149-1173.

Farmer, V.C., ed., 1974, The infrared spectra of minerals: London, The Mineral.Soc., 539p.

Farmer, V.C., Russell, J.D. and Ahlrichs, J.L., 1968, Characterization of clay minerals by infrared spectroscopy: Trans.9th Int'l.Congr. Soil Sci.(Adelaide), v.3, p. 101-110.

Farmer, V.C., Russell, J.D., McHardy, W.J., Newman, A.C.D., Ahlrichs, J.L. and Rimsaite, J.Y.H., 1971, Evidence for loss of protons and octahedral iron from oxidized biotites and vermiculites: Mineral. Mag., v.38, p. 121-137.

Fleischer, M., 1983, Glossary of mineral species: Tucson, Arizona, The Mineralogical Record Inc., 202 p.

Folk, R. L., 1974, Petrology of sedimentary rocks: Austin, Texas, Hemphill Publishing Co., 182 p.

Garrels, R. M. and Christ, C. L., 1965, Solutions, minerals, and equilibria: San Francisco, Freeman, Cooper and Co., 450 p.

Gilkes, R.J., Young, R.C. and Quirk, J.P., 1972, Oxidation of ferrous iron in biotite: Nature, v. 236, p. 89-91.

Gilkes, R.J., Young, R.C. and Quirk, J.P., 1972, The oxidation of octahedral iron in biotite: Clays and Clay Minerals, v.20, p. 303-315.

Gilkes, R.J., Young, R.C. and Quirk, J.P., 1973, Artificial weathering of oxidized biotite -- II. Rates of dissolution in 0.1, 0.01, and 0.001 M HCl: Soil Sci. Soc. Am. Proc., v.37, p. 29-33.

Goodman, B.A., Russell, J.D., Fraser, A.R. and Woodhams, F.W.D., 1976, A Mossbauer and IR spectroscopic study of the structure of nontronite: Clays Clay Minerals, v. 24, p. 53-59.

Graf, H., Richenbach, V. and Beyme, B., 1988, Oxidation of structural ferrous iron in vermiculites: I. Oxidizing Fe^{3+}: Clay Minerals, v. 23, p. 261-270.

Grim, R. E., 1968, Clay mineralogy: NY, McGraw-Hill Book Co., 596 p.

Grman, D., Pisarcik, M., and Novak, I., 1973, Investigation of octahedral isomorphous substitution in montmorillonites by means of infrared reflection spectroscopy: Silikaty, v. 17, p. 55-60.

Harder, H., 1978, Synthesis of iron layer silicate minerals under natural conditions: Clays Clay Minerals, v. 26, p. 65-72.

Harmon, W. L., 1987, Complete petrographic study for Electric Power Research Institute K-1 and I-1 wells compressed air energy storage site Pike County, Illinois: Irving, Texas, Litton Core Lab, 124 p.

Ismail, F.T., 1969, Role of ferrous iron oxidation in the alteration of biotite and its effect on the type of clay minerals formed in soils of arid and humid regions: Am. Mineral., v.54, p. 1460-1466.

Ismail, F.T., 1970, Oxidation-reduction mechanism of octahedral iron in mica type structures: Soil Sci., v. 110, p. 167-171.

Istvan, J. and Pereira, J., 1987, Field test of compressed air energy storage within an aquifer at Pittsfield, Illinois: in Proc. Geotechnology workshop on compressed-air energy storage in porous media sites (Traverse City, MI, Sept. 23-24, 1986), Palo Alto, EPRI AP-5301 proj. 2488-10, p.6-21 to 6-51.

Karickhoff, S.W. and Bailey, G.W., 1973, Optical absorption spectra of clay minerals: Clays Clay Minerals, v. 21, p. 59-70.

Kishk, F.M. and El-Sheemy, H.M., 1974, Potassium selectivity of clays as affected by the state of oxidation of their crystal structure iron: Clays Clay Minerals, v.22, p.41-47.

Klein, J.D. and Shuey, R.T., 1979, Nonlinear impedance of mineral-electrolyte interfaces, part I, pyrite: Geophysics, v. 43, p. 1222-1234.

Krapac, I.G., Griffin, R.S. and Dickerson, D.R., 1987, Assessment of oxygen depletion by inorganic constituents at the Pittsfield, Illinois compressed air energy storage site: in Proc. Geotechnology workshop on compressed-air energy storage in porous media sites (Traverse City, MI, Sept. 23-24, 1986), Palo Alto, EPRI AP-5301 proj. 2488-10, p.6-53 to 6-88.

Lahav, N. and Banin, A., 1968, Effect of various treatments on particle size and optical properties of montmorillonite suspensions: Israel J. Chem., v.6, p. 285-294.

Lear, P.R. and Stucki, J.W., 1985, The role of structural hydrogen in the reduction and reoxidation of iron in nontronite: Clays Clay Minerals, v. 33, p. 539-545.

Lindsay, W.L., 1988, Solubility and redox equilibria of iron compounds in soils: in Iron in soils and clay minerals, J.W. Stucki, B.A. Goodman and U. Schwertmann, eds., Dordrecht, D.Reidel, p. 37-62.

Marfunin, A.S., Mkrtchyan, A.R., Nadzharyan, G.N., Nyussik, Y.M. and Platonov, A.N., 1971, Optical and Mossbauer spectra of iron in some layered silicates: Izv. Akad. Nauk. SSSR, Ser.Geol.1971, p. 87-93.

McBride, M.B., 1979, Reactivity of adsorbed and structural iron in hectorite as indicated by oxidation of benzidine: Clays Clay Minerals, v. 27, p. 224-230.

McBride, M.B., Pinnavaia, T.J. and Mortland, M.M., 1975, Perturbation of structural Fe+3 in smectites by exchange ions: Clays Clay Minerals, v. 23, p. 103-107.

Mortimer, C. E., 1971, Chemistry a conceptual approach: New York, Van Nostrand Reinhold Company, p.555.

Nordstrom, D.K., 1982, Aqueous pyrite oxidation and the consequent formation of secondary iron minerals: in Acid sulfate weathering, L.R. Hossner, ed., Madison, Soil Sci. Soc. Am. Spec.Publ. 10, p. 37-56.

Orion Research, 1978, Instruction Manual model 97-08 oxygen electrode: Cambridge, MA, 23p.

Orion Research, 1983, Instruction Manual platinum redox electrodes model 96-78-00 and model 97-78-00: Cambridge, MA, 13p.

Plumlee, G.S. and Ridley, W.I., 1989, Chemical aspects of compressed air energy storage: a chemical modeling approach: U.S.G.S. Admin.Report to EPRI, var.pag.

Ridley, W.I. and Plumlee, G.S., 1988, A literature survey on oxygen depletion mechanisms in compressed air energy storage aquifers: U. S. Geol. Survey Admin. Report to EPRI, 12p.

Risatti, J.B. and Brower, R.D., 1987, Evaluation of microbiological depletion of oxygen in the Pittsfield, Illinois CAES site: in Proc. Geotechnology workshop on compressed-air energy storage in porous media sites (Traverse City, MI, Sept. 23-24, 1986), Palo Alto, EPRI, p.6-89 to 6-112.

Ross, G.J. and Kodama, H., 1976, Experimental alteration of a chlorite into a regularly interstratified chlorite-vermiculite by chemical oxidation: Clays Clay Minerals, v. 24, p. 183-190.

Ross, G.J., 1975, Experimental oxidation of chlorites into vermiculites by chemical oxidation: Nature, v. 255, p. 133-134.

Roth, C.B., Jackson, M.L. and Syers, J.K., 1969, Deferration effect on structural ferrous-ferric iron ratio and CEC of vermiculites and soils: Clays Clay Minerals, v. 17, p. 253-264.

Roth, C.B., Jackson, M.L., Lotse, E.G. and Syers, J.K., 1968, Ferrous-ferric ratio and CEC changes on deferration of weathered micaceous vermiculite: Israel J.Chem., v.6, p. 261-273.

Rowell, D.L., 1981, Oxidation and reduction: in The chemistry of soil processes, D.J. Greenland and M.H.B. Hayes, eds., NY, Wiley, p. 401-461.

Rozenson, I. and Heller-Kallai, L., 1976, Reduction and oxidation of Fe^{3+} in dioctahedral smectites -- I. Reduction with hydrazine and dithionite: Clays Clay Minerals, v. 24, p. 271-282.

Rozenson, I. and Heller-Kallai, L., 1976, Reduction and oxidation of Fe^{3+} in dioctahedral smectites -- II. Reduction with sodium sulfide solutions: Clays Clay Minerals, v. 24, p. 283-288.

Rozenson, I. and Heller-Kallai, L., 1978, Reduction and oxidation of Fe^{3+} in dioctahedral smectites -- III. Oxidation of octahedral iron in montmorillonite: Clays Clay Minerals, v. 26, p. 88-92.

Russell, J.D., 1979, An infrared spectroscopic study of the interaction of nontronite and ferruginous montmorillonites with alkali metal hydroxides: Clay Minerals, v. 14, p. 127-137.

Russell, J.D., Goodman, B.A. and Fraser, A.R., 1979, Infrared and Mossbauer studies of reduced nontronites: Clays Clay Minerals, v. 27, p. 63-71.

Sayin, M., 1982, Catalytic action of copper on the oxidation of structural iron in vermiculitized biotite: Clays Clay Minerals, v. 30, p. 287-290.

Scott, A.D. and Amonette, J., 1988, Role of iron in mica weathering: in Iron in soils and clay minerals, J.W. Stucki, B.A. Goodman and U. Schwertmann, eds., Dordrecht, D.Reidel, p. 537-623.

Scott, A.D. and Youssef, A.F., 1979, Structural iron oxidation during mica expansion: in Proc.Int'l. Clay Conf. (Oxford, 1978), M.M.Mortland and V.C.Farmer, eds., Amsterdam, Elsevier, p. 17-26.

Smith, G., Howes, B. and Hazen, Z., 1980, Mossbauer and optical spectra of biotite. A case for Fe^{2+}-Fe^{3+} interactions: Phys. Status. Solidi, v. A57, p. K187-K192.

Stucki, J.W. and Roth, C.B., 1976, Interpretation of infrared spectra of oxidized and reduced nontronite: Clays Clay Minerals, v. 24, p. 293-296.

Stucki, J.W. and Roth, C.B., 1977, Oxidation-reduction mechanism for structural iron in nontronite: Soil Sci. Soc. Am.J., v. 41, p. 808-814.

Stucki, J.W., 1988, Structural iron in smectites: in Iron in soils and clay minerals, J.W. Stucki, B.A. Goodman and U. Schwertmann, eds., Dordrecht, D.Reidel, p. 625-675.

Stucki, J.W., Golden, D.C. and Roth, C.B., 1984, Effects of reduction and reoxidation of structural iron on the surface charge and dissolution of dioctahedral smectites: Clays Clay Minerals, v. 32, p. 350-356.

Stucki, J.W., Low, P.F., Roth, C.B. and Golden, D.C., 1984, Effects of oxidation state of octahedral iron on clay swelling: Clays Clay Minerals, v. 32, p. 357-362.

van Breeman, N., 1980, Magnesium-ferric iron replacement in smectite during aeration of pyritic sediments: Clay Minerals, v. 15, p. 101-110.

van Breeman, N., 1988, Redox processes of iron and sulfur involved in the formation of acid sulfate soils: in Iron in soils and clay minerals, J.W. Stucki, B.A. Goodman and U. Schwertmann, eds., Dordrecht, D.Reidel, p. 825-841.

Van Olphen, H. and Fripiat, J. J., 1979, Data handbook for clay materials and other non-metallic minerals, NY, Pergamon Press, 346 p.

Veith, J.A and Jackson, M.L., 1974, Iron oxidation and reduction effects on structural hydroxyl and layer charge in aqueous suspension of micaceous vermiculites: Clays Clay Minerals, v. 22, p. 345-353.

Velde, B., 1985, Clay minerals: A physico-chemical explanation of their occurrence: Developments in sedimentology v.40: NY, Elsevier, 427 p.

Wong, J., 1979, An electrochemical model of the induced-polarization phenomenon in disseminated sulfide ores: Geophysics, v. 44, p. 1245-1265.

Wood, B.J. and Strens, R.G.J., 1979, Diffuse reflectance spectra and optical properties of some sulfides and related materials: Mineral.Mag., v. 43, p. 509-518.

Yariv, S. and Cross, H., 1979, Geochemistry of colloid systems: NY, Springer-Verlag, 450p.